Search for Scalar Top Quark Pair-Production in Scenario with Violated R-parity in $p\bar{p}$ Collisions at $\sqrt{s} = 1.96$ TeV

A thesis presented
by

Takashi Ogawa

to
The Department of Physics
in partial fulfillment of the requirements
for the degree of
Doctor of Philosophy
in the subject of

Physics

Waseda University
Tokyo, Japan
March 2005

©2005 - Takashi Ogawa

All rights reserved.

Thesis advisor

Kunitaka Kondo

Author

Takashi Ogawa

Search for Scalar Top Quark Pair-Production in Scenario with Violated R-parity in $p\bar{p}$ Collisions at $\sqrt{s} = 1.96$ TeV

Abstract

A search for the pair production of supersymmetric partner of the top quark in scenario with R-parity violation is presented. The quantum number called R-parity distinguishes particles in standard model from supersymmetric particles. A scalar top quark (stop) is assumed to decay only via R_p-violating supersymmetric coupling into tau lepton and b-quark. To collect events with multiple taus, a new special tau trigger (the lepton plus track trigger) is installed in Run II experiment of the Collider Detector at Fermilab (CDF). The goal of the lepton plus track trigger is to collect generic dilepton ($\ell\ell, \ell\tau, \tau\tau$) events with lower p_T threshold (8 GeV/c) and without prescale even at high luminosity. The $Z \to \tau\tau$ event, where one τ-lepton decays leptonically and the other hadronically, is a good benchmark to calibrate the the lepton plus track trigger and τ identification. The data sample of 72 pb^{-1}, collected using the electron plus track trigger, contains clear a τ signal from $Z \to \tau\tau$ events. The data used in stop search correspond to 200 pb^{-1}. The lower stop mass bound of 134 GeV/c^2 at a 95% confidence level is obtained. This limit is also directly applicable to the case of the third generation scalar leptoquark (LQ_3) assuming a 100% branching for the $LQ_3 \to \tau b$ decay mode.

Contents

List of Figures

List of Tables

Acknowledgments

I thank my supervisor, Prof. Kuni Kondo, for supporting and encouraging me through my short history of physics research. Also I would like to acknowledge Prof. Teruki Kamon, Dr. Alexei Safonov, and Vadim Khotilovich. The analyses in this thesis were collaborative with them and other members of the lepton plus track group, Sasha Baroiant, Prof. Maxwell Chertok, Prof. Richard Lander, Dr. John R. Smith, Prof. Aurore Savoy-Navarro, Dr. Carmine Pagliarone, Dr. Elena Vataga, Dr. Fedor Ratnikov, and Dr. Maxim Goncharov.

I thank the Fermilab staff and the technical staffs of the participating institutions for their vital contributions. This work was supported by the U.S. Department of Energy and National Science Foundation; the Italian Istituto Nazionale di Fisica Nucleare; the Ministry of Education, Culture, Sports, Science and Technology of Japan; the Natural Sciences and Engineering Research Council of Canada; the National Science Council of the Republic of China; the Swiss National Science Foundation; the A.P. Sloan Foundation; the Bundesministerium fuer Bildung und Forschung, Germany; the Korean Science and Engineering Foundation and the Korean Research Foundation; the Particle Physics and Astronomy Research Council and the Royal Society, UK; the Russian Foundation for Basic Research; the Comision Interministerial de Ciencia y Tecnologia, Spain; and in part by the European Community's Human Potential Programme under contract HPRN-CT-2002-00292, Probe for New Physics.

I thank Yoshihiro Hiratsuka, who is my first supervisor and excited my interest in physics. In addition, I would like to leave the names of Taku Ito and Kenji Hirawatari for our spent time together. Most importantly I thank my parents, who support me in many meanings. This thesis is dedicated to my mother. Finally I would like to thank Mai Saeki. Without her patience, support and love, I could not accomplish this thesis, which should be dedicated to her as well.

Chapter 1

Introduction

Our understanding in the elementary particle physics is based on the Standard Model (SM) at present. The SM have been succeeded in describing the properties and interactions of elementary particles in the last thirty years. Experimental measurements also has shown a remarkable agreement with the SM. In spite of its success, the SM is regarded as merely a good low energy effective theory, since it builds on many assumptions and still leaves many theoretical questions which can be answered only by the introduction of new physics. There have been various theoretical attempts to solve the problems of the SM such as quark compositeness, technicolor, supersymmetry (SUSY) and large extra dimensions.

Among them, SUSY is a natural extension to the SM by introducing a new type of space-time symmetry between fermions and bosons. In this theory all the SM particles have their own superpartners: every fermion (boson) has a bosonic (fermionic) superpartner. The Minimal Supersymmetric extension of the Standard Model (MSSM) expands the SM with a minimum number of new particles and interactions while remaining consistent with observation. Supersymmetric theory defines a new multiplicative quantum number called R-parity which distinguishes SM particles from their superpartners. The MSSM is constructed to conserve both baryon number and lepton number so that R-parity conservation is imposed on the couplings. If R-parity is conserved, supersymmetric particles can only be produced in pairs and the Lightest Supersymmetric Particle (LSP) should be stable to be a candidate of cold dark matter (CDM).

However, because R-parity conservation is not necessarily transcendental in SUSY and gauge invariance in general, there is considerable theoretical and phenomenological interest in studying the implication of R-parity violation. In this scenario, the LSP is not stable any longer and various new decays have to be considered in SUSY search. Such processes have become important topics in recent years.

Although experimental searches for SUSY particles have been continued for past 20 years or more, no evidence has discovered yet. Consequently, it is surmised that almost SUSY particles have heavy masses. However top quark has the maximum mass among the observed particles in the SM therefore it is pointed out that scalar top quark (stop) can be lighter than other SUSY particles. This is because the off-diagonal components (related to the top quark mass) of the stop quark mass matrix becomes large and can have the solution of a comparatively small mass eigenstate. Because stop can decay into tau lepton and b-quark in scenario with R-parity violation, stop pair-production yields to two tau leptons and two jets from b-quark.

The R-parity violating stop was searched using data with an integrated luminosity of 106 pb^{-1} at a center of mass energy of $\sqrt{s} = 1.8$ TeV, which were collected by the Collider Detector at Fermilab (CDF) during the 1992-93 (Run Ia) and 1994-95 (Run Ib) runs. However no evidence was observed and stop mass is limited to below 122 GeV/c^2 at 95% confidence level.

The CDF is a general purpose detector to study $p\bar{p}$ collision at the Tevatron collider in Fermi National Accelerator Laboratory, Illinois, U.S.. The Tevatron has been upgraded in energy and luminosity for Run II as well as The CDF is improved for high rate of data-taking. Thus the data worth of an integrated luminosity of 2000 pb^{-1} at the center of mass energy of 1.96 TeV is expected to be taken in Run IIa which started in March 2001.

In Run II the study of processes containing tau leptons in the final state play an important role in physics both within and beyond the SM, especially SUSY processes. It was shown in results both from LEP 200 and from CDM constraints that SUSY favor large value for tan β. This means enhancement in the branching ratio of the decays of SUSY particles into tau leptons as compared to other charged leptons. In order to be able to select such events, specific dedicated tau trigger system have been designed and implemented at CDF in Run II (CDF-II), which is called the lepton plus track trigger. This trigger system compromise a reasonable data-taking rate with high luminosity in Run II and a low threshold for lepton momentum. The lepton plus track trigger has shown good performance and collected tau enriched sample since the installation. The CDF group uses its sample for some physics topics such as R-parity violating stop.

This thesis is organized as follows. The next chapter begins with a introduction of the theoretical concepts of the SUSY and the stop. In Chapter 3, the proton-antiproton collider at Fermilab and the CDF detector are reviewed. The lepton plus track trigger system to collect events in multi-tau final states is described in Chapter 4. Its application to various physics is also discussed. The validation of the lepton plus track trigger is confirmed in the $Z \to \tau\tau$ process with 72 pb^{-1} data in Chapter 5. Chapter 6 shows the result of an indirect search for SUSY through measurements of the branching ratio of $B_{s(d)} \to \mu\mu$. In Chapter 7, the analysis of stop quark is explained in detail, such as data, event selection, systematic uncertainties, background evaluation, and results, followed by a short summary which concludes the dissertation.

Chapter 2

Theory

2.1 Standard Model

Particle physics attempts to understand the fundamental constituents of matter and their interactions. The SM is a quantum field theory which postulates that all matters are composed of fermions and that the fundamental forces of nature are mediated by gauge boson. They are spin $\frac{1}{2}$ particles comprising two families: the leptons and quarks. The lepton and quark families are each divided into three generations of leptons and quark doublets. The interaction forces of the leptons and quarks are mediated by the exchange of fundamental gauge bosons. There are four known forces governing the interactions of matter at low energy: strong, electromagnetic, weak, and gravitational.

The strong force is attractive and has a very short range of interaction. The strong force is mediated only between quarks by the exchange of gluons. It is responsible for the binding of protons and neutrons to form atomic nuclei. This force is described by Quantum ChromoDynamics (QCD).

The electromagnetic force is attractive (repulsive) force if the particles have the opposite (same) signs of electric charge. This force is mediated by the exchange of protons and weaker than the strong force by approximately two orders of magnitude. It is responsible for the binding of electrons to nuclei to form atoms.

The weak force also has a short range of interaction and is mediated by heavy gauge bosons, and affects quarks, leptons and the gauge bosons excluding gluons. This force is approximately six order of magnitude smaller than the strong force and responsible for neutron decay.

Finally, the gravitational force is purely attractive between two massive particles. Sine the gravitational force is much weaker than any other forces (roughly 40 orders of magnitude weaker than the strong force), this effects are usually ignored in the SM framework in the high energy collider experiments. On the other hand, it becomes significant for bodies with astronomical mass like our earth or galaxy.

The SM is based on the gauge symmetry group $SU(3) \times SU(2) \times U(1)$, where $SU(3)$ and $SU(2) \times U(1)$ govern the strong force and the electroweak force, respectively. This gauge symmetry group breaks spontaneously in the electroweak sector through the Higgs mechanism, which invokes a special kind of neutral scalar particle called the Higgs Boson. This particle is the only remained undiscovered piece of the SM.

This SM explains up to now most of experimental facts but leaves some problems. For examples,

- The energy scale of Grand Unified Theory (GUT) is $\mathcal{O}(10^{15}\ \mathrm{GeV}/c^2)$ while that of the electroweak is $\mathcal{O}(100\ \mathrm{GeV}/c^2)$. This is called hierarchy problem, which requires the fine-tuning of the parameters through 26 orders for the stabilization of the Higgs mass around the electroweak scale against the radiative correction within the SM framework.

- The extrapolations of the coupling constants come close together at very high energies, but do not actually meet (See **Fig.2.1** [1]). However a modified set of renormalization group, to be explained later, gives a unification around the GUT energy scale (See **Fig.2.2** [1]).

- The upper limit of the proton life time observed at the Kamiokande is larger than the expectation of GUT within the SM [2].

- The Lightest Supersymmetric Particle (LSP) is a good candidate for Cold Dark Matter (CDM) [3].

One possibility to solve these problems are SUperSYmmetry (SUSY). SUSY is a new kind of symmetry not included in the SM.

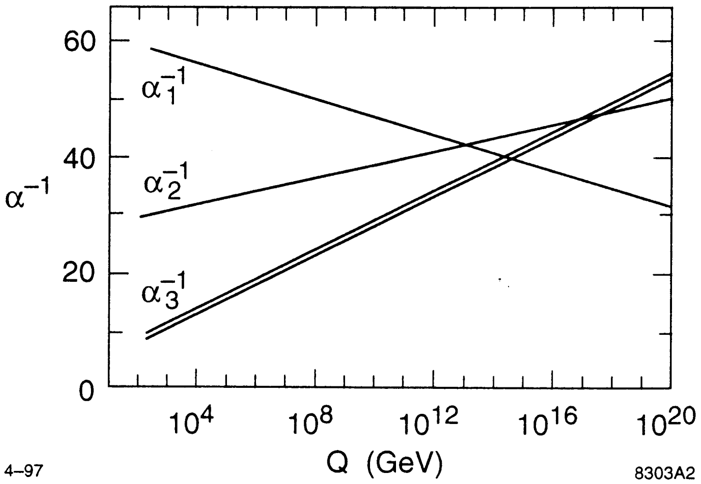

Fig. 2.1. Evolution of the inverse of the $SU(3) \times SU(2) \times U(1)$ couplings to high energy scales, using the one-loop renormalization group equation of the SM.

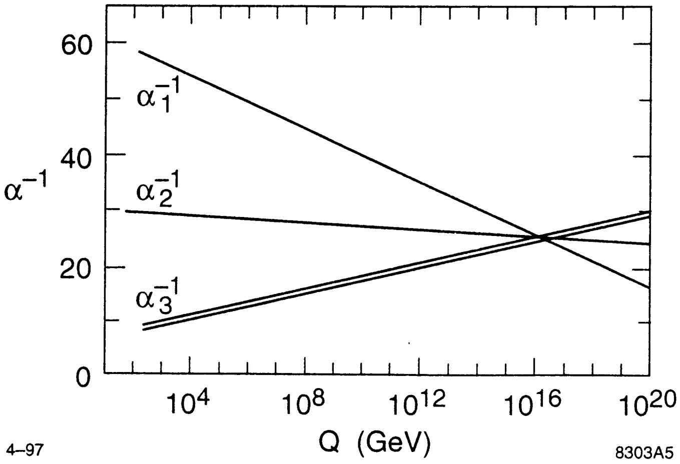

Fig. 2.2. Evolution of the inverse of the $SU(3) \times SU(2) \times U(1)$ couplings to high energy scales, using the one-loop renormalization group equation of the MSSM.

2.2 Supersymmetry

The new symmetry called SUSY relates bosons to fermions and vice versa. It is predicted that quarks(leptons) have their partners with 0-spin, squarks(sleptons), and gauge bosons have partners with $\frac{1}{2}$-spin, gauginos, but these partners have not been observed so far. Considering this fact, SUSY is not a strict symmetry.

2.2.1 The Minimal Supersymmetric extension of the Standard Model

The Minimal Supersymmetric extension of the Standard Model (MSSM) is the simplest linear extension of the SM. The MSSM has the same gauge group as the SM. As a feature of the MSSM, there exists a quantum number called R-parity;

$$R_p = (-1)^{3B+L+2s} \tag{2.1}$$

where B, L and s indicate baryon number, lepton number and spin, respectively. The R-parity discriminates between ordinary and supersymmetric particles; $R_p = +1$ for SM particles and $R_p = -1$ for their supersymmetric partners.

If R-parity is really conserved, it leads to two important phenomenological implications. Firstly, SUSY particles can only be produced in pairs. Secondly, the LSP is stable.

2.2.2 Supersymmetric Particle

The MSSM has many particles which don't exist in the SM. In the MSSM there are a second Higgs doublet, the spin $\frac{1}{2}$ partners for Higgs field called higgsinos, the spin $\frac{1}{2}$ partners for the SM bosons and spin 0 partners for the SM fermions. In addition the graviton which mediates gravity and its partner, the gravitino, are predicted but they are not considered in this thesis. The SM fermions have two different states, right-handed and left-handed states. Because each state has its superpartner, the SM fermion f have two superpartners $\tilde{f}_R$, $\tilde{f}_L$. Most SUSY particles are mixed and become the mass eigenstates. For instance the mass eigenstates of charged gauginos and charged higgsinos are called charginos $\tilde{\chi}^{\pm}_{1,2}$. Analogous to the chargino case, mixtures take place between neutral gauginos and neutral higgsinos, so the mass eigenstates are called neutralinos $\tilde{\chi}^0_j$ $(j = 1, 2, 3, 4)$. In large SUSY parameter regions, the lightest neutralino $\tilde{\chi}^0_0$ is assumed to be the LSP. These particles are summarized in **Table 2.1** [4].

Table 2.1. Particle content of the Minimal Supersymmetric Standard Model.

SM particles + additional Higgs		SUSY particles	
$j = \frac{1}{2}$	$q_{L_i}=\begin{pmatrix} u_{L_i} \\ d_{L_i} \end{pmatrix}, u_{R_i}, d_{R_i}$ $l_{L_i}=\begin{pmatrix} \nu_{L_i} \\ e_{L_i} \end{pmatrix}, e_{R_i}$	$j = 0$	$\tilde{q}_{L_i}=\begin{pmatrix} \tilde{u}_{L_i} \\ \tilde{d}_{L_i} \end{pmatrix}, \tilde{u}_{R_i}, \tilde{d}_{R_i}$ $\tilde{l}_{L_i}=\begin{pmatrix} \tilde{\nu}_{L_i} \\ \tilde{e}_{L_i} \end{pmatrix}, \tilde{e}_{R_i}$
$j = 1$	g^a	$j = \frac{1}{2}$	$\tilde{g}^a$
	$\gamma, Z, W^{\pm}$		$\tilde{\chi}^0_i = a_i\tilde{\gamma} + b_i\tilde{Z} + c_i\tilde{H}^0_1 + d_i\tilde{H}^0_2$
$j = 0$	$H_1 = \begin{pmatrix} H^0_1 \\ H^-_1 \end{pmatrix}, H_2 = \begin{pmatrix} H^+_2 \\ H^0_2 \end{pmatrix}$		$\tilde{\chi}^{\pm}_k = \alpha_k\tilde{W}^{\pm} + \beta_k\tilde{H}^{\pm}_{1,2}$

2.2.3 Supersymmetric Lagrangian

In this section, we will consider briefly the supersymmetric Lagrangian $\mathcal{L}$ which is invariant under supersymmetric transformations. The minimum content in four dimensions consists of a single left-handed two component Weyl fermion ψ. Since this is an intrinsically complex object, it seems sensible to choose as its superpartner a complex scalar field ϕ. In the Ref [5],

$$\mathcal{L} = -\partial^{\mu}\phi^{*i}\partial_{\mu}\phi_i - i\psi^{\dagger i}\bar{\sigma}^{\mu}\partial_{\mu}\psi_i - \frac{1}{2}\left(W^{ij}\psi_i\psi_j + W^{*ij}\psi^{\dagger i}\psi^{\dagger j}\right) - W^iW^*_i \tag{2.2}$$

where W^i and W^{ij} are derivatives of *superpotential* W,

$$W = \frac{1}{2}M^{ij}\phi_i\phi_j + \frac{1}{6}y^{ijk}\phi_i\phi_j\phi_k, \tag{2.3}$$

$$W^{ij} = \frac{\delta^2}{\delta\phi_i\delta\phi_j}W = M^{ij} + y^{ijk}\phi_k, \tag{2.4}$$

$$W^i = \frac{\delta W}{\delta\phi_i} = M^{ij}\phi_j + \frac{1}{2}\phi_j\phi_k. \tag{2.5}$$

A chiral *superfield*, Φ, is a single object which contains as components all of the bosonic, fermionic, and auxiliary fields within the corresponding supermultiplet. The gauge quantum numbers and mass dimension of a chiral superfield are the same as that of its scalar component. One writes the superpotential of supermultiplets

$$W = \frac{1}{2} M^{ij} \Phi_i \Phi_j + \frac{1}{6} y^{ijk} \Phi_i \Phi_j \Phi_k. \tag{2.6}$$

The most general superpotential as given in Eq. (2.6) contains trilinear couplings of chiral matter supermultiplets, like the Higgs, the quark, and the lepton supermultiplet. Couplings between the different Higgs fields or between the Higgs field and the corresponding lepton/quark supermultiplets are needed to construct the two Higgs doublet sector in the scalar potential. Although these vertices conserve the over-all fermion number, they may violate the baryon and lepton numbers and would lead to the same effects as leptoquark. The general superpotential Eq. (2.6) can be separated into R-parity conserving part (W_{MSSM}) and R-parity violating part ($W_{\not{R}_p}$);

$$W = W_{MSSM} + W_{\not{R}_p}. \tag{2.7}$$

Here W_{MSSM} is given by

$$W_{MSSM} = (y_L)_{ij} H_u \overline{e}^i L^j + (y_D)_{ij} H_u \overline{d}^i Q^j + (y_U)_{ij} H_d \overline{u}^i Q^j + \mu H_u H_d, \tag{2.8}$$

where L (Q) is the lepton (quark) $SU(2)_L$ doublet, e (u and d) is the lepton (up- and down-type quarks, respectively) $SU(2)_L$ singlet, and $H_{u(d)}$ is the up(down)-type Higgs $SU(2)_L$ doublet. Also (i, j) are the generation indices, namely $i, j = 1, 2, 3$. The $SU(2)_L$ weak isospin indices and the $SU(3)_C$ color index have been suppressed. The y_L, y_D and y_U are the dimensionless Yukawa couplings in the 3×3 generation space. The μ is the Higgs mass parameter and the μ-term in Eq.(2.8) represents the supersymmetric version of the Higgs boson mass term in the SM.

2.2.4 R-parity violation

The SUSY models with the R-parity violating ($\not{R}_p$) interactions have been considered in a number of papers [6-8]. There also have been discussions of trying to explain the large-Q^2 events at HERA [9] in the context of the $\not{R}_p$-SUSY models [10].

The $\not{R}_p$ interactions are introduced by adding the following terms of the chiral superfields to the superpotential of the MSSM:

$$W_{\not{R}_p} = \underbrace{\lambda_{ijk} L^i L^j \overline{e}^k}_{L\text{-violation}} + \underbrace{\lambda'_{ijk} L^i Q^j \overline{d}^k}_{L\text{-violation}} + \underbrace{\lambda''_{ijk} \overline{u}^i \overline{d}^j \overline{d}^k}_{B\text{-violation}} + \underbrace{\epsilon_i L^i H_u}_{L\text{-violation}} , \tag{2.9}$$

where (i, j, k) are the generation indices. First three terms are the explicit R-parity violation ones resulting from the trilinear $\not{R}_p$(TRPV) couplings. The first and the third term is antisymmetric for (i, j) and (j, k), respectively. There are, thus, $9 + 27 + 9 = 45$ coupling constants. These terms represent the lepton number or baryon number violating interactions as indicated, and cause violation of the R-parity. The last term is the bilinear $\not{R}_p$(BRPV) couplings, which gives spontaneous $\not{R}_p$through non-zero VEVs (Vacuum Expectation Values) for sneutrinos [11]. However, the spontaneous breaking via VEVs of the doublet sneutrinos of the MSSM is excluded by Γ_Z measurements [12]. The spontaneous $\not{R}_p$ is not viable unless additional singlet sneutrinos are introduced [13].

Expanding the superpotential in TRPV, we have the Yukawa couplings between the SM matter fields and their superpartners in the Lagrangian:

$$\begin{aligned} \mathcal{L}_{TRPV} &= \lambda_{ijk}(\nu^i_L \tilde{e}^j_L \overline{e}^k_R - e^i_L \tilde{\nu}^j_L \overline{e}^k_R + ...) \\ &\quad + \lambda'_{ijk}(\nu^i_L \tilde{d}^j_L \overline{d}^k_R - e^i_L \tilde{u}^j_L \overline{d}^k_R + ...) + \lambda''_{ijk}(\overline{u}^i_R \overline{\tilde{d}}^j_R \overline{d}^k_R + ...) + \text{h.c.} \end{aligned} \tag{2.10}$$

There are similar terms (indicated by "...") from permutation of the tilde. For clarity, examples of decays for each term are given in **Table 2.2**.

Table 2.2. Examples of decays by the $\not{R}_p$ interactions.

Interaction	Elementary decays
λ	$\tilde{\ell}_j \longrightarrow \overline{\nu}_i \ell_k$, $\tilde{\nu}_j \longrightarrow \ell^+_i \ell^-_k$
λ'	$\tilde{d}_j \longrightarrow \overline{\nu}_i d_k$, $\tilde{u}_j \longrightarrow \ell^+_i d_k$
λ''	$\tilde{d}_j \longrightarrow \overline{u}_i \overline{d}_k$

Note that, from $L^i L^j$ and $L^i Q^j$, we have only couplings between the up-type and down-type doublet particles (λ' in **Table 2.2**).

2.3 General discussions of $\not R_p$ model

2.3.1 Constraints on the $\not R_p$ couplings

There are constraints on the TRPV couplings from various measurements as summarized in **Table 2.3** [7,14-25]. For simplicity, it has been assumed that one $\not R_p$ operator at a time is dominant in obtaining the bounds.

Table 2.3. Upper limits on the TRPV couplings for the sparticle mass of 100 GeV/c^2, and corresponding measurements.

λ		λ'						λ''	
ijk		ijk		ijk		ijk		ijk	
121	$0.05^{(a)}$	111	$0.001^{(d)}$	211	$0.09^{(h)}$	311	$0.16^{(k)}$	112	$10^{-6(\ell)}$
122	$0.05^{(a)}$	112	$0.02^{(a)}$	212	$0.09^{(h)}$	312	$0.16^{(k)}$	113	$10^{-5(m)}$
123	$0.05^{(a)}$	113	$0.02^{(a)}$	213	$0.09^{(h)}$	313	$0.16^{(k)}$	123	–
131	$0.06^{(b)}$	121	$0.035^{(e)}$	221	$0.18^{(i)}$	321	$0.20^{(f)}$	212	–
132	$0.06^{(b)}$	122	$0.06^{(c)}$	222	$0.18^{(i)}$	322	$0.20^{(f)}$	213	–
133	$0.004^{(c)}$	123	$0.20^{(f)}$	223	$0.18^{(i)}$	323	$0.20^{(f)}$	223	–
231	$0.06^{(b)}$	131	$0.035^{(e)}$	231	$0.22^{(j)}$	331	$0.26^{(g)}$	312	$0.43^{(g)}$
232	$0.06^{(b)}$	132	$0.33^{(g)}$	232	$0.39^{(g)}$	332	$0.26^{(g)}$	313	$0.43^{(g)}$
233	$0.06^{(b)}$	133	$0.002^{(c)}$	233	$0.39^{(g)}$	333	$0.26^{(g)}$	323	$0.43^{(g)}$

(a)	charged current universality [14, 15]
(b)	$\Gamma(\tau \to e\nu\overline{\nu})/\Gamma(\tau \to \mu\nu\overline{\nu})$ [14, 15]
(c)	bound on the ν_e mass [7, 16]
(d)	ν-less double-β decay [17]
(e)	atomic parity violation [18]
(f)	D^0-$\overline{D^0}$ mixing [19, 20]
(g)	$\Gamma_h(Z^0)/\Gamma_\ell(Z^0)$ [21, 22]
(h)	$\Gamma(\pi \to e\overline{\nu})/\Gamma(\pi \to \mu\overline{\nu})$ [14]
(i)	$B_R(D^+ \to \overline{K^{0*}}\mu^+\nu_\mu)/B_R(D^+ \to \overline{K^{0*}}e^+\nu_\mu)$ [22, 23]
(j)	ν_μ deep-inelastic scattering [14]
(k)	$B_R(\tau \to \pi\nu_\tau)$ [22, 23]
(l)	heavy nucleon decay [25]
(m)	n-$\overline{n}$ oscillation [24, 25]

These bounds are obtained for the sparticle mass of 100 GeV/c^2 and become less tighter for larger masses. We see that there is basically 3 to 4 orders of magnitude for the $\not R_p$ couplings which collider experiments can explore.

Because of the assumption made above for simplicity, constraints on products of two couplings are not included in **Table 2.3**. In fact, there are strong constraints as given below.

Proton stability:

Sizable $\not{R}_p$ couplings result in faster proton decays. There is a strong constraints obtained from the present limit on the proton stability, $\tau(p \longrightarrow e\pi) > 10^{32}$ years [25]:

$$\lambda'_{11k} \cdot \lambda''_{11k} < (2 \times 10^{-27}) \cdot \left(\frac{m_{\tilde{d}_k}}{100\ [\mathrm{GeV}/c^2]} \right)^2 . \tag{2.11}$$

From this strong constraints, one sees that existence of the λ' and λ'' interactions simultaneously puts the magnitude of the coupling far below the bound of our interest.

$\mu \longrightarrow e\gamma$:

The lepton-flavor-violating interactions contribute to the process $\mu \longrightarrow e\gamma$. From an observed limit on this decay, the constraint is obtained [26] as,

$$\lambda_{1jk} \cdot \lambda_{2jk}, \quad \lambda_{ij1} \cdot \lambda_{ij2} < 10^{-4}, \qquad \lambda'_{1jk} \cdot \lambda'_{1jk} < 10^{-6}, \tag{2.12}$$

although the result is highly dependent on the input SUSY parameters, and the constraints are evaded for some choices of the parameters.

Neutrino mass

The $\not{R}_p$ couplings generate neutrino VEVs and lepton-Higgs mixing, which then result in non-zero neutrino mass. This effect has been studied in detail in Ref. [26] including all soft SUSY-breaking terms from the $\not{R}_p$ interactions as well as usual SUSY interactions, and the bounds are obtained as

$$\lambda_{i33} < 10^{-2}, \qquad \lambda'_{i33} < 10^{-3} \tag{2.13}$$

for $m_{\nu_i} < 1$ keV/c^2. The impact was found to be rather larger than the case where the soft terms were included only partially like those in **Table 2.3**, but the constraints are dependent on the input SUSY parameters as in the $\mu \rightarrow e\gamma$ case. Note that 1 keV/c^2 is very loose. For

m_{ν_e}, the limit must be at least one order tighter than Eq. (2.13)[1].

2.3.2 Theoretical considerations

Discrete symmetry:

In principle, it is possible that only λ'_{11k} and/or λ''_{11k}, a subset of the whole $\not{R}_p$ couplings, happen to be so small as to satisfy Eq. (2.11). Theoretically, however, it is natural to consider that such strong suppression is due to some discrete symmetries. There are many possibilities of discrete symmetries to protect the proton [27]. Obviously, simultaneous conservation of L and B ensures the proton stability, but it forbids any $\not{R}_p$ interactions. Our interest is, thus, the case where only L or B is conserved.

In trying to understand such discrete symmetries as what comes from more fundamental theory, it has been argued that the quantum gravity effects violate all the discrete symmetries other than *discrete gauge symmetries* [28]. They are remnants of a higher gauge symmetry which has been broken at low-energy scale. It has been shown that, in the MSSM, only the R_p conservation and B conservation can be such discrete gauge symmetries [29]. Actually, there are the GUT models of $SU(5)$ and $SO(10)$ gauge group where the $\not{R}_p$ interaction at low-energy scale is only due to λ and λ', respectively [7, 30] [2]. As a reasonable scenario, we consider only the $\not{R}_p$ interactions due to λ and λ' in this study.

The constraints Eq. (2.12) are much looser than the case for the proton. For example, if the two couplings are the same magnitude, then $\lambda \simeq 10^{-2}$ and $\lambda' \simeq 10^{-3}$. It is not unreasonable to consider that this is within the variation of the magnitude of the couplings rather than regarding them as an indication of some symmetries if we think of that the top quark Yukawa coupling is almost a factor of 40 times larger than the bottom Yukawa coupling [19].

Matter asymmetry in the universe:

Existence of L or B-violating interactions may conflict with the observed matter asymmetry in

---

[1] Neutrino mass scales by $\lambda^2_{\not{R}_p}$. So $\times 10^{-1}$ smaller couplings give $\times 10^{-2}$ reduction on the mass.

[2] Also, there are models with the $\not{R}_p$ interaction in string theories [31].

the universe. If the present matter asymmetry was generated below the electroweak scale, the $\not{R}_p$ violation in SUSY does not affect it. In the case that the origin of the matter asymmetry is in higher energy scale such as the GUT scale or the Plank scale, a part of the B asymmetry is erased ($B \to 0$) by B-violating *sphaleron* interactions in the electroweak sector, which, however, conserve $B - L$ and $B/3 - L_i$ for each lepton generation. As long as $B - L \neq 0$ initially, the L asymmetry remains ($L \to L - B$) and a part of it is converted to the B asymmetry via SM leptonic and supersymmetric mass effects below the electroweak scale [32]. When B-violating interactions are added, the same argument applies since it does not touch L, and keeping matter asymmetry is feasible. Existence of the L-violating interactions, however, washes away the L asymmetry, and it, together with the sphaleron interactions, buries the matter asymmetry. In this situation, the matter asymmetry is only viable if at least one of L_i is conserved and $B/3 - L_i$ is left unchanged. So we have to assume that

- λ and λ' involving at least one lepton generation must be 0.

SUperGRAbity (SUGRA):

In the framework of SUGRA, large $\not{R}_p$ couplings would change the running of the sfermion masses, so do the spectrum as well. It turned out [26] that neglecting the $\not{R}_p$ terms has less than 10% effect in the running of the coupling themselves with respect to the full calculation if

$$\lambda < 0.27, \qquad \lambda' < 0.15, \qquad \lambda'' < 0.15 \tag{2.14}$$

at the electroweak scale. Because most of the constraints given in **Table 2.3** are already smaller than or at least similar to the bounds in Eq. (2.14), we follow such a technically simple way.

2.4 Scalar Top Quark

2.4.1 Mass Eigenstate

As already mentioned every SM fermion (except for neutrinos) has two partners with 0-spin denoted by $\tilde{f}_L$ and $\tilde{f}_R$, one for each chiral state. These scalar partners have the same electric charge and color, therefore the left- and right-chiral states can be mixed if $SU(2) \times U(1)$ is broken. It turns out that these particles can be mixed and form the mass eigenstates.

The large Yukawa couplings imply a large mixing between $\tilde{f}_L$ and $\tilde{f}_R$ and large couplings to the higgsino components of neutralinos and charginos. The sfermions of the third generation have a quite different phenomenology compared to those of the first two generations owing to the large Yukawa couplings. The mass matrix $\mathcal{M}$ of the scalar top quark (stop) is given by

$$\mathcal{M}^2_{\tilde{t}} = \begin{pmatrix} M^2_{\tilde{t}_L} + M^2_t + M^2_Z \cos 2\beta(\frac{1}{2} - \frac{2}{3}\sin^2\theta_W) & M_t(A_t - \mu\cot\beta) \\ M_t(A_t - \mu\cot\beta) & M^2_{\tilde{t}_R} + M^2_t + M^2_Z \cos 2\beta(\frac{2}{3}\sin^2\theta_W) \end{pmatrix}, \quad (2.15)$$

where the angle θ_W is the weak mixing angle (or Weinberg angle), $\tan\beta$ is the ratio of VEVs from the two Higgs doublets, and A_t is a coefficient for Higgs-stop-stop trilinear coupling. Note that the off-diagonal elements are proportional to the top quark mass leading to a strong mixing and a large mass splitting between the mass eigenstates $\tilde{t}_1$ and $\tilde{t}_2$ ($M_{\tilde{t}_1} < M_{\tilde{t}_2}$). The diagonalized mass eigenstates are

$$\tilde{t}_1 = \tilde{t}_L \cos\theta_{\tilde{t}} + \tilde{t}_R \sin\theta_{\tilde{t}}, \quad (2.16)$$

$$\tilde{t}_2 = -\tilde{t}_L \sin\theta_{\tilde{t}} + \tilde{t}_R \cos\theta_{\tilde{t}}, \quad (2.17)$$

where $\theta_{\tilde{t}}$ stands for the mixing angle between $\tilde{t}_L$ and $\tilde{t}_R$. The off-diagonal elements in Eq. (2.15) tend to induces a significant mixing which reduces the square of the lightest stop eigenmass. As a consequence, the $\tilde{t}_1$ could be substantially lighter than other squarks.

2.4.2 Pair Production

At the Tevatron, scalar top quarks are pair-produced via gg fusion and $q\bar{q}$ annihilation. **Fig. 2.3** shows the Next-to-Leading Order (NLO) cross-section for $p\bar{p} \to \tilde{t}_1\bar{\tilde{t}}_1$ process at $\sqrt{s} =$ 1.96 TeV using PROSPINO [33] with CTEQ6M Parton Distribution Function (PDF) set [34, 35]. Renormalization and factorization scales are set to $\sqrt{M^2(\tilde{t}_1) + p^2_T(\tilde{t}_1)}$. While the cross section is affected by other SUSY parameters like gluino mass, the effect is only in high order

Table 2.4. PROSPINO predictions for the stop pair production cross-section as a function of stop mass. Calculation is obtained by using CTEQ6M PDF set and renormalization and factorization scales are both set to $\sqrt{M^2(\tilde{t}_1) + p_T^2(\tilde{t}_1)}$.

$M(\tilde{t}_1)$ [GeV/c^2]	100	110	120	130	140	150	160
$\sigma(p\bar{p} \to \tilde{t}_1\tilde{t}_1)$ [pb]	15.07	8.89	5.45	3.45	2.25	1.50	1.02

correction. **Table 2.4** gives numerical values for the expected cross section. These values are large enough to be detected at the Tevatron.

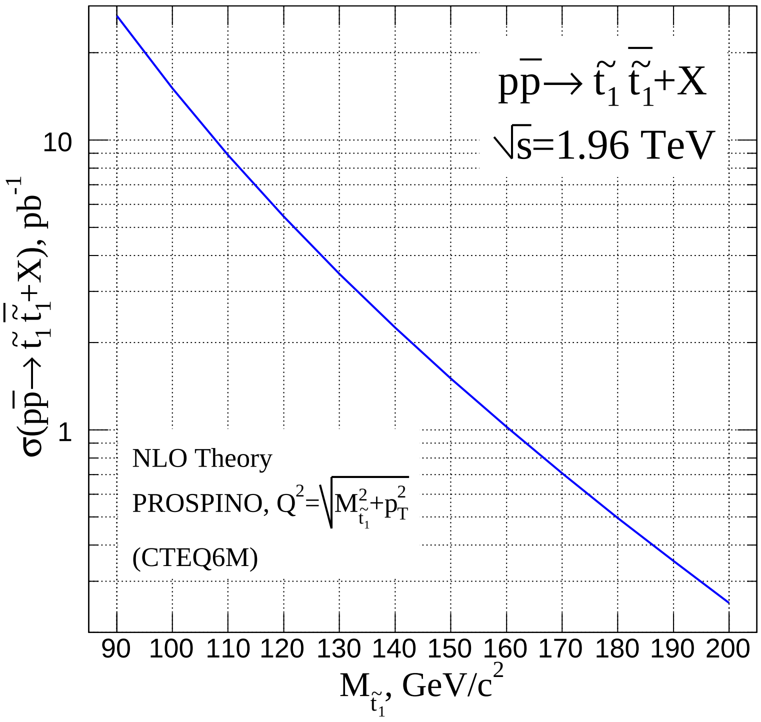

Fig. 2.3. NLO cross-section for the $p\bar{p} \to \tilde{t}_1\bar{\tilde{t}}_1$ process using CTEQ6M PDF set and with renormalization and factorization scales set to $\sqrt{M^2(\tilde{t}_1) + p_T^2(\tilde{t}_1)}$.

2.4.3 Decay Channel

According to stop and other SUSY particles, the decay modes of $\tilde{t}_1$are different considerably. These modes are classified to some cases.

(i) Two body decays at tree level [36]

In general, sfermions decay according to $\tilde{f} \to \tilde{\chi}^0_j + f$ [j = 1-4] and $\tilde{f} \to \tilde{\chi}^\pm_i + f'$ [i = 1,2]. Normally the flavor conserving decay into the LSP is permissible, and yet the light stop may be an exception because of the large top quark mass. Nevertheless, the decay of a light stop into the lighter chargino $\tilde{\chi}^\pm_1$ and a bottom quark can still be accessible in this case.

$$\tilde{t}_1 \to t + \tilde{\chi}^0_1, \tag{2.18}$$

$$\tilde{t}_1 \to b + \tilde{\chi}^+_1. \tag{2.19}$$

(ii) Two body decay at loop level [37]

There is a wide range of SUSY parameters where all two body decays of the light stop are forbidden at tree level. Therefore as far as two body decays are concerned the flavor changing decay into a charm quark and the LSP, which is induced at one loop level, becomes important.

$$\tilde{t}_1 \to c + \tilde{\chi}^0_1. \tag{2.20}$$

(iii) Multi body decays at higher orders [38, 39]

Additionally there are some three or more body decays of the light stop. The dominant decay channel of $\tilde{t}_1$ mostly depends on the mass of $\tilde{t}_1$ and the masses of the final state particles. When the light stop is heavy comparatively, the three body decays into W^+ or H^+ can be accessible. In addition if sleptons(sneutrinos) are lighter than $\tilde{t}_1$, the decays into slepton(sneutrino) become possible. With an attention to this, on condition that the mass of $\tilde{t}_1$ is less than the gluino mass $m_{\tilde{g}}$ in the MSSM, the following decay modes are considered.

$$
\begin{aligned}
\tilde{t}_1 &\rightarrow b + W^+ + \tilde{\chi}_1^0, &(2.21)\\
\tilde{t}_1 &\rightarrow b + H^+ + \tilde{\chi}_1^0, &(2.22)\\
\tilde{t}_1 &\rightarrow b + \tilde{l} + \nu, &(2.23)\\
\tilde{t}_1 &\rightarrow b + l + \tilde{\nu}, &(2.24)\\
\tilde{t}_1 &\rightarrow b + f + \bar{f}' + \tilde{\chi}_1^0. &(2.25)
\end{aligned}
$$

(iv) Two body decay in $\not{R}_p$ model [40, 41]

Stop can decay into a tau lepton and a bottom quark when R-parity is violated via non-zero λ' or ϵ_3 in superpotential $W_{\not{R}_p}$. The branching ratio of this channel will be 100 % in both TRPV and BRPV frameworks, if the stop is the LSP. If the LSP is the lightest neutralino with the Next Lightest Supersymmetric Particle (NLSP) being the stop, channel (ii) is possible. However, it has been also shown that large λ'_{333} in TRPV or enough small $|\epsilon_3|$ and $|v_3|$ ($\lesssim$ 1 GeV) gives the dominant branching ratio for this channel even if the LSP is the lightest neutralino. Therefore, there exists a large parameter region where the R-parity violating decay is much more important than loop level and can compete with the three body decay.

$$\tilde{t}_1 \rightarrow b + \tau. \tag{2.26}$$

Chapter 3

Experimental Design

The Collider Detector at Fermilab (CDF) is a general purpose detector to study $p\bar{p}$ collision. The Tevatron accelerator is the highest energy proton-antiproton collider in the world currently. In this chapter, the experimental designs are described.

3.1 Accelerator complex

The Tevatron is a superconducting accelerator of about 1 km of radius. There are several smaller accelerators and storage rings before reaching the final collision with center of mass energies of 1.96 TeV. **Fig. 3.1** shows a pictorial overview of the complex process at Fermilab.

3.1.1 Proton beam

At the first stage of acceleration, the particle including a proton is provided and accelerated by the Cockcroft-Walton. In this device, electrons are added to hydrogen atoms (H_2), and the resulting negative ions (H^-), each consisting of two electrons and one proton, are attracted to a positive voltage and accelerated to about 750 keV.

After leaving the Cockcroft-Walton, the negative hydrogen ions enter into a linear accelerator called the Linac, which is approximately 150 meter long. The Linac consists of nine blue tanks filled with small drift tubes, and these tanks are spaced further and further apart. An electric

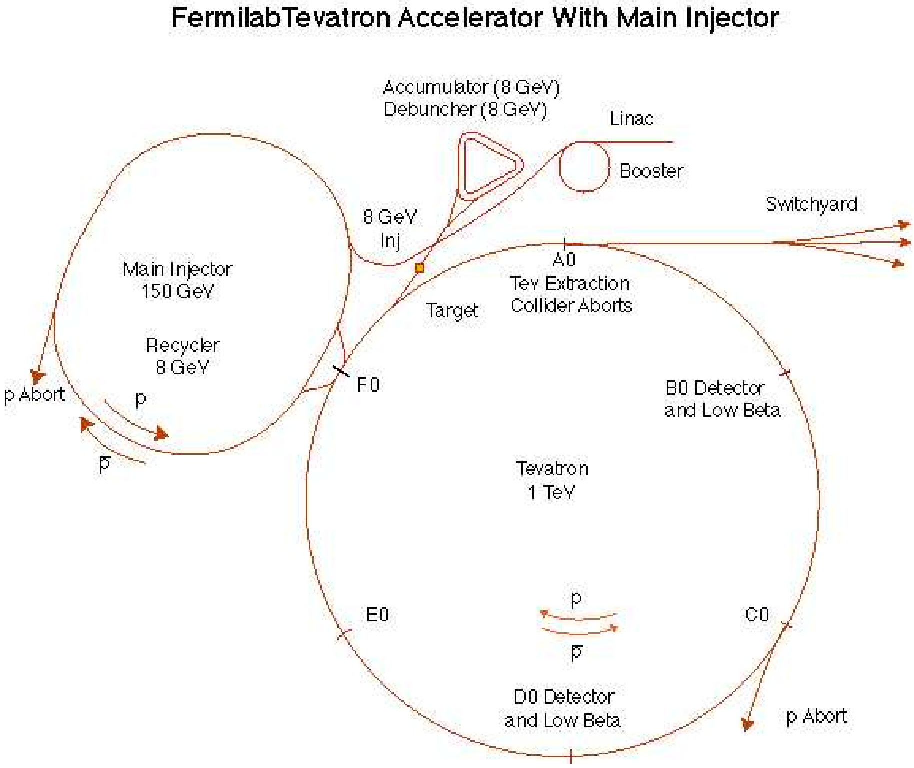

Fig. 3.1. Schematic layout of the Fermilab Accelerator complex.

field is applied to the tubes repeatedly reserving in direction. The negative ions travel through the drift tubes, hiding in them when the electric field is in a direction that would slow them down. And these particles emerge into the gaps between the drift tubes when the field is in the direction to speed them up. In this stage, the negative ions are accelerated from 750 keV to 400 MeV. Before entering the third stage, the ions pass through a carbon foil and lose electrons.

Protons leaving the Linac then go into the Booster accelerator, which is a rapid cycling synchrotron of 150 meter in diameter. After the protons travel around the Booster in a few hundreds of a second, their energy is raised up to 8 GeV.

The accelerated protons up to 8 GeV enter the Main Injector, which is a proton synchrotron ring with ~2 km radius. This apparatus is a major part of the Run II upgrade to the Fermilab accelerator complex. The Main Injector accelerate the protons up to 150 GeV.

After a proton beam is accelerated in the Main Injector, they enter the Tevatron. The Tevatron, 6 km in circumference, containing 1,000 superconducting magnets brings proton beam to 980 GeV.

3.1.2 Antiproton beam

The antiprotons are created at the target section by the proton accelerated to 120 GeV in the Main Injector. The proton beam is focused on the nickel target and a spray of particles containing a small number of antiprotons are created. Antiprotons are produced over a large spread angle on the forward direction. The particle pass through a cylindrical lithium lens to make the parallel antiproton beam. These beam are directed into the Debuncher, where the momentum spread of the antiprotons are reduced by debunching and stochastical cooling. Then, the antipotons are transfered into the Accumulator. When enough antiprotons are stored and cooled in the Accumulator ring, they are transfered back into the Main Injector, accelerated and injected into the Tevatron ring in the opposite direction of the proton beam.

3.1.3 The Tevetron performance

The Tevatron operates with 36 bunches of protons and 36 bunches of antiproton, with 396 ns spacing between bunches in Run II. Each two beams are focused by quadrupole magnets to achieve the highest luminosity at the two collision points around the Tevatron ring, B0 and D0. The CDF experiment is operated at the former point and the D0 experiment at the latter. In comparison with the past Run, two specific features exist in Run II, namely high luminosity and short bunch spacing, thanks mainly to the replacement of Main Ring by Main Injector. **Table 3.1** shows each performance of Run Ib and Run IIa.

Table 3.1. Operational performance in Run Ib and Run IIa.

	Run Ib (1993 ~ 1995)	Run IIa
Energy [GeV]	1800	1960
Typical luminosity [$\mathrm{cm}^{-2}\mathrm{s}^{-1}$]	0.16×10^{31}	0.1-0.8 $\times 10^{32}$
Integrated luminosity [pb^{-1}/week]	3.2	8-15
Number of bunches ($p \times \bar{p}$)	6×6	36×36
Bunch length (rms) [m]	0.60	0.37
Bunch spacing [ns]	~ 3500	396
Protons/bunch	2.3×10^{11}	2.7×10^{11}
Antiprotons/bunch	5.5×10^{10}	3.0×10^{10}
Total Antiprotons	3.3×10^{11}	1.1×10^{12}
Antiproton Production Rate [hr^{-1}]	6.0×10^{10}	1.0×10^{11}

3.2 CDF Detector

The Collider Detector at Fermilab (CDF) is the first general purpose detector built on the Fermilab Tevatron collider. The detector consists of solenoidal magnet, tracking chamber, silicon vertex detector, electromagnetic calorimeter, hadron calorimeter, muon detector and so on. The CDF undergoes improvements for Tevatron Run II at present partly because the requirement for Run II environment is harder than that of Run I. The layout of the CDF II detector is shown in **Fig. 3.2**. In this chapter each part of the detector is briefly illustrated.

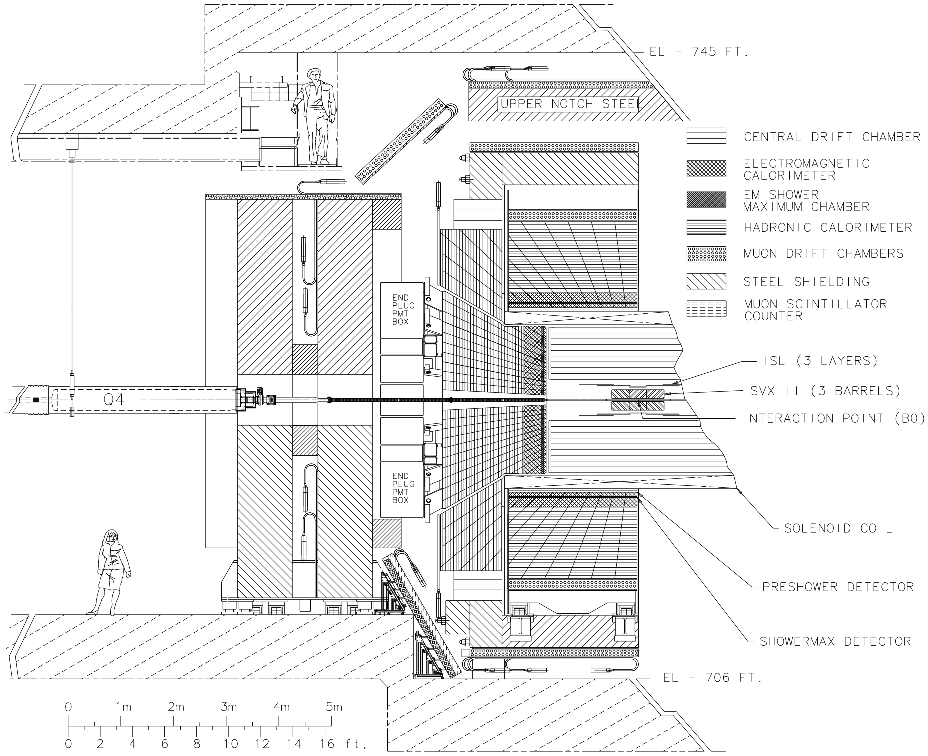

Fig. 3.2. Elevation view of one half of the CDF II Detector.

3.2.1 Tracking Systems

Tracking systems are placed inside a superconducting solenoid, 1.5 m in radius and 4.8 m in length, which generates a 1.4 T magnetic field parallel to the beam axis. These systems have mainly three parts, namely Central Outer Tracker (COT), Silicon Vertex Detector (SVX) and Intermediate Silicon Layer (ISL) (See **Fig. 3.3**).

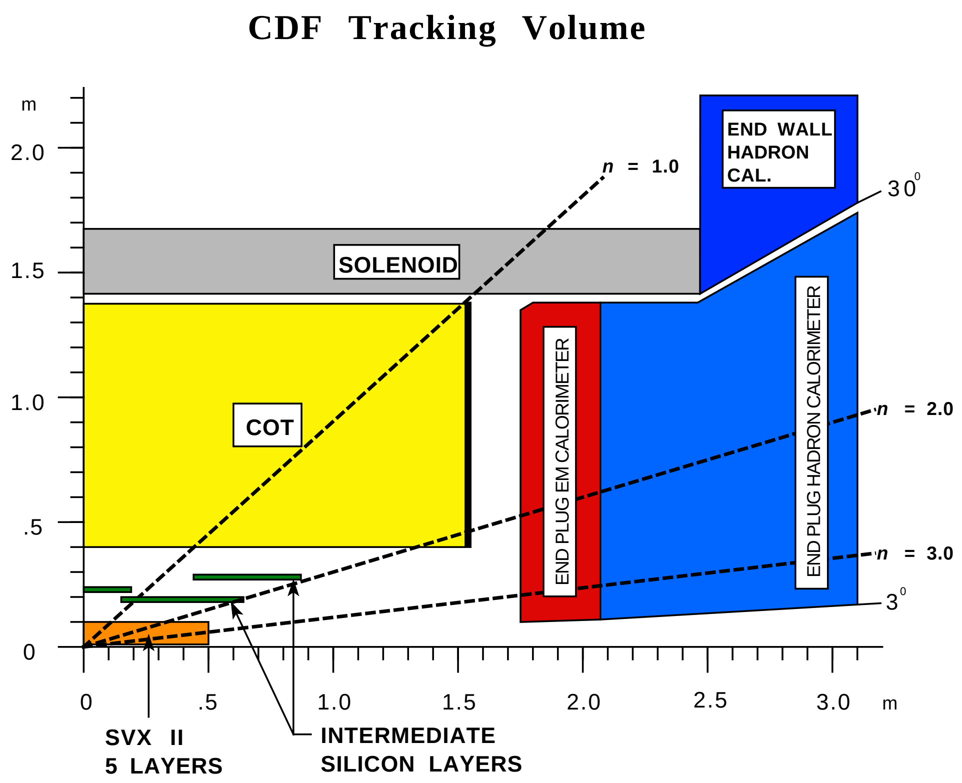

Fig. 3.3. Design of tracking system for the CDF II.

COT, covering radii between 44 and 132 cm in the region $|\eta| \lesssim 1.0$, is composed of small drift cells filled with Ar-Et gas, which has a drift velocity of $\sim$200 μs/ns. 96 sense wire layers in COT are grouped into eight SuperLayers (SL). Four superlayers are placed on the axial side and the others are on the stereo side with a small stereo angle of $\pm 3^\circ$. Each superlayer is alternated and holds a number of cells, the geometry of which is illustrated in **Fig. 3.4**. The basic drift cell has a line of 12 sense wires alternating with shaper wires every 3.8 mm. Total number of drift cells is 2520, so 30,240 readout channels are linked to TDC (Time to Digital Converter) which is standard for CDF II wire chamber systems, and the tracking information will be available for the primary stage of data acquisition. The momentum resolution of COT, $\delta p_T/p_T^2$, is approximately 0.3 % (GeV/c)$^{-1}$.

On the other hand, an inner track is assigned to SVX and ISL. Firstly, SVX is built on three cylindrical barrels, with a total length of 96 cm and covering $\sim 2.5\sigma$ of the luminous region. There are 12 wedges in ϕ, each with five radial layers of double sided silicon microstrip detectors between 2.4 and 10.7 cm. Sensors in all five layers have one side for measurements

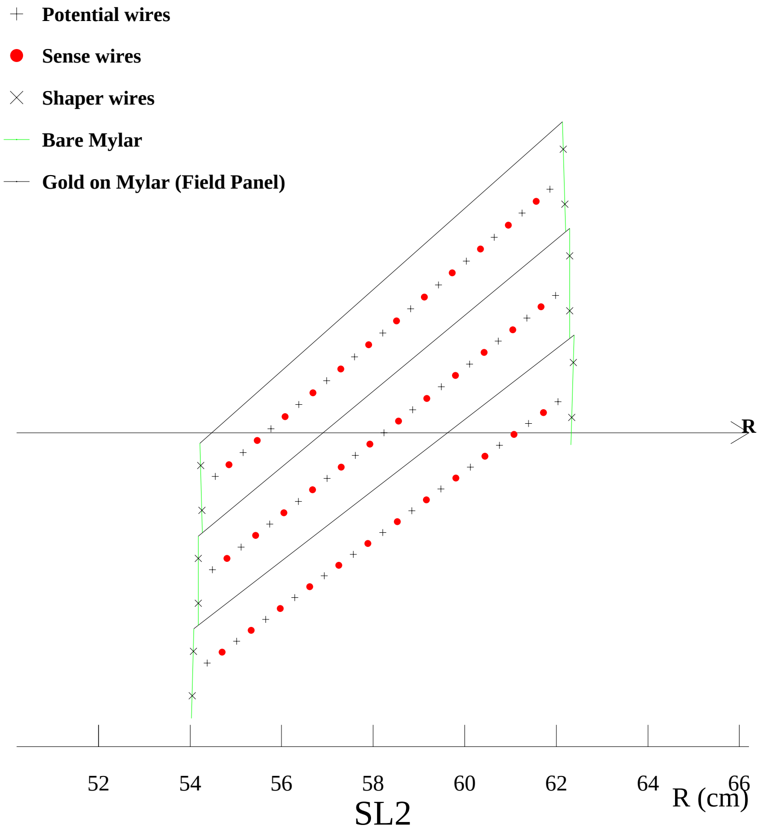

Fig. 3.4. Nominal cell layout for SL2. R represents the distance from beam line.

in the r-ϕ plane. On the first, second and fourth layers from the inner side, there are sensing strips for the measurement in the r-z plane on the other side. The remaining two layers (third and fifth) have a second side with sensing strips which are on the tilt of 1.2° in relation to the first set. This systems have 405,504 channels, connecting to radiation hardened readout chips mounted on the surface of the silicon detectors. Each readout chip set has 128 channels, each with a charge-sensitive amplifier, a 42-cell dual-ported pipeline with four additional cells for buffers, and an ADC (Analog to Digital Converter).

In the next place, ISL consists of three layers. In central region, $|\eta| \lesssim 1.0$, a single ISL layer is placed at a radius of 22 cm, while in the plug region, $1.0 \lesssim |\eta| \lesssim 2.0$, two layers of silicon are placed at radii of 20 and 28 cm. The ISL readout electronics are identical to the SVX II and the read out segmentation is in 30° wedges which exactly match the SVX II segmentation.

It is emphasized that SVX II and ISL together are a single function system which standalone silicon tracking and b-tagging over the full region $|\eta| \lesssim 2.0$.

Table 3.2 shows the designed parameters of the tracking systems.

Table 3.2. Design parameters of the baseline tracking systems.

COT	
Number of superlayers	8
Radial coverage	44 to 132 cm
Rapidity coverage	$\lvert\eta\rvert \leq 1.0$
Number of channels	30,240
Resolution per measurement	180 μm
Measurements per superlayers	12
Maximum drift distance	0.88 cm
SVX II	
Number of layers	5
Radial coverage	2.4 to 10.7 cm
Rapidity coverage	$\lvert\eta\rvert \leq 2.0$
Total length	96.0 cm
Number of channels	405,504
Resolution per measurement	12 μm (axial)
ISL	
Number of layers	1 for $\lvert\eta\rvert < 1.0$; 2 for $1.0 < \lvert\eta\rvert < 2.0$
Radial coverage	20 to 28 cm
Rapidity coverage	$\lvert\eta\rvert \geq 1.9$
Total length	174 cm
Number of channels	268,800
Resolution per measurement	16 μm (axial)

3.2.2 Calorimeter System

The CDF II calorimeter systems surround the tracking volume and the solenoid with two separated devices of the electromagnetic (EM) and hadronic (HA) calorimeters. The CDF calorimeters have a uniform pattern of matched projective towers of EM and HA calorimeters.

The central calorimeters (CEM and CHA) are constructed of 24 wedges (15°) in ϕ, and 10 towers (~ 0.1) in $|\eta| \lesssim 1.1$ for CEM and $|\eta| \lesssim 0.9$ for CHA, containing a crack region around $\eta = 0$. In plug region, the segmentation of the plug calorimeters (PEM and PHA) consists of 48 wedges (7.5°) and 8 towers (~ 0.1) in $1.1 \lesssim |\eta| \lesssim 1.8$, and 24 wedges (15°) and 4 towers ($0.2 \sim 0.6$) in $2.1 \lesssim |\eta| \lesssim 3.6$. The endwall hadronic calorimeter (WHA) covers a gap between

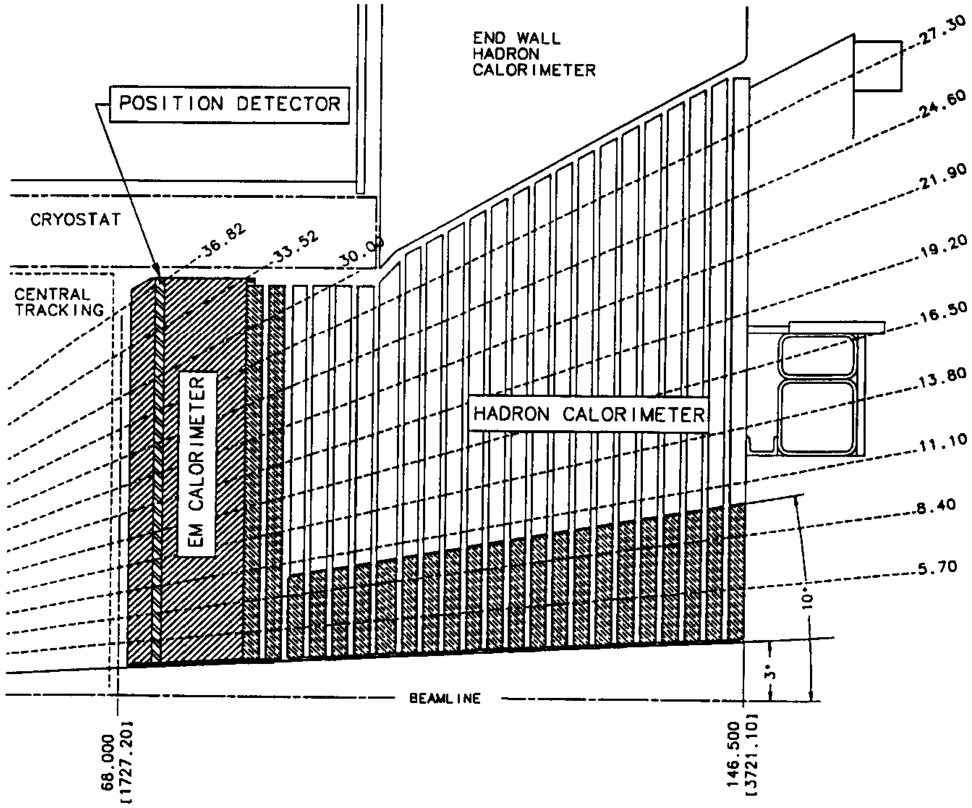

Fig. 3.5. Cross section of upper part of new end plug calorimeter.

the central and plug hadronic sections. **Figure 3.5** shows the layout of the detector and the coverage.

The EM calorimeters are a lead/scintillator sampling device made of the sandwiched structure of 31 layers for CEM and 23 layers for PEM, respectively. The HA calorimeters contain 32 layers and 23 layers of alternating iron and scintillator for CHA and PHA, respectively. Also the wall hadron (WHA) calorimetry is constructed of 15 layers of iron absorber alternating with plastic scintillator. Characteristics of the CDF II calorimeter are summarized in **Table 3.3**.

The EM shower position is measured by a shower max detector (CES, PES) and pre-shower detector (CPR). The CES is a multi-wire proportional chamber embedded near the shower maximum (approximately $6X_0$, where X_0 is radiation length) into the CEM calorimeters. The

Table 3.3. Characteristics of the CDF II calorimeter. In the rows corresponding to light yield, photoelectrons is abbreviated as "p.e.".

	Central and End-wall	Plug
EM:		
Thickness	$19X_0$, 1λ	$21X_0$, 1λ
Sample (Pb)	$0.6X_0$	$0.8X_0$
Sample (scint.)	5 mm	4.5 mm
Light yield	160 p.e./GeV	300 p.e./GeV
Sampling resolution	$11.6\%/\sqrt{E_T}$	$14.\%/\sqrt{E_T}$
Stochastic resolution	$14.\%/\sqrt{E_T}$	$16.\%/\sqrt{E_T}$
HAD:		
Thickness	4.5λ	1λ
Sample (Pb)	1 inch. (central) 2 inch. (end-wall)	2 inch.
Sample (scint.)	10 mm	6 mm
Light yield	40 p.e./GeV	30 p.e./GeV
Energy resolution	$75.\%/\sqrt{E_T} + 3.\%$	$80.\%/\sqrt{E_T}$+$5.\%$

anode wires are strung parallel to the beam axis and the cathode strips to that perpendicular direction (r-ϕ). Another wire chamber is placed immediately placed in front of CEM to act as a pre-shower detector (CPR). In the plug region, two scintillator layers act as the shower maximum (PES) and pre-shower detectors. PES consists of the scintillator-based strip readout divided into eight 45° sectors. Each sector contains two layers (called U and V) of 5 mm pitch scintillator strips. The U and V layers are aligned at $+22.5°$ and $-22.5°$ with respect to the radial dimension to provide two-dimensional position measurement, and are inserted into the fifth sampling slot ($\sim X_0$) within PEM calorimeter. The first layer in PEM is used as a pre-shower detector.

The electron track matching and the lateral EM shower profile in CES and PES are very powerful to separate the electron, photon, and the photons from the neutral pions.

3.2.3 Muon System

The CDF II muon detectors are composed of four systems of scintillators and proportional chambers in the region of $|\eta| \lesssim 2.0$. The absorbers for these systems are the steel in calorimeters, the magnet return yoke, additional steel walls, and the steel from the Run I forward muon toroids.

The Central MUon detector (CMU) is a set of single-wire drift tubes consisted of 144 modules with 16 rectangular cells per module, located behind CHA, which provides approximately $\sim 5.5\lambda$ of absorber.

The Central Muon uPgrade (CMP) is a second set of muon chambers behind an additional 60 cm of steel in the region $55^\circ \leq \theta \leq 90^\circ$. CMP is a fixed length in z, vary in η, and form a box around CMU. A layer of scintillation counters (CSP) is also installed on outside the surface of CMP.

The Central Muon eXtension (CMX) consists of conical sections of drift tubes and scintillation counters (CSX) located at each end of the central detector and extending in polar angle from 42° to 55°. There is a 30° gap of the azimuthal coverage in CMX/CSX at the top of the detector for Tevatron Main Ring used in Run I and the solenoid refrigerator.

The Intermediate MUon detector (IMU) is designed to trigger on muons with $|\eta| \lesssim 1.5$ and to identify offline muons with $|\eta| \lesssim 2.0$. IMU is almost the same configuration with the CMX/CSX, a set of drift tubes with four layer, located behind the plug calorimeter ($6 \sim 20\lambda$ of steel). The forward muon toroidal magnet used in Run I is re-used as the absorber without energizing. Additionally, a ring of steel ~ 60 cm is welded onto the inner face of the toroids. The muon momentum is measured using solenoidal magnet field, where the silicon detector gives a good momentum resolution.

The detailed design parameters of the central muon detectors are given in **Table 3.4**, and a schematic view of the coverage of each detector is shown in **Fig. 3.6**.

3.2.4 Trigger and data acquisition systems

Since collision events with the average size of 250 kb in a 396 ns bunch-crossing rate give an extremely large amount of data, disk space needed to store all of this information would be overwhelming. To reduce the data size stored on disk we implement an outline selection, the

Table 3.4. Characteristics of the CDF II muon detector.

	CMU	CMP/CSP	CMX/CSX	IMU
Coverage	$\|\eta\| \lesssim 0.6$	$\|\eta\| \lesssim 0.6$	$0.6 \lesssim \|\eta\| \lesssim 1.0$	$1.0 \lesssim \|\eta\| \lesssim 1.5$
Drift tubes:				
Thickness [cm]	2.68	2.5	2.5	2.5
Width [cm]	6.35	15	15	8.4
Length [cm]	226	640	180	363
Max drift time [ns]	800	1400	1400	800
Total drift tubes	2304	1076	2208	1728
Scintillator:				
Thickness [cm]	-	2.5	1.5	2.5
Width [cm]	-	30	$30 \sim 40$	17
Length [cm]	-	320	180	180
Total counters	-	269	324	864
Pion interaction lengths	5.5λ	7.8λ	6.2λ	$6.2 - 20\lambda$
Min. muon p_T [GeV/c	1.4	2.2	$1.4 \sim 2.0$	

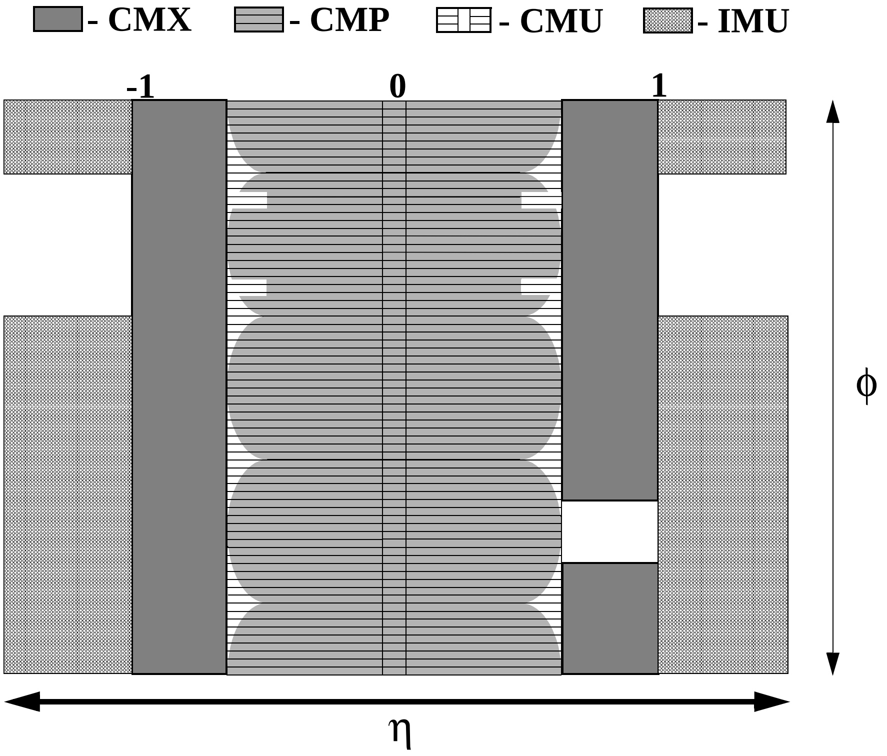

Fig. 3.6. Location of the central muon upgrade components in azimuth ϕ and pseudorapidity η for Run II.

trigger.

Triggers are sets of requirements which are based on the identification of particles and their measured kinematics. The detectors are read out into a three-tiered trigger system. The Level 1 (L1), Level 2 (L2), and Level 3 (L3) trigger requirements are combined into a logical unit called a trigger path. Trigger tables are made up of many trigger paths, to cover the wide range of physics interests at CDF. We have many different trigger tables, each providing a different functionality. (See Chapter 4 for a discussion of triggers used in this thesis).

Our trigger system is a deadtime-less trigger, with total trigger deadtime typically of the order of $\lesssim 5\%$. Each level of trigger provides a rate reduction; 40 kHz acceptable rate at L1, 300 Hz for L2, and 30-50 Hz at L3 trigger stage. **Figure 3.7** shows the functional block diagram of the readout electronics.

L1 can make a decision to accept or reject an event based on calorimeter energy, muon depositions, or track information. The remarkable change for L1 in Run II upgrade is the addition of track finding, which was previously available only at L2. The 2-dimensional track reconstruction (XFT, the eXtremely Fast Tracker) allows to identify an electron or a muon object at L1, or to use the kinematic properties of observed track pairs. The XFT tracks must be sent to the calorimeter and muon streams as well as the track only system, because the electron and muon triggers require the presence of a track pointing at the corresponding outer detector element. At this stage the data rate is reduced from 2.5 MHz down less than 20 kHz.

Events accepted by the L1 system are processed by the L2 hardware. L2 uses programmable processor which provides decision based on calorimeter energy and track information. The most significant addition to the L2 trigger is Silicon Vertex Tracker (SVT) which provides the track impact parameter with high precision. Thus, the secondary vertex information is available at L2 triggering. Moreover, there is an access to data from the shower max detector for improved identification of electrons and photons, and jet reconstruction through a cluster finding algorithm in the L2 calorimeter boards. L2 provides a factor of 100 reduction over L1, passing on a 300 Hz rate into L3.

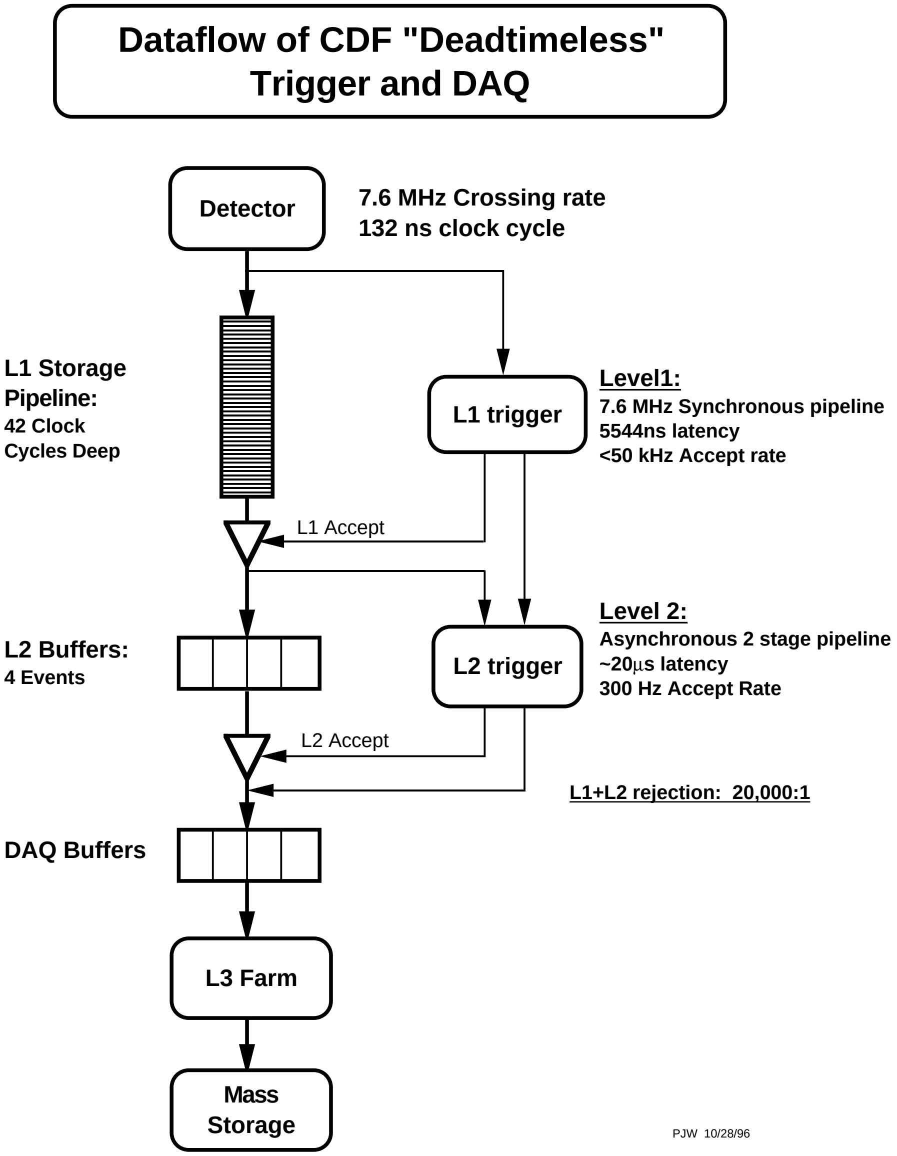

Fig. 3.7. The Run II readout functional block diagram.

Once events pass the L2 triggers the EVent Builder (EVB) assembles those event fragments into one data block and delivers it to the L3 trigger system. L3 is a farm of approximately 300 CPU's, each fully analyzing a single event. After passing through the L3 trigger, the Data Logger system delivers events to the tape device, or online monitoring processes which verify the entire detector and trigger systems are working properly. The L3 reconstruction program is the same as offline event analysis, which produces reconstructed objects, such as CdfEmObject for an electron, CdfMuon for a muon, and CdfTau for a tau. A maximum rate of 75 Hz can pass L3 and be written out to tape.

Chapter 4

The Lepton plus Track Trigger

We describe the implementation of the lepton plus track trigger and the evolution in details since its installation in this chapter. Also the various physics topics that can be addressed with this trigger both within and beyond the SM are picked up. We point out the complementarity with respect to the dynamical and geometrical acceptances as compared to other triggers and also emphasize the necessity of these triggers for some important physics issues. Finally we discuss possible ways of extending these triggers by using other new capabilities of the CDF II.

4.1 Introduction

At the SUSY-Higgs Workshop in 1998 at FNAL [42, 43, 44, 45], a group of people pointed out the importance of building a low E_T dilepton trigger that could also include τ-leptons. One of the motivations was the fact that the SUSY results both from limits on the Higgs mass at LEP 200 and from CDM constraints, favor a rather large value for tanβ ($5\sim55$). This means an enhancement in the branching ratios of the decays of SUSY particles (including SUSY Higgs) into τ-leptons as compared to other charged leptons. Another motivation was the improved capability of the CDF detector for Run II, especially for tracking, with a special mention of the XFT trigger system that allows for the first time the inclusion of the COT tracking information at the L1 trigger.

Thus the lepton plus track triggers were proposed in order to detect events with two leptons ($ee, e\mu, \mu\mu, e\tau_h$, and $\mu\tau_h$) where τ_h indicates the τ-lepton decaying hadronically, and the e or μ can be either directly produced or through the leptonic decay of the τ-lepton (τ_ℓ). In this latter case, two last signatures could represent $\tau_\ell\tau_h$ dileptons. **Table 4.1** summarizes the branching ratios of τ-lepton and the final states in ditau events. Almost half of ditau events has $\tau_\ell\tau_h$ in the final states. Though the $\tau_h\tau_h$ final state has the second largest ratio, it is difficult to reject large backgrounds from QCD. Therefore to detect $\tau_\ell\tau_h$ is very important.

Table 4.1. The branching ratios of single tau and the final states in ditau events. $h^\pm$ represent charged mesons, almost $\pi^\pm$ or $K^\pm$.

Decay Mode	Branching Ratio
Single τ:	
$\tau^- \to e^-\bar{\nu}_e\nu_\tau$	17.8 %
$\tau^- \to \mu^-\bar{\nu}_\mu\nu_\tau$	17.4 %
$\tau^- \to h^-\nu_\tau + X$ (1-prong)	49.5 %
$\tau^- \to h^-h^-h^+\nu_\tau + X$ (3-prong)	15.2 %
Di-τ:	
$\tau\tau \to \tau_\ell\tau_\ell$	12.4 %
$\tau\tau \to \tau_\ell\tau_h$	45.6 %
$\tau\tau \to \tau_h\tau_h$	42.0 %

The first detailed studies for the electron plus track [46] and the muon plus track [47] triggers were achieved for the case of the foreseen high luminosity for Run II. The selection criteria and thresholds applied by the trigger system were carefully estimated in order to obtain the best compromise between keeping a reasonable rate and applying the lowest possible E_T and/or p_T cuts on both leptons. Subsequently, these were accepted to be included as official Run II triggers [48] and the implementation in the experiment was achieved in January 2002. Being faced with real running conditions, the definitions of the triggers have been slightly modified as compared to the original ones and were evolved according to the changes in the experiment occurring since January 2002.

4.2 Evolution of the lepton plus track triggers

The modifications applied to the lepton plus track triggers since their installation in January 2002 are detailed in this section, for each lepton case, namely: (i) electrons with the CEM detector, muons as measured both with (ii) the CMU/P and (iii) the CMX detectors.

4.2.1 The electron plus track trigger

The original design of the electron plus track trigger, labeled as TAU_ELECTRON8_TRACK5_ISO (TAU_ELE), is described in Ref. [46]. However the trigger used in the actual data taking is a little bit different and it has evolved since its installation in January 2002.

Table 4.2 gives, for each trigger level, and for each trigger version, the corresponding detailed list of cuts and conditions. The refinements in L2 and furthermore in L3 of the trigger selection are shown. The selection of the electron plus track trigger starts at L1, by requiring a single EM tower at least 8-GeV in E_T and an associated XFT track of at least 8-GeV/c in p_T. L2 tightens the electron identification by requiring the CES E_T larger than 2 GeV and by demanding a second XFT track of 5 GeV/c. L3 refines these conditions and furthermore requires a charged track isolation around the track reconstructed at L3; this isolation criterion is typical of a τ-jet. It should be noted that the main difference is due to L2. The CES requirement for the electron is added as well as a second track making an azimuthal angle with the lepton track of at least 10 degrees is demanded.

Table 4.3 gives the definitions of the trigger path and the average cross-section for the TAU_ELE trigger over good runs in each version. The average cross-section evolves from 44 nb in version 1 (before AAA) to 50 nb in version 1 (after AAA), where AAA means the problem for an electron reconstruction at L3 that led to a CdfEmObject without associated track even if this object was an electron candidate. The electron plus track trigger is affected by this bug and this explains the slightly lower value in the cross-section for version 1 with AAA as compared

Table 4.2. Cuts for TAU_ELE at L1, L2 and L3.

Trigger Name	Cuts
Level 1	
L1_CEM8_PT8_v-2	· Seed tower $E_T \geq 8$ GeV in central · $E_{had}/E_{em} \leq 0.125$ if $E_T < 16$ GeV · "4 layer" XFT $p_T \geq 8.0$ GeV/c pointing to the seed tower
L1_CEM8_PT8_v-4	· Seed tower $E_T \geq 8$ GeV in central · $E_{had}/E_{em} \leq 0.125$ if $E_T < 16$ GeV · "4 layer" or "3 layer" XFT $p_T \geq 8.0$ GeV/c pointing to the seed tower
Level 2	
L2_CEM8_PT8_v-4	· Cluster seed $E_T \geq 8$ GeV in central, shoulder $E_T \geq 7.5$ GeV · $E_{had}/E_{em} \leq 0.125$ · "4 layer" XFT $p_T \geq 8.0$ GeV/c pointing to the seed
L2_CEM8_PT8_CES2_v-1	· Same as L2_CEM8_PT8_v-4 · CES $E \geq 2.0$ GeV
L2_CEM8_PT8_CES2_ &_TRK5_DPHI10_v-1	· Same as L2_CEM8_PT8_CES2_v-1 · Second "4 layer" XFT $p_T \geq 5.0$ GeV/c · The angle between 1st and 2nd XFT is $\geq 10°$
Level 3	
L3_ELECTRON8_ TRACK5_ISO_v-1	[Electron Side] · $E_T \geq 8$ GeV (Calculated with $z_0 = 0$) · $p_T \geq 8$ GeV/c · $\lvert\Delta z\rvert \leq 8.0$ cm · $\chi^2_{strip} \leq 20$ [Iso. Track Side] · $p_T \geq 5$ GeV/c · $\lvert\eta\rvert \leq 1.5$ · no track with $p_T > 1.5$ GeV/c and $\lvert\Delta z_0\rvert < 15$ cm in $0.175 \leq \Delta R \leq 0.524$ [Other Cuts] · $\lvert z_0(e) - z_0(trk)\rvert \leq 15$ cm · $\Delta R(e, trk) \geq 0.175$
L3_ELECTRON8_ TRACK5_ISO_v-2	· Same as L3_ELECTRON8_TRACK5_ISO_v-1 but based on v4.8.4
L3_ELECTRON8_ TRACK5_ISO_v-3	· Same as L3_ELECTRON8_TRACK5_ISO_v-2 but E_T is calculated with track z_0

Table 4.3. Evolution of the definition of the TAU_ELE trigger and the corresponding average cross section (σ).

Ver.	Level 1	Level 2	Level 3	Ave. σ [nb]
1	L1_CEM8_PT8_v-2	L2_CEM8_PT8_v-4	L3_ELECTRON8_ TRACK5_ISO_v-1	44.0 (Before AAA) 50.1 (After AAA)
2	L1_CEM8_PT8_v-2	L2_CEM8_PT8 _CES2_v-1	L3_ELECTRON8_ TRACK5_ISO_v-1	38.8
4	L1_CEM8_PT8_v-4	L2_CEM8_PT8_CES2_ &_TRK5_DPHI10_v-1	L3_ELECTRON8_ TRACK5_ISO_v-1	28.8 (XFT v1) 26.1 (XFT v2)
5	L1_CEM8_PT8_v-4	L2_CEM8_PT8_CES2_ &_TRK5_DPHI10_v-1	L3_ELECTRON8_ TRACK5_ISO_v-2	27.1
6	L1_CEM8_PT8_v-4	L2_CEM8_PT8_CES2_ &_TRK5_DPHI10_v-1	L3_ELECTRON8_ TRACK5_ISO_v-3	26.7

with the one for version 1 after AAA is cured. Then version 2 gives 39 nb and it is reduced to 29 nb in version 4 (XFT v1). In addition, XFT finder design is changed from “two miss” to “one miss” in every layer during running version 4. As a result, the average cross-section goes down to 26 nb in version 4 (XFT v2). Version 5 leads to a small increase of the average cross-section to 27 nb as the CDF offline softwares for reconstruction and filtering at L3 are upgraded from version 4.3.0 to version 4.8.4 which is changed in CdfEmObject clustering algorithm. Finally, version 6 calculates E_T with track z_0 at L3 but the average cross-section is not changed.

4.2.2 The muon plus track trigger

The original design of the muon plus track trigger was proposed in Ref. [47]. Here, we describe in more detail the implementation for this trigger, as it is currently functioning. Two cases are considered corresponding to a muon triggered (i) by the CMU and CMP detectors and (ii) by the CMX detector. They are labeled as TAU_CMUP8_TRACK5_ISO (TAU_CMUP) and as TAU_CMX8_TRACK5_ISO (TAU_CMX), respectively. The same corresponding tables as in the electron case are presented for each muon case.

Table 4.4. Cuts for TAU_CMUP at L1, L2 and L3.

Trigger Name	Cuts
Level 1	
L1_CMUP6_PT4_v-1	· CMU stub $p_T \geq 6$ GeV/c · CMP stub $p_T > 3$ GeV/c · Number of CMP hit layers > 2 · "4 layer" associated XFT $p_T \geq 4$ GeV/c
L1_CMUP6_PT4_v-2	· Same as L1_CMUP6_PT4_v-1
Level 2	
L2_AUTO_L1_CMUP6_PT4_v-1	· Auto accept
L2_TRK8_L1_CMUP6_PT4_v-1	· XFT $p_T \geq 8$ GeV/c
L2_TRK8_L1_CMUP6_PT4_v-2	· Same as L2_TRK8_L1_CMUP6_PT4_v-1
Level 3	
L3_CMUP8_TRACK5_ISO_v-1	[Muon Side] · $p_T \geq 8$ GeV/c · $\|\Delta x\|_{CMU} < 15.0$ cm · $\|\Delta x\|_{CMP} < 20.0$ cm [Iso. Track Side] · $p_T \geq 5$ GeV/c · $\|\eta\| \leq 1.5$ · no track with $p_T > 1.5$ GeV/c and $\|\Delta z_0\| < 15$ cm in $0.175 \leq \Delta R \leq 0.524$ [Other Cuts] · $\|z_0(e) - z_0(trk)\| \leq 15$ cm · $\Delta R(e, trk) \geq 0.175$
L3_CMUP8_TRACK5_ISO_v-2	· Same as L3_CMUP8_TRACK5_ISO_v-1 but based on v4.8.4.

The CMUP plus track trigger

This trigger was changed once in L2 since its installation. **Table 4.4** gives the detailed trigger selection for each level of the trigger system. Here, L1 is again a rather low E_T and p_T inclusive muon trigger of 6 GeV/c, with a "4 layer" XFT track associated to the muon stub. L2, contrary to the electron case, is just an "auto-accept" as the L2 muon system is not yet currently operational in version 2. However, a "4 layer" XFT track above 8 GeV/c, which is not required to be associated to the muon stub in version 2, is required in version 3. Then, L3 requires another track of at least 5 GeV/c and with an isolation characteristic of a hadronically decaying τ.

Table 4.5. Evolution of the definition of the TAU_CMUP trigger and the corresponding average cross section (σ).

Ver.	Level 1	Level 2	Level 3	Ave. σ [nb]
2	L1_CMUP6_PT4_v-1	L2_AUTO_L1_ CMUP6_PT4_v-1	L3_CMUP8_ TRACK5_ISO_v-1	10.9 (XFT v1) 9.3 (XFT v2)
3	L1_CMUP6_PT4_v-1	L2_TRK8_ L1_CMUP6_PT4_v-1	L3_CMUP8_ TRACK5_ISO_v-1	8.2
5	L1_CMUP6_PT4_v-2	L2_TRK8_ L1_CMUP6_PT4_v-1	L3_CMUP8_ TRACK5_ISO_v-2	9.6
6	L1_CMUP6_PT4_v-2	L2_TRK8_ L1_CMUP6_PT4_v-2	L3_CMUP8_ TRACK5_ISO_v-2	9.2

Table 4.5 is a summary of the definitions for trigger path and the average cross-section for the TAU_CMUP trigger in each trigger table. The average cross-sections are 11 nb and 9 nb in version 2 (XFT v1) and (XFT v2), respectively. Similar to the electron plus track trigger, the design of XFT gives smaller cross-section in XFT v2. Then the decrease to 8 nb can be seen in version 3 because of the requirement for an 8-GeV/c XFT track at L2. A small increase of cross-section to 10 nb seen in version 5 is similar to the electron plus track case.

The CMX plus track trigger

Table 4.6 gives the corresponding cuts and conditions for L1, L2 and L3 in each trigger version.

Table 4.7 lists the definitions of the trigger path and the average cross-section for good runs. One notes that there are three versions for this trigger (version 1, 2 and 3) that differ by L1. However, the detailed description of this trigger does not exhibit any difference between the three versions of L1 (See **Table 4.6**). Also, in the case of CMX, the change of XFT design gives a smaller cross-section.

4.2.3 Summary

Three types of the lepton plus track triggers, (i) CEM plus track, (ii) CMUP plus track, and (iii) CMX plus track, are implemented where p_T(lepton)>8GeV/c and p_T(track)>5GeV/c.

Table 4.6. Cuts for TAU_CMX at L1, L2 and L3.

Trigger Name	Cuts
Level 1	
L1_CMX6_PT8_PS1_v-1	· CMX stub $p_T \geq 6$ GeV/c · Long associated XFT $p_T \geq 8$ GeV/c
L1_CMX6_PT8_PS1_v-2	· Same as L1_CMX6_PT8_PS1_v-1
L1_CMX6_PT8_CSX_PS1_v-1	· Same as L1_CMX6_PT8_PS1_v-1
L1_CMX6_PT8_CSX_v-1	· Same as L1_CMX6_PT8_PS1_v-1 · CSX required
Level 2	
L2_AUTO_L1_CMX6_PT8_v-1	· Auto accept
L2_AUTO_L1_CMX6_PT8_CSX_v-1	· Auto accept
Level 3	
L3_CMX8_TRACK5_ISO_v-1	[Muon Side] · $p_T \geq 8$ GeV/c · $\lvert\Delta x\rvert_{CMX} < 30.0$ cm [Iso. Track Side] · $p_T \geq 5$ GeV/c · $\lvert\eta\rvert \leq 1.5$ · no track with $p_T > 1.5$ GeV/c and $\lvert\Delta z_0\rvert < 15$ cm in $0.175 \leq \Delta R \leq 0.524$ [Other Cuts] · $\lvert z_0(e) - z_0(trk)\rvert \leq 15$ cm · $\Delta R(e, trk) \geq 0.175$
L3_CMX8_TRACK5_ISO_v-2	· Same as L3_CMX8_TRACK5_ISO_v-1 but based on v4.8.4.

Table 4.7. Evolution of the definition of the TAU_CMX trigger and the corresponding average cross section (σ).

Ver.	Level 1	Level 2	Level 3	Ave. σ [nb]
1	L1_CMX6_PT8_PS1_v-1	L2_AUTO_L1_CMX6_PT8_v-1	L3_CMX8_TRACK5_ISO_v-1	4.5
2	L1_CMX6_PT8_PS1_v-2	L2_AUTO_L1_CMX6_PT8_v-1	L3_CMX8_TRACK5_ISO_v-1	4.5 (XFT v1) 5.1 (XFT v2)
3	L1_CMX6_PT8_CSX_PS1_v-1	L2_AUTO_L1_CMX6_PT8_CSX_v-1	L3_CMX8_TRACK5_ISO_v-1	4.6
5	L1_CMX6_PT8_CSX_v-1	L2_AUTO_L1_CMX6_PT8_CSX_v-1	L3_CMX8_TRACK5_ISO_v-2	5.7

They are running stably at the trigger cross-sections of 27 nb, 9.7 nb, and 5.7 nb, respectively. **Figure 4.1** shows the typical trigger cross section at L1, L2, L3 and physics events, $Z \to \ell\ell$ and stop ($M_{\tilde{t}_1} = 100$ GeV/c^2) pair production. It is shown that the lepton plus track triggers produce good reduction at each level. The datasets from those triggers are ready for the SM physics, such as $Z \to \tau\tau$, as well as beyond the SM physics that include two tau leptons in the final states.

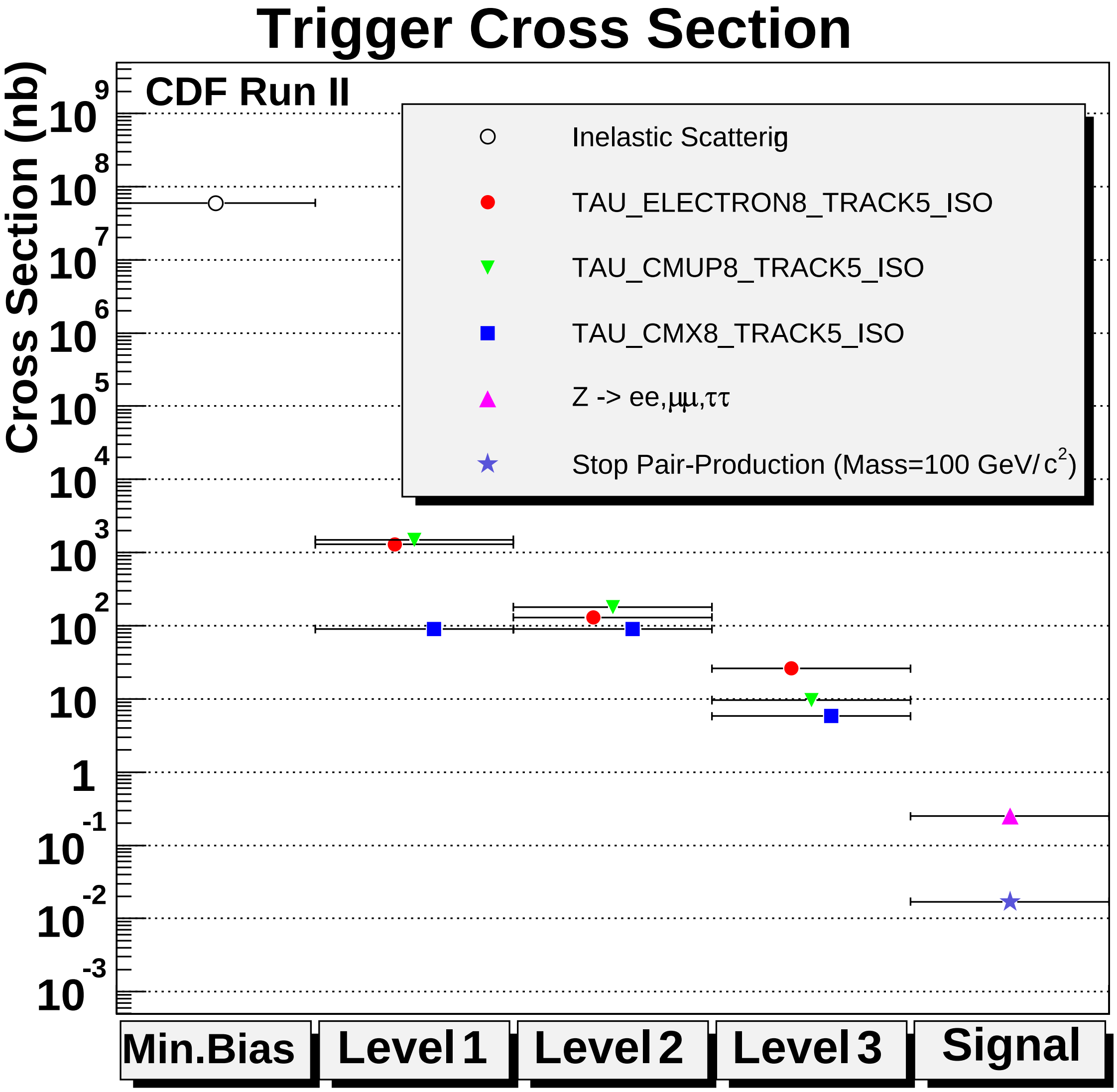

Fig. 4.1. The reduction of trigger cross section at each trigger level.

4.3 Physics topics addressed by the lepton plus track trigger

The lepton plus track trigger is a class of low momentum dilepton triggers to select events containing charged leptons, including τ's, in the final state. Taus decay in leptonic (35%) and hadronic (65%) modes. Dilepton events, where both leptons are τ's, can be identified by accessing $\tau_e\,\tau_e$, $\tau_e\tau_\mu$, $\tau_e\tau_h$, or $\tau_\mu\tau_h$. Then the fully accessible final states are: $e\,e$, $e\,\mu$, $e\,\tau_h$, $\mu\,\mu$, $\mu\,\tau_h$, $\tau_h\,\tau_h$.

In the case of a hadronic decay, the "τ-jetiness" is ensured by an isolation criteria applied around the second track at L3. As a corollary, this prevents the track from being a product of a light quark or heavy flavored quark jet. This point will be discussed in more detail in the next section.

Low p_T dileptons are a basic element for many and very important signatures, both in the SM physics and in searches for physics beyond the SM. The main goal of this section is then to give a mini-review of the possible applications of the lepton plus track trigger.

Because of the XFT track requirement for both the lepton and the second tracks, this trigger is restricted to the central region. Extending its geometrical acceptance will be part of the discussion in the next section.

The complementarity and necessity of this trigger with respect to other triggers actually running in the experiment are emphasized. In **Table 4.8**, we briefly summarize each of these triggers, η coverage, primary E_T (or p_T) thresholds along with the use of the XFT and/or the SVT trigger systems. It allows to address the overlaps, complementarity or uniqueness of the lepton plus track trigger with respect to the others, in terms of geometrical acceptance and accessible domains in p_T. This last point, of course, has an influence on the accessibility of some physics topics. The comparison with the other relevant triggers is done for each physics topics discussed in the following two subsections.

Table 4.8. Main characteristics of some relevant triggers as compared with those of the lepton + track trigger.

Trigger Type	η coverage	Thresholds	Requirements		
			XFT	SVT	Other
Lepton +Track	$\|\eta\| < 1.0$	$E_T^e(p_T^\mu) \geq 8$ GeV(/c) Track $p_T \geq 5$ GeV/c	yes	no	Iso. for track
Dilepton (C-C)	$\|\eta\| < 1.0$ (no CMX-CMX)	$E_T^e(p_T^\mu) \geq 4$ GeV(/c)	yes	no	
Dilepton (C-P)	C: $\|\eta\| < 1.0$ P: $1.1 < \|\eta\| < 3.6$	$E_T^e(p_T^\mu) \geq 8(4)$ GeV(/c) $E_T^e \geq 8$ GeV	yes	no	
Ditau	$\|\eta\| < 1.0$	$E_T^\tau \geq 6$ GeV/c	yes	no	
Tau+$\not\!\!E_T$	$\|\eta\| < 1.0$	$E_T^\tau \geq 20$ GeV/c $\not\!\!E_T \geq 20$ GeV	no	no	
B-exclusive1	$\|\eta\| < 1.0(0.6)$	$E_T^e(p_T^\mu) \geq 4$ GeV(/c)	yes	yes	Sec.Vtx Track Mass
B-exclusive2	$\|\eta_{CMUP}\| < 0.6$, $\|\eta_{CMU(X)}\| < 1.0$	$p_{T\,CMUP} \geq 4$ GeV/c, $p_{T\,CMU(X)} \geq 3$ GeV/c	yes	no	Track Mass
Inclusive e	$\|\eta\| < 1.0$	$E_T \geq 18$ GeV	yes	no	
Inclusive μ	$\|\eta\| < 1.0$	$p_T \geq 18$ GeV/c	yes	no	
$\not\!\!E_T$+jets1	$\|\eta\| < 1.0$	$E_T \geq 18$ GeV $\not\!\!E_T \geq 15$ GeV	yes	no	
$\not\!\!E_T$+jets2	$\|\eta\| < 1.0$	$\not\!\!E_T \geq 20$ GeV	yes	yes	Two XFT Two SVT
Jet20 (Jet50)	$\|\eta\| < 3.6$	$E_T \geq 20(50)$ GeV	no	no	

4.3.1 SM processes accessible via the lepton plus track trigger

Drell-Yan production

The Drell-Yan (DY) process can be accessed for all lepton pairs produced down to rather low p_T and E_T. It includes all charged dileptons: ee, $\mu\mu$, $\tau\tau$. The interest to study such production goes beyond the study of the DY process as this signature is also typical of theories beyond the SM such as, in particular, Extra-dimension Theories (see below).

Also of interest is a study of $Z \to \tau\tau$ where one of the τ's decays leptonically and the other hadronically. In this respect, this trigger is quite unique to perform this measurement. This signature is crucial in the search for Higgs(es) where the Higgs decays into a pair of τ's (see later) as the $Z \to \tau\tau$ is a primary source of background events. We will describe the detailed

Table 4.9. Cuts for dielectron mass plot. Each parameters are explained in the next chapter.

1st leg	2nd leg
$E_T > 10$ GeV	$E_T > 5$ GeV
$p_T > 8$ GeV/c	$E^{had}/E^{em} < 0.05$
$E^{had}/E^{em} < 0.055 + E \times 0.00045$	$\lvert\eta_{det}\rvert < 1.2$
–1.5 cm $< Q_{trk} \cdot \Delta x <$ 3.0 cm	track found
$\lvert\Delta z\rvert <$ 3.0 cm	opposite sign with 1st leg
${\chi^2}_{strip} < 10$	
$L_{shr} < 0.2$	
CEM, CES and COT fiducial	
conversion removal: $\lvert S_{xy}\rvert < 0.1, \lvert\Delta(\cot\theta)\rvert < 0.03$	

analysis for $Z \to \tau\tau$ in the next chapter. It should be noted that the lepton plus track trigger sample also contains $Z \to \tau\tau \to (\ell\nu\nu)(\ell\nu\nu)$ events. Thus, it will be an enriched data sample.

Figure 4.2 shows Opposite-Sign (OS) dielectron mass distribution after imposing the cuts described in **Table 4.9**. We observe an apparent peak from $Z \to ee$ around 91 GeV/c^2. We also see a very visible Υ(1S) peak. **Figures 4.3** and **4.4** are OS dimuon mass distributions (CMUP-CMUP and CMUP-CMX) after removing cosmic ray events with less than four tracks. Loose track isolation of $(\sum\limits_{\Delta R<0.4} p_T - p_T^\mu)/p_T^\mu < 0.2$ is applied to a first leg of muons. We also have $Z \to \mu\mu$ peaks both in CMUP-CMUP and CMUP-CMX events.

For this physics case, the lepton plus track trigger selection must also be compared to the other τ triggers at CDF Run II, namely the di-τ trigger and the τ plus missing-E_T trigger. These two τ triggers focus on high E_T τ-leptons that decay hadronically. Therefore compared to the di-τ trigger, the lepton plus track trigger can collect $\tau_\ell\tau_\ell$ events as well as $\tau_\ell\tau_h$ events with relatively lower E_T or p_T thresholds.

The other τ trigger, namely the τ plus missing E_T trigger, focuses on the $W \to \tau\nu_\tau$ channel for what concerns the electroweak physics topic. The lepton plus track trigger is not particularly suited to this case.

The study of the $Z \to b\bar{b}$ channel is mandatory prior the search for the $H^0 \to b\bar{b}$. Some of $Z \to b\bar{b}$ events will be in this trigger dataset if the b's decay semileptonically to e, μ or τ-lepton.

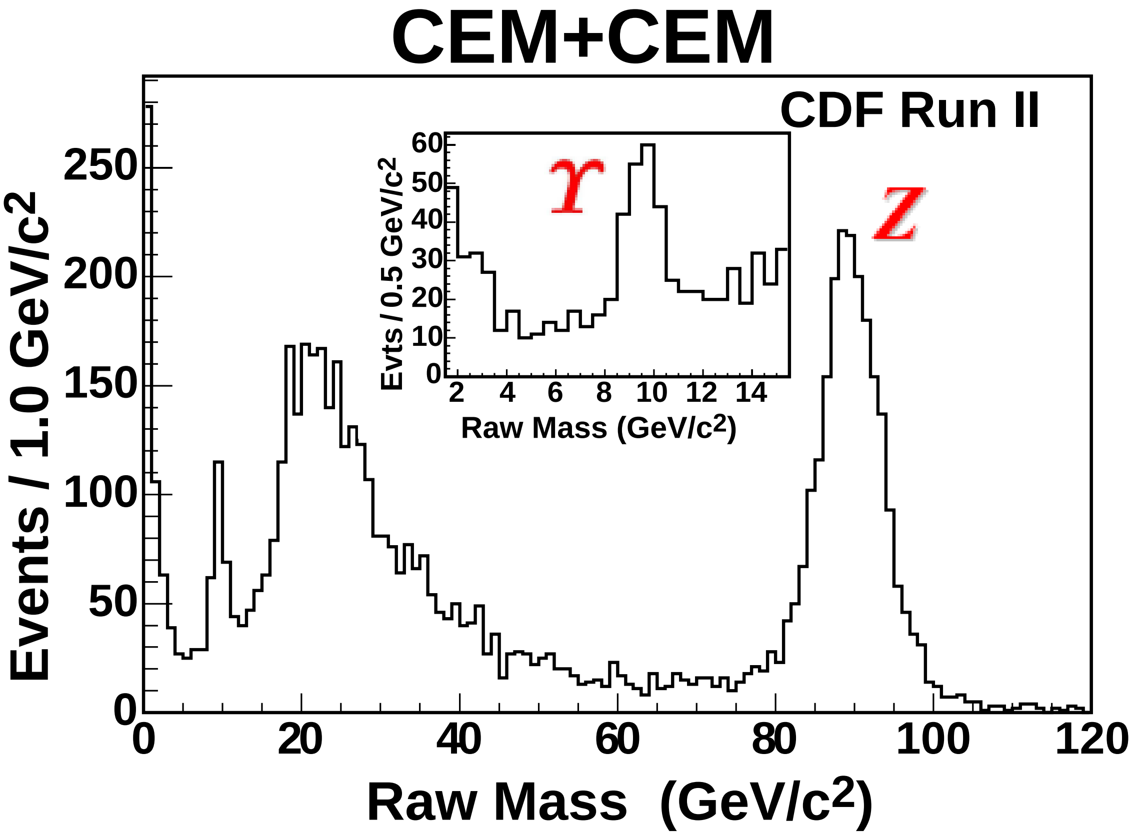

Fig. 4.2. OS dielectron mass distribution in the electron plus track data until January 2003 shutdown. A J/ψ peak is not seen because a separation between two electrons coming from J/ψ decay are not large enough to be identified as two on calorimeter-base electron clustering algorithm.

Top physics

Another important physics issue that can be reached with this trigger is top physics. After the discovery of the top quark in Run I of the Tevatron, Run II will provide the unique opportunity to start top physics both from the point of view of the SM and to study it, as a background, for many expected new phenomena.

The top quark is an essential player in the SM; Being able to measure accurately its mass, its cross-section and its various branching ratios is of fundamental importance. This trigger allows us to study the production of a top pair through its decay products into two charged leptons (including the τ-lepton), thus the various channels, $ee, e\mu, \mu\mu, e\tau, \mu\tau, \tau\tau$, can be examined. The remark on the isolation constraint applies again here: the search for the lepton plus jet signatures with jets other than τ-jets, will be dramatically impeded with the present trigger.

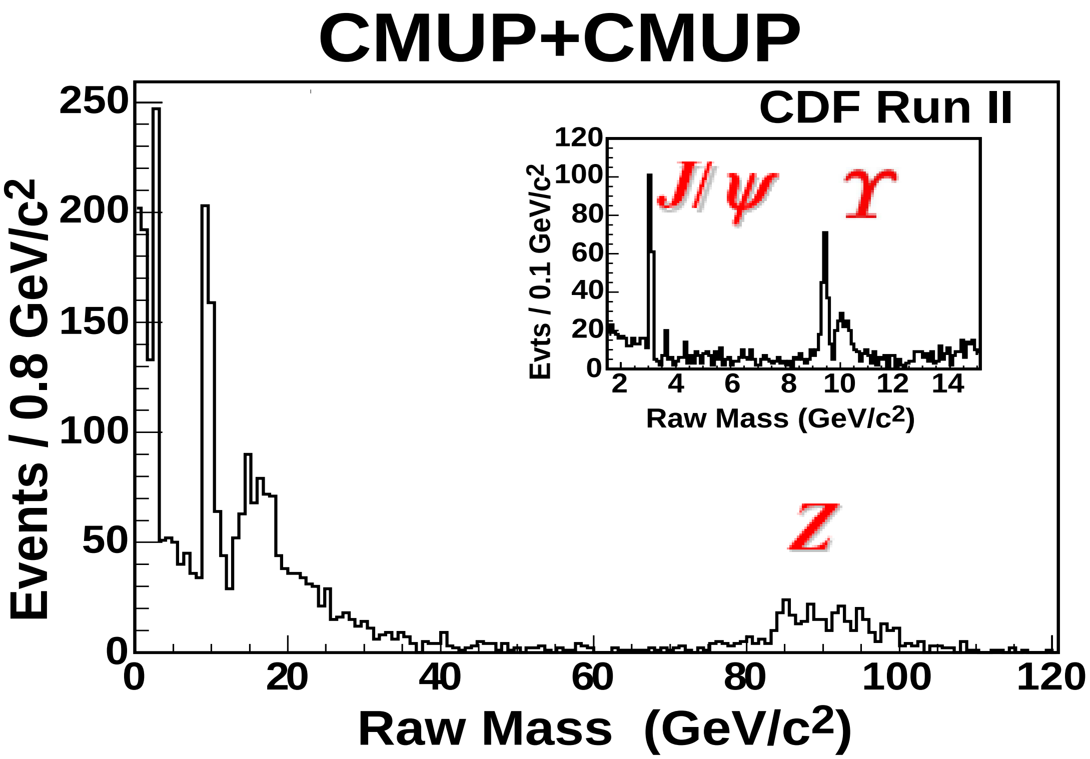

Fig. 4.3. OS dimuon (CMUP-CMUP) mass distribution in the muon plus track data until January 2003 shutdown. Note the beam-constraint fitting is not performed.

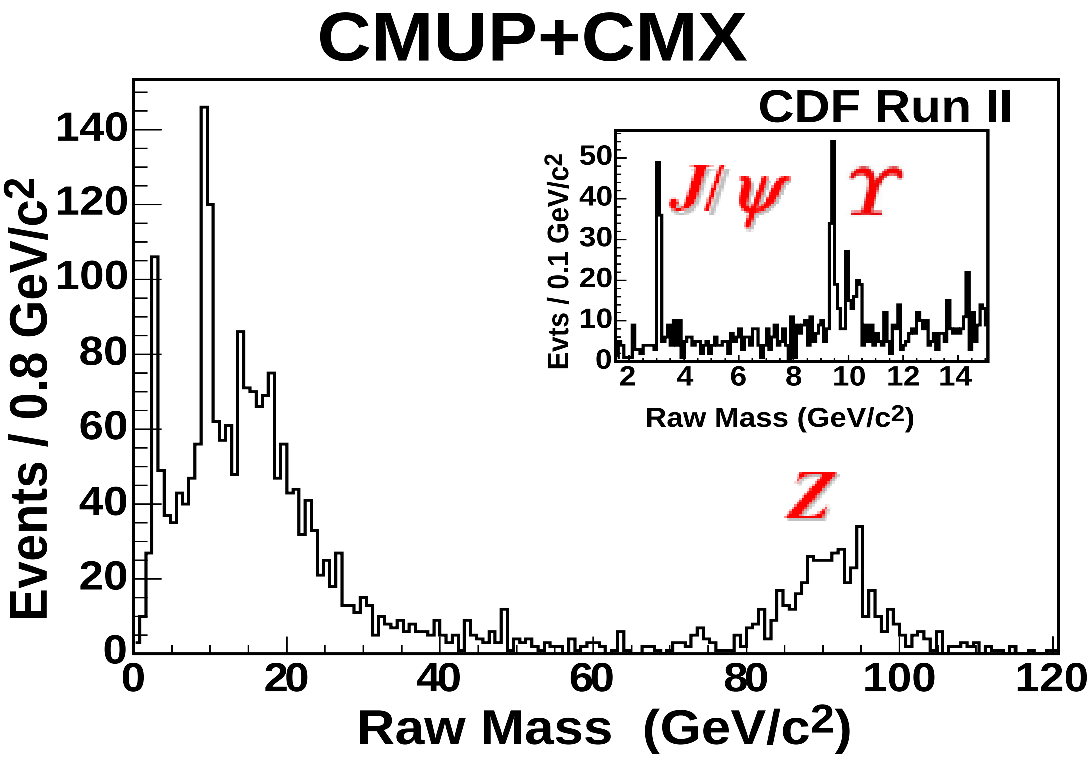

Fig. 4.4. OS dimuon (CMUP-CMX) distribution in the muon plus track data until January 2003 shutdown. Note the beam-constraint fitting is not performed.

This trigger could also contribute to the study of the single top production, especially in the case where the W decay product of the single top decays into a τ-lepton. Furthermore, the same trigger gives the possibility to study the b-fragmentation that impacts on the top measurement.

Comparing with the other triggers that are currently used for the top studies, this trigger gives a unique access to the top searches where top decays leptonically producing one or two τ-leptons.

QCD physics

The scope of applications of this trigger for QCD physics is essentially restricted to the study of $b\bar{b}$ and $c\bar{c}$ productions down to relatively low E_T and p_T values. The identification of these final object relies on the leptonic decays of the heavy flavored quarks only. Indeed the isolation constraint imposed on the second track, prevents the jet from being anything else than a τ-jet. It removes ordinary light quark jets. This has been studied by applying the selection criteria of this trigger to generated light quark jets or b-jets.

It indicates the effect of the isolation cut to remove these b or light quark jets as compared to the τ-jets. Most of the b-jets are removed by this cut even for relatively large p_T values of the b-jets, namely for up to 15 GeV/c in p_T, 70% of the b-jets are removed by a cut of 5 GeV/c on the stiff track.

Getting access to this rather low and intermediate E_T b-jets would be of interest when studying the fragmentation of the b-quark. It would allow us to link the larger E_T region scanned with the jet triggers with the exclusive B-physics triggers that act at very low E_T and p_T. This possible extension of the lepton plus track trigger is discussed in the next section.

By relaxing the condition on the isolation of the track, so as to accept light quark or b-jets, would give an aperture to the lepton plus jets signals that could be of interest also for QCD studies.

B physics

This trigger could also be interesting for addressing certain regions of exclusive final state B-physics. For instance the production of $b\bar{b}$ mesons such as the Υ's in (1S), (2S) or (3S) states can be selected by this trigger through their leptonic decays into ee and $\mu\mu$ (or $\tau\tau$?) channels. Each of these channels has a corresponding branching ratio of 1% to 2%. We might have an opportunity to look for the τ-decay channel of this $b\bar{b}$ meson.

Looking for J/ψ 's or other B or D mesons final states would be only possible in their leptonic decay modes and furthermore the E_T and p_T thresholds may be too high. A possibility for overcoming this problem is discussed in the next section. It also needs more dedicated and detailed study.

The lepton plus track trigger has a much more restricted access to the B-physics than the dedicated exclusive B-triggers. However it might be useful for some particular cases such as access to the τ-decay channels, intermediate E_T-range for the b-fragmentation studies and access to the $b\bar{b}$ mesons, but this needs to be investigated.

W and Z pairs and H production

For the W or Z pair production, this trigger selects the signatures where both W or at least one of the Z decays leptonically, including τ's. It gives a possibility to select signatures of WH production with Higgs H decaying into $b\bar{b}$ or $\tau^+\tau^-$, and a W through its leptonic decay including τ's; the other part of the trigger signature can be used for the Higgs identification. It also serves to identify ZH where the Z decays leptonically and H decays into a $b\bar{b}$ or a $\tau^+\tau^-$. Or one can look for ZH production with any decay for the Z and using the lepton plus track signature to identify the Higgs. The b's can be identified through their semi-leptonic decays and the τ's if both decay leptonically, or if one decays hadronically and the other one leptonically.

The advantage of this trigger is that it goes down to rather low E_T and p_T thresholds even for processes where the decay products have rather high E_T, it thus provides a useful overlap region between the corresponding standard process backgrounds and the signal to be looked for. It furthermore permits to study, with lower E_T and p_T samples, some systematic effects, such as fake leptons based on the same trigger selection.

4.3.2 Beyond the SM processes accessible via the lepton plus track trigger

The dilepton signature is quite a fundamental signature for many beyond-the-SM processes. It is also the basis signature for multilepton signatures that include at least three charged leptons. Here below are briefly described the main physics topics to which these triggers apply. For what concerns the SUSY scenarios that are mentioned here below, it should be noticed that the τ-enriched signatures are expected to become dominant as tanβ increases. This was one of the motivations when this trigger was studied at the FNAL SUSY-Higgs Workshop.

Search for chargino-neutralino associated production

LEP 200 performed an impressive and rather unique work in searching for the neutralino $\tilde{\chi}_1^0$ as the LSP in the MSSM framework. The Tevatron Run I was not able to compete because of the lack of luminosity. One of the main challenges is to overcome the LEP limits on gauginos. The CDF at Run I [49] demonstrated that with a powerful tracking system, the measurement of multilepton signatures with 2 or 3 well measured leptons is an essential tool to search for chargino-neutralino production. Importantly, this trigger thus allows to select these events including the τ's. Because it is able to select all three types of charged leptons, its trigger rates will be higher. However its trigger selection is complementary to the other dilepton $(ee, e\mu, \mu\mu)$ trigger [50]. This other dilepton trigger only selects electrons and muons with a more stringent isolation criteria for both leptons. In the lepton plus track trigger case there is no isolation for the lepton (e or μ) leg, while the track leg has a rather relaxed isolation to select hadronic τ-jets. Besides, it is important to have at least two different triggers to study such types of possible new events or very crucial signatures.

Search for various gluino and squark cascade decays

Higher luminosity in Run II and the improved detector capabilities will allow the search for cascade decays of the gluino or the squarks that was not possible in Run I.

Among the interesting possibilities, there is the case where the gluino decays into a b-quark and sbottom ($\tilde{b}$), followed by $\tilde{b} \to b\tilde{\chi}_2^0$ ($\tilde{\chi}_2^0 \to \tau\tilde{\tau}$ and $\tilde{\tau} \to \tau\tilde{\chi}_1^0$). This τ-enriched signature will become more dominant as tanβ becomes larger. The final decay product of the gluino will be: $bb\tau\tau\tilde{\chi}_1^0$. The τ's produced in this case will be especially selected by this trigger, because its relatively low E_T and p_T thresholds.

Search for third generation squarks and R_p violation

In the MSSM framework with no R-parity violation, the search for stop or sbottom is mainly done through b- and c-taggings. However, some specific scenarios given by R-parity violation make the case for using this trigger.

As studied in Run I and LEP 200, various R-parity violated SUSY scenarios lead to enriched multilepton signatures. For all these cases, this trigger will be quite useful. In addition the fake leptons that are crucial for these searches can be studied with the same triggered sample of data, and thus reduce systematics effects.

Search for non-SM top quark decays

One of the major issues of the Tevatron will be to understand the real nature of top quark production and decay. Top quark production, be it $t\bar{t}$ or single top, is an ideal place where to look for new physics. If there is any new physics associated with the generation of mass, it may be more apparent in the top quark sector than in any of the other lighter, known, fermions. Many models predict new particles or interactions that couple preferentially to the third generation and in particular to the top quark. These models extend the strong, hypercharge or weak interactions in such a way that, at some scale, the new groups spontaneously break into their SM subgroup: $SU(3)_h \times SU(3)_l \to SU(3)_C$, $SU(2)_h \times SU(2)_l \to SU(2)_W$, and

$U(1)_h \times U(1)_l \to U(1)_Y$, where h represents the third (heavy) generation and l the first two (light) generations. As a result, one would expect production rate and kinematic distributions of the decay products to differ from the SM predictions. The SM predicts $\mathcal{B}R(t \to bW) > 0.998$. Other decays allowed in the SM are not only rare, but also mostly too difficult to disentangle from backgrounds to be observed in the future. Nevertheless, one must try to be sensitive to all conceivable signatures of top quark decay, as some can be enhanced by several orders of magnitude in scenarios beyond the SM. Here we highlight some scenarios, with interesting theoretical motivations, in the rich of Tevatron Run II, that will get a relevant advantage of the lepton plus track trigger.

Search for SUSY decays of top

With the observation in 1995 of a heavy top quark [51, 52], an important prerequisite was met for low energy supersymmetry [53] to explain electroweak symmetry breaking. The lightest stop squark ($\tilde{t}_1$) could be lighter than the superpartners of all other squarks because of the large Yukawa coupling of the top quark (See Chapter 2). If the stop squark is light, decays of the top quark into stop plus the lightest neutralino could be kinematically allowed.

The CDF experiment has already searched, during the Run I, for events of this type where the SM top decay proceeds as $t \to bW \to b\ell\nu_\ell$ ($\ell = e, \mu$), while the SUSY decay of the other top proceeds as $t \to \tilde{t}_1\, \tilde{\chi}_1^0 \to b\, \tilde{\chi}_1^+\, \tilde{\chi}_1^0 \to b\, q_1\, \bar{q}_2\, \tilde{\chi}_1^0\, \tilde{\chi}_1^0$, setting a 95% C.L. limit on $\mathcal{B}R(t \to \tilde{t}_1\tilde{\chi}_1^0)$ as function of $m_{\tilde{t}_1}$, $m_{\tilde{\chi}_1^\pm}$ and $m_{\tilde{\chi}_1^0}$ [54]. The letpon plus track trigger will allow us to access also the dilepton final states making possible to increase the sensitivity on $\mathcal{B}R(t \to \tilde{t}_1\tilde{\chi}_1^0)$.

Top decays in BRPV

Another class of models that will be investigated by using the lepton plus track trigger are those based on the bilinear R_p violation (BRPV) [55-58]. These models are well-motivated theoretically as they arise as effective truncations of models where R_p is broken spontaneously [59] through a nonvanishing VEV of the right-handed sneutrino $\tilde{\nu}^c = v_R \neq 0$. In the BRPV models the charginos mix with the charged leptons, the neutralinos with neutrinos, and the charged sleptons with the charged Higgs boson [55, 56, 57]. Therefore, the top can have additional decay modes:

$$t \rightarrow \tilde{\tau}_1^+ \, b \, , \quad t \rightarrow \nu_\tau \, \tilde{t}_1 \, , \quad t \rightarrow \tau^+ \, \tilde{b}_1 .$$

In each case the various decay modes lead to cascade decays:

$$\begin{array}{lll}
t \rightarrow \tilde{\tau}_1^+ \, b & \rightarrow \tau^+ \, \nu_\tau \, b & \\
& \rightarrow \tau^+ \, \tilde{\chi}_1^0 \, b & \rightarrow \tau^+ \, f \, \bar{f} \, \nu_\tau \, b \\
& & \rightarrow \tau^+ \, f \, \bar{f}' \, \tau^\pm \, b \\
t \rightarrow \nu_\tau \, \tilde{t}_1 & \rightarrow \nu_\tau \, \tilde{\chi}_1^+ \, b & \rightarrow \nu_\tau \, f \, \bar{f}' \, \nu_\tau \, b \\
& & \rightarrow \nu_\tau \, f \, \bar{f} \, \tau^+ \, b \\
t \rightarrow \tau^+ \, \tilde{b}_1 & \rightarrow \tau^+ \, \nu_\tau \, b & \\
& \rightarrow \tau^+ \, \tilde{\chi}_1^0 \, b & \rightarrow \tau^+ \, f \, \bar{f} \, \nu_\tau \, b \\
& & \rightarrow \tau^+ \, f \, \bar{f}' \, \tau^\pm \, b
\end{array}$$

In nearly all cases there are two τ's and two b-quarks in the final state plus the possibility of additional leptons and/or jets. Therefore, b-tagging and a good τ identification are important for extracting these final states. The background will come mainly from the production of one or two gauge bosons plus additional jets.

The CDF II detector and the related tau triggers should be sensitive to branching ratio values up to $10^{-3} \sim 10^{-2}$ depending on the mode.

Search for SUSY Higgs

The search for the lighest SUSY Higgs (h_0) will be very similar to the case of the SM Higgs search already mentioned. The difference can be in an enhanced rate in particular for the case where the Higgs decays into a τ-pair. This trigger is quite unique for detecting $h^0 \rightarrow \tau^+\tau^-$ with one leptonic τ and one hadronic τ or both leptonic τ's.

The $b\bar{b}$ channel will be accessible if both b's decay semileptonically, thus with 8% branching ratio for each lepton case.

Search for lepton flavor violating (LFV) Higgs decay

The conservation of the family lepton number ($L_i = L_e,\ L_\mu,\ L_\tau$) follows directly from the fermion quantum number assignment assumed in the SM. There are many SM extensions in

Table 4.10. $\mathcal{BR}$ of LFV Higgs decays for the THDM-III.

M_H [GeV]	$\mathcal{BR}(H \to \mu\tau)$	$\mathcal{BR}(H \to e\tau)$	$\mathcal{BR}(H \to \mu\tau)$	$\mathcal{BR}(H \to e\tau)$
	$\sin\alpha = 0.1$	$\sin\alpha = 0.1$	$\sin\alpha = 0.9$	$\sin\alpha = 0.9$
100	0.7	1.3×10^{-5}	0.1	2.0×10^{-6}
130	0.7	1.2×10^{-5}	0.7	2.1×10^{-6}
170	0.3	5.5×10^{-6}	1.2×10^{-3}	2.3×10^{-8}
200	0.1	2.2×10^{-6}	3.5×10^{-4}	6.4×10^{-9}

which the lepton number can be violated, for instance by just providing neutrinos with a mass, either through dimension-5 operators or Higgs triplets. Strong evidence, in favor of neutrino masses and mixing obtained in Super-Kamiokande and other neutrino experiments, opened a new epoch. Several extensions of the SM, supersymmetric and not, assume the existence of flavor-changing couplings of a Higgs boson. Among them, the generic Two Higgs Doublet Model (THDM-III) can be taken as a representative case where $\mathcal{B}R(H \to \tau\mu)$ can reach values of order $\simeq 10^{-1} \sim 10^{-2}$ as shown in **Table 4.10** [60].

The search for Lepton Flavor Violating (LFV) Higgs decay, $H \to \tau\mu$, is not only well motivated by the favorable interpretation of the ν_μ-ν_τ oscillation but also has at the same time the unique advantage to be a reachable Higgs discovery channel and a way to constrain the present loose bounds on the size of the LFV factor $\kappa_{\tau\mu}$ by following a totally model independent search for LFV Higgs decays [61].

Search for large extra dimensions

The hierarchy between the 4-dimensional Planck Scale $G_{\mathcal{P}}^{-1/2} \sim 10^{19}$ GeV and the electroweak scale $G_{\mathcal{F}}^{-1/2} \sim 10^{2}$ GeV is a fact of Nature. This fact is generally considered, by theorists, a problem. If in SUSY and technicolor, the effort to explain the ratio $G_{\mathcal{P}}/G_{\mathcal{F}}$ is mainly focused on the denominator, numerous scenarios have emerged in the past few years that address the hierarchy problem by focusing on the numerator: the Newton constant ($G_{\mathcal{N}}$). Arkani-Hamed, Dimopoulos and Dvali (ADD) have suggested that the foundamental quantum gravity scale is of the order of the Fermi scale: $G_{\mathcal{N}} = G_{\mathcal{D}}/R^N$ where $G_{\mathcal{D}}$ is the microscopic

Newton constant, N is the number of extra spatial dimensions, hiden, as compactified at each point of the 4-dimensional space, with a compactification radius R [62]. Present gravity experiments, with Cavendish-type setups, cannot test gravity below the millimeter scale. The CDF by using the lepton plus track trigger can study gravity below this edge. As a matter of fact the virtual exchange of graviton towers (G_{KK}) either leads to modifications in the SM cross sections and asymmetries or to new processes not allowed in the SM at the tree level. In the case of virtual G_{KK} emission, gravitons lead to apparent violation of 4-momentum as well as of the angular momentum. The impact of virtual gravitons then can be observed in processes such as: $q\bar{q} \to G \to \gamma\gamma$ or $gg \to G \to \ell^+\ell^-$ where the ADD model introduces production mechanism that can increase the cross-section [63]:

$$\frac{d^2\sigma_{Tot}}{d\cos\theta^*\ dM} = \frac{d^2\sigma_{SM}}{d\cos\theta^*\ dM} + \frac{a(n)}{M_{\mathcal{F}}^4} F_1(\cos\theta^*, M) + \frac{b(n)}{M_{\mathcal{F}}^8} F_2(\cos\theta^*, M) \tag{4.1}$$

where $\cos\theta^*$ is the scattering angle of the photon or lepton in the center of mass frame of the incoming parton. The first term in the Eq.(4.1) is the pure SM contribution; the second and the third parts are the interference term and the direct G_{KK} contribution. The characteristic signatures of virtual graviton exchange correspond then to the formation of massive systems abnormally beyond the SM expectations. The lepton plus track trigger gives a very relevant access to this physics as it permits to study pairs of charged leptons including τ's.

4.4 Possible extensions of the lepton plus track trigger

The present limitations of the trigger as currently running have been briefly mentioned in the previous section. Among those are essentially two:

⇒ The L3 requirement on isolation of the track is appropriate for τ-jet but kills other potential interesting sources of physics such as lepton plus jet(s) where the jet can be either coming from a light quark or else a heavy flavor b or c quark.

⇒ The coverage of XFT reduces the acceptance of this trigger mainly to the central region. As well known when getting higher in energy, physics becomes less and less central.

It is proposed here to have some variations of this trigger. This means adding a few other trigger to enhance the capabilities of selection for a variety of fundamental physics topics.

4.4.1 Extending to lepton plus jet triggers

While keeping the lepton selection as it is, the isolation criteria could be replaced by the following condition

1. Instead of just one, require 2 XFT tracks, the second one having a minimum distance in ΔR with the first XFT track such to allow at least two pencil-like jets. This was studied in Ref. [46], in order to try to keep or increase the threshold on the E_T of the lepton leg and on the contrary to try to decrease the threshold in p_T of the stiff track. The idea here would be both to get rid of the isolation on the stiff track and to possibly lower its p_T threshold.

2. Require one XFT track plus amount of missing transverse energy. Most of the scenarios mentioned in the last section have a certain missing transverse energy. The threshold requirement on the p_T of the XFT track and on the amount of missing energy should be a compromise between a large interesting scope of physics and a reasonable trigger rate.

3. Require an SVT track with the second XFT track, and impose an impact parameter cut to enhance the heavy flavor content in jets.

4.4.2 Extending the geometrical coverage of our trigger

For the time being the plug electrons and the IMU muons can be added.

Enlarging the coverage of the trigger means, at least for the lepton part, to relax the requirement on the XFT matching track. Indeed one can require a matching track with only

3 instead of 4 layers, and the same matching requirement for the case of the forward muons. Maybe it will mean to impose higher E_T thresholds both on electrons and muons.

To conclude this section, there are various ways to expand the physics scope of the lepton plus track trigger in particular in the direction of b-physics or QCD. It implies to relax the condition that ensure tau isolation for the pencil-like jet built from the XFT leg of this trigger. Also it is possible to extend it in the larger η range. This can be done partially by relaxing the requirement on the minimum number of COT layers to build the XFT track or more drastically with hardware upgrades.

These various alternatives would give a few additional triggers to implement in addition to the current lepton plus track trigger.

Chapter 5

Validation of the Lepton plus Track Trigger

5.1 Introduction

In this chapter we report the first look at $Z \rightarrow \tau\tau$ events in an inclusive electron plus track trigger (TAU_ELE) dataset collected from March 2002 to January 2003.

We use the datasets, labeled as ETAU08 and ETLP08, processed using CDF software version 4.8.4. The data are required to pass trigger requirements and a loose fractional track isolation less than 0.2 for electron. Later, the ETAU08 data is reprocessed using version 4.9.1hpt1 plus improved π^0 reconstruction (see Ref. [64] for details). We also require that runs are to be good. The data sample contains 202178 events with $\int \mathcal{L}\, dt = 72$ pb^{-1}.

A sample of the $Z \rightarrow \tau\tau$ events is a good benchmark to calibrate the trigger system and τ identification (ID).

Table 5.1. Electron identification quality cuts.

Electron Variables	Cuts
E_T	> 10 GeV
p_T	> 8 GeV/c
E^{had}/E^{em}	$< 0.055 + 0.00045 \times E$
E/p	< 4.0 (for $E_T > 50$ GeV)
L_{shr}	< 0.2
$\|\Delta x\|$	$-3.0 < Q_{trk} \cdot \Delta x < 1.5$ cm
$\|\Delta z\|$	< 3 cm
χ^2_{strip}	< 10
$\|z_0\|$	< 60 cm
I^{cal} (with leakage correction)	< 3 GeV
(I^{trk}/E_T during stripping)	(< 0.2)
Track quality	
Fiducial Region	

5.2 Events Selection

5.2.1 Baseline Selection

Central Electron Selection

Our analysis begins by requiring at least one good electron in the central region with $E_T \geq 10$ GeV and $p_T \geq 8$ GeV/c. The electron ID criteria are summarized in **Table 5.1**. They are very close to the standard quality cuts for inclusive high E_T central electron used in the CDF [65].

The variables used in the electron ID criteria are explained below;

E^{had}/E^{em} :

The ratio of the CHA energy in the calorimeter cluster (E^{had}) to the CEM energy (E^{em}) is used for rejection of the contamination of hadronic jets.

E/p :

The ratio of the CEM energy of a cluster to the momentum of a given track.

L_{shr} :

The lateral sharing of a central electron allows a comparison of the lateral sharing of energy in the calorimeter towers of an electron cluster to electron shower shapes gained in test beam data. The L_{shr} is defined as

$$L_{shr} = 0.14 \cdot \frac{\sum_i (E_i^{adj} - E_i^{exp})}{\sqrt{(0.14\sqrt{E_{em}})^2 + \sum_i (\Delta E_i^{exp})^2}},$$

where E_i^{adj} is the measured energy in a tower adjacent to the seed tower, E_i^{exp} is the expected energy in the adjacent tower. E_{em} is the total electromagnetic energy of the cluster, the $(0.14\sqrt{E_{em}})$ term is from calorimeter energy resolution. The $(\Delta E_i^{exp})^2$ term is the uncertainty in the expected energy. We expect the large difference when comparing an electron and a jet.

d_0 :

Signed impact parameter with respect to beam line.

z_0 :

The location in z of the intersection between a track and the beam axis.

Δx and Δz :

The distance in the r-ϕ (Δx) and r-z (Δz) planes between the CES cluster position and that of the COT track extrapolated the CES.

χ^2_{strip} :

The χ^2 of a comparison between the CES strip shower profile of a given shower and expected one based on the test beam results.

I^{cal} and I^{trk} :

The calorimeter isolation (I^{cal}) is defined as

$$I^{cal} = \sum_{\Delta R < 0.4} E_T^{cal,i} - E_T^e$$

where E_T^{cal} represents the energy deposit on the i-th calorimeter tower in the cone of $\Delta R = \sqrt{(\Delta\eta)^2 + (\Delta\phi)^2} = 0.4$ around the center of the electromagnetic cluster. Similarly

Table 5.2. Tau Cuts.

Tau Variables	Cuts
$\|\eta_{det}\|$	< 1.0
E_T^{clu}	> 20 GeV
Seed Tower E_T	> 6 GeV
Seed Track p_T	> 6 GeV/c
Mass(tracks+$\pi^0 s$)	< 1.8 GeV/c^2
I^{cal}/E_T^{clu}	< 0.1
$\|z_0(\tau) - z_0(e)\|$	< 5 cm
ξ	> 0.1
$N_{trk}^{iso\ cone}$	$= 0$
$N_{\pi^0}^{iso\ cone}$	$= 0$
Track quality	
Fiducial Region	

Table 5.3. Cone definition.

Run I	Signal Cone :	$0.00 < \theta < 0.17$	
	Isolation Cone :	$0.17 < \theta < 0.52$	
Run II	Signal Cone :	$0.00 < \theta < \alpha$	
	Isolation Cone :	$\alpha < \theta < 0.52$	
	α :	0.005	(for $5.0/E^{clu} < 0.005$)
		$5.0/E^{clu}$	(for $0.005 < 5.0/E^{clu} < 0.17$)
		0.17	(for $5.0/E^{clu} > 0.17$)

the track isolation is defined as

$$I^{trk} = \sum_{\Delta R < 0.4} p_T^{trk,i} - p_T^e$$

where $p_T^{trk,i}$ is the i-th track in the cone with respect to the electron track.

Central τ_h Selection

We require the event to have at least one τ_h object in the central region ($|\eta_{det}| < 1.0$) with cluster transverse energy $E_T^{clu}(\tau_h) > 20$ GeV. The reconstruction of a τ_h object is described in Ref. [66]. The same τ_h ID criteria are used in the $W \to \tau\nu$ analysis at CDF II [67]. **Table 5.2** is a summary of the τ_h ID cuts. It should be noted that there is the difference between the Run I study and this study in the definition of τ_h signal and isolation cones as in **Table 5.3**.

The variables used for τ_h (including those for Chapter 7) are listed below;

z_0 :

The location in z of the intersection between a seed track and the beam axis.

Mass :

The invariant mass of tracks or tracks and neutral pions in τ cone.

ξ :

To discriminate hadronic taus from electrons, we define the variable related to EM fraction and E/P as,

$$\xi \equiv \frac{E_T}{\Sigma|p_T|}(1.0 - \frac{E^{em}}{E}) = \frac{E_T^{had}}{\Sigma|p_T|}.$$

N_{trk} and N_{π^0} :

Number of tracks with $p_T > 1.0$ GeV/c in τ cone or isolation cone[1]. Number of π^0s with $E_T > 0.5$ GeV in τ cone or isolation cone.

I_{trk} and I_{π^0} :

The first kind of isolation we use is track isolation and this variable is defined as a scalar sum of all tracks inside a cone of $10^\circ - 30^\circ$ around the seed track in 3D space:

$$I_{trk}^{\Delta\Theta} = \sum_{10^\circ < \Delta\Theta < 30^\circ}$$

Note that for a track to be counted in the isolation, it is required that the track has z_0 compatible with that of the seed track: $|z_0^{trk} - z_0^{seed}| < 5.0$ cm.

We also define isolation in η - ϕ space and use it primarily to match the requirements used in the trigger.

$$I_{trk}^{\Delta R} = \sum_{0.17 < \Delta R < 0.52} p_T$$

In a similar way, we define the tau candidate π^0 isolation, $I_{\pi^0}^{\Delta R}$ and $I_{\pi^0}^{\Delta R}$.

---

[1] For isolation cut fixed cone is used, namely $10^\circ - 30^\circ$

Table 5.4. Requirements for a pair of tracks to be tagged as a conversion.

$\lvert\Delta(\cot\theta)\rvert \geq 0.04$
$\Delta S_{xy} \geq 0.2$

Table 5.5. Cuts for calorimeter- and track-based $Z \to ee$ removal.

	Cuts
Calorimeter-base	$E_T > 8$ GeV $E^{had}/E^{em} < 0.12$ Opposite Sign $75 < M(e, CdfEmObj) < 105$ GeV/c^2
Track-base	$p_T^{trk} > 10$ GeV/c $Iso^{trk} < 0.05$ $\lvert z_0^{trk} - z_0^{ele}\rvert < 8$ cm Opposite Sign $60 < M(e, trk) < 110$ GeV/c^2

5.2.2 Conversion Electron Removal

We remove events in which primary electron candidate is likely produced by a photon conversion. Definition of a conversion candidate is given in **Table 5.4**. S_{xy} is defined as the distance between the two track trajectory helices at the point of their closest approach to each other.

5.2.3 $Z \to ee$ Removal

Since the second-leg electron from the $Z \to ee$ decay can be misidentified as one-prong τ_h,[2] we strictly remove the $Z \to ee$ events by using (i) calorimeter information and (ii) track information. The cuts are taken from the similar analysis in Run I [68] and summarized in **Table 5.5**.

---

[2] Tau ID cuts include an explicit cut against electrons, but it is found that a fraction of $Z \to ee$ events still passes all cuts. This motivate us to use an explicit removal of $Z \to ee$ events to further suppress this background.

5.2.4 $M_T(e, \not{E}_T)$ and $p_T(e, \not{E}_T)$ Cuts

The SM backgrounds for $Z \to \tau_e \tau_h$ signal are QCD, W+jets, $Z/\gamma^* \to ee$, $t\bar{t}$ and diboson production. Of them QCD and W+jets events are dominant. First, we remove W+jets by applying a cut on transverse mass of electron and missing E_T, $M_T(e, \not{E}_T)$. The W events appear in higher mass region. Therefore we require

$$M_T(e, \not{E}_T) \leq 25 \text{ GeV}/c^2$$

After the M_T cut, a significant number of QCD background events still remains in our sample. To remove QCD events we define $p_T(e, \not{E}_T) \equiv |\overrightarrow{E_T}(e) + \overrightarrow{\not{E}_T}|$ and require

$$p_T(e, \not{E}_T) \geq 25 \text{ GeV}/c.$$

A total of 78 events are left after the $p_T(e, \not{E}_T)$ cut.

5.3 Results

The two plots we are interested in are inclusive multiplicity of tracks in the tau signal cone and also invariant mass of the electron-τ_h-$\not{E}_T$ system for OS events.

5.3.1 Track Multiplicity

After applying baseline e/τ_h ID cuts and $M_T(e, \not{E}_T)/p_T(e, \not{E}_T)$ cuts for background reduction, the data is expected to consist of $Z \to \tau_e \tau_h$ signal events and backgrounds dominated by QCD jet production and to less extent by $Z/\gamma^* \to ee$.

We use PYTHIA 6.1 Monte Carlo (MC) with full detector simulation to generate $Z/\gamma^* \to ee$ backgrounds. We estimate the expected number of $Z/\gamma^* \to ee$ events surviving all cuts to be 3.7 assuming $\sigma \cdot BR(Z \to ee) = 250$ pb.

To estimate the shape of the backgrounds where a jet is misidentified as τ_h, we use results of a dedicated study of tau fake rates [69]. In Ref. [69], a generic jet sample is used to measure how often a jet (or, alternatively, a offline production-level CdfTau) can survive standard tau ID cuts. It should be noted that there is an independent analysis of the fake rate [70]. Results are tabulated as a function of jet (CdfTau) E_T and track multiplicity inside the tau cone. If $\mathcal{P}^{CdfTau}(N_{trk}, E_T)$ is the 2D distribution for all CdfTaus passing ID cuts, and the $I^{CdfTau}(N_{trk}, E_T)$ is the same distribution for all found CdfTaus before applying ID cuts, the distribution of the number of tracks for background events can be predicted as:

$$n^{QCD}(N_{trk}) = \int \frac{\mathcal{P}^{CdfTau}(N_{trk}, E_T)}{I^{CdfTau}(N_{trk}, E_T)} \times Data^{LS}(E_T)\; dE_T,$$

where $Data^{LS}(E_T)$ is the E_T spectrum of the backgrounds surviving all cuts. For this study, we estimate $Data^{LS}(E_T)$ by the E_T distribution of the Like-Sign (LS) data passing all cuts when no tau ID cuts are applied. This approach does not give correct overall normalization but should give a reasonable estimation for the shape of the background distribution. A correct normalization can be obtained by using not just LS, but all data with the signal subtracted.

Next we determine the shape of the $Z \to \tau_e \tau_h$ signal by applying all cuts for MC samples. After applying all cuts, the trigger effect should be considered. Because of slight difference in how track isolation is defined in offline and in the trigger, we explicitly require that MC events pass not only standard offline tau tracking isolation but also satisfy trigger tracking isolation requirement. The trigger efficiencies for L1, L2 and L3 are taken into account [71, 72].

Finally we fit the data distribution with two floating variables for signal and QCD background using Log-Likelihood as follows,

$$N^{tot}_{fit}(N_{trk}) = A \cdot n^{Z\to\tau_e\tau_h(MC)}_{expected}(N_{trk}) + B \cdot n^{QCD}(N_{trk}) + N^{Z/\gamma^*\to ee(MC)}_{expected}(N_{trk})$$

where

- A, B = Free parameters (Normalizations for data and unknown absolute background).
- $n^{Z\to\tau_e\tau_h(MC)}_{expected}$ = Shape of the expected multiplicity of $Z \to \tau_e \tau_h$ MC events.
- $N^{Z/\gamma^*\to ee(MC)}_{expected}$ = Multiplicity distribution of $Z/\gamma^* \to ee$ events in MC.

Table 5.6. Result of the fit of tau track multiplicity. For MC based prediction, we assume that $\sigma \cdot BR(Z \to \ell\ell) = 250$ pb. Note that extracted number of events corresponds to measured $\sigma \cdot BR(Z \to \tau\tau) = 267\pm87$ pb.

		Number of Events
Data :	N_{data}^{tot}	78
Expected :	$N_{expected}^{Z\to\tau_e\tau_h(MC)}$	43
	$N_{expected}^{Z/\gamma^*\to ee(MC)}$	3.7
Fit :	$N_{fit}^{Z\to\tau_e\tau_h(MC)}$	46±15
	N_{fit}^{QCD}	28±14

- n^{QCD} = Expected multiplicity shape of the backgrounds (QCD jets faking tau by passing all tau ID cuts).

$$\Rightarrow N_{fit}^{Z\to\tau_e\tau_h} = A \cdot n_{expected}^{Z\to\tau_e\tau_h(MC)}, \quad N_{fit}^{QCD} = B \cdot n^{QCD}$$

Results are shown in **Table 5.6** and **Fig. 5.1**.

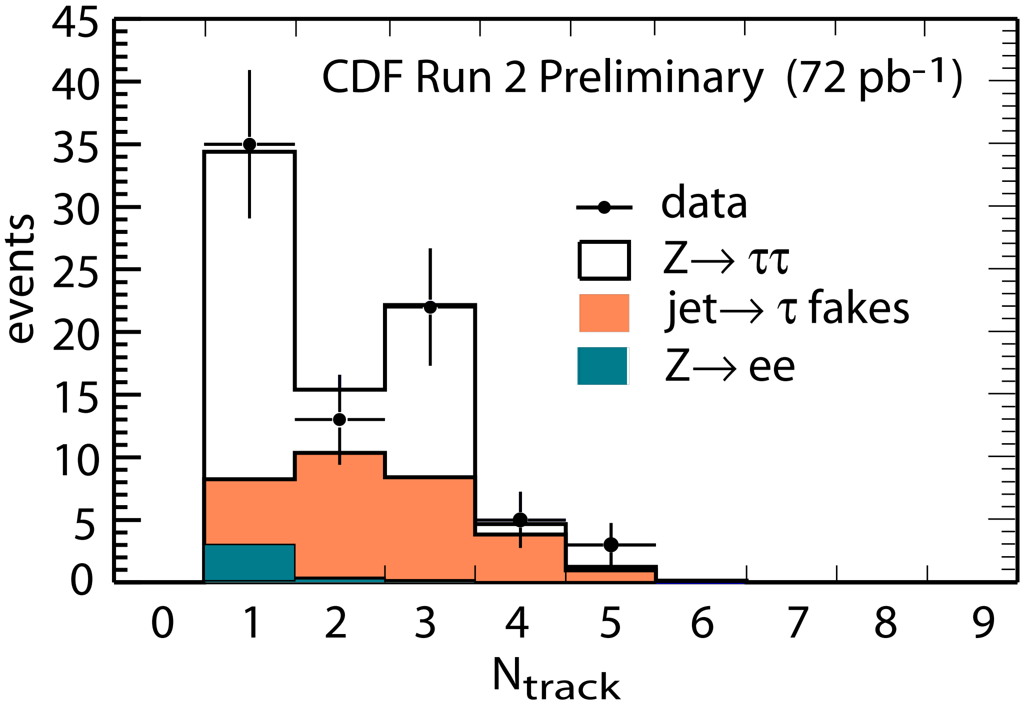

Fig. 5.1. Track multiplicity of τ objects in the electron plus track trigger dataset after baseline, $M_T(e, \not{E}_T)$ and $p_T(e, \not{E}_T)$ cuts. Signal and QCD background are scaled as floating variables.

5.3.2 Mass

Of 78 events, we leave 47 events after requiring that the charge of the τ_h object to have Opposite Sign (OS) of the electron. The τ_h charge is defined as the sum of the track charges. **Figure 5.2** shows the mass of e-τ_h-$\not{E}_T$ system. In the fashion similar to the case in the track multiplicity, we estimate the shape of the QCD backgrounds for the mass distribution, $M_{e\tau_h\not{E}_T}$ by:

$$n^{QCD}(M_{e\tau_h\not{E}_T}) = \sum^{N_{trk}=1,3} \int \frac{\mathcal{P}^{CdfTau}(N_{trk}, E_T)}{I^{CdfTau}(N_{trk}, E_T)} \times Data^{LS}(E_T, M_{e\tau_h\not{E}_T})\, dE_T.$$

Here $Data^{LS}(E_T, M_{e\tau_h\not{E}_T})$ is a distribution of the LS events in the E_T-$M_{e\tau_h\not{E}_T}$ plane.

The final distribution is fitted for normalization of QCD backgrounds (signal normalization is fixed by the multiplicity fit). We also fit data with a 2-parameter fit (signal normalization is not fixed anymore). **Table 5.7** is a summary of the fitting result.

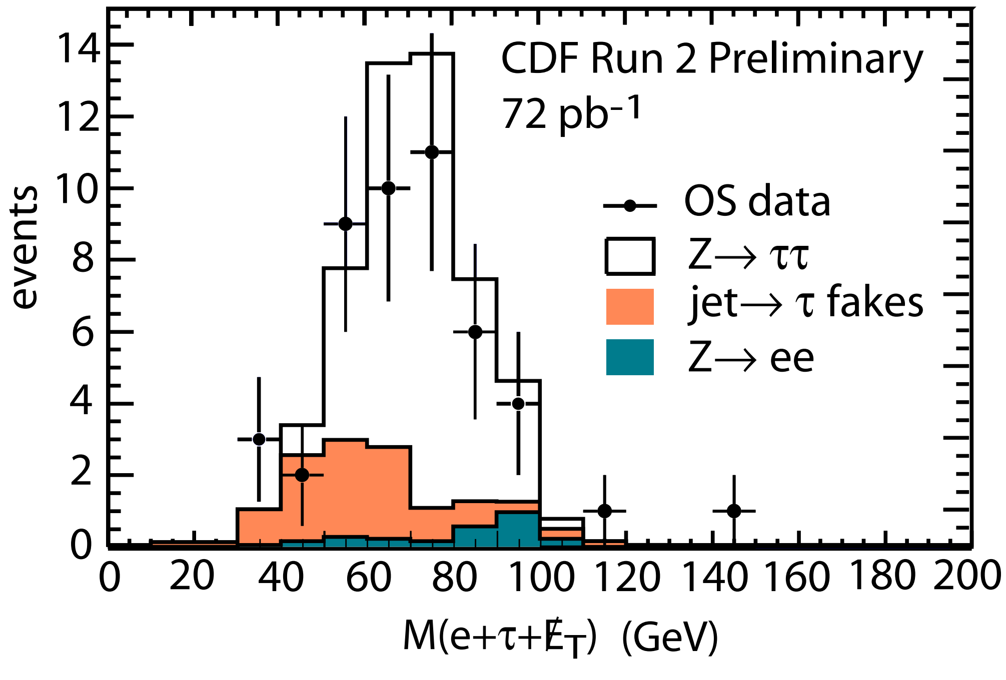

Fig. 5.2. Mass distribution of OS $e\tau_h$ events after baseline, $M_T(e, \not{E}_T)$ and $p_T(e, \not{E}_T)$ cuts. The same normalization factor from the N_{trk} analysis is used for the signal. The distribution of QCD background events is fitted as a floating variable.

Table 5.7. Result of the fit of mass. For MC based prediction, we assume that $\sigma \cdot BR(Z \to \ell\ell)$ = 250 pb.

		Number of Events
Data :	N_{data}^{tot}	47
Expected :	$N_{expected}^{Z\to\tau_e\tau_h(MC)}$	36
	$N_{expected}^{Z/\gamma^*\to ee(MC)}$	2.8
Fit (for QCD) :	$N_{from\ track\ multi.}^{Z\to\tau_e\tau_h(MC)}$	39 (fixed)
	N_{fit}^{QCD}	11±6
Fit (for signal and QCD) :	$N_{fit}^{Z\to\tau_e\tau_h(MC)}$	29±10
	N_{fit}^{QCD}	14±8

5.4 Summary

The Run II data collected by the electron plus track trigger, corresponding to 72 pb^{-1} of integrated luminosity, has been analyzed. In a sample of $e\tau_h$ events we observed a clear tau signal even before an OS sign cut between the electron and the τ_h object is required. The expected number of signal events obtained from the fit of track multiplicity distribution of the τ_h candidates was in agreement with other $Z \to \ell\ell$ analysis [73, 74]. Furthermore the $M_{e\tau_h \not{E}_T}$ distribution in the data was found to be consistent with the ditau events being from $Z \to \tau\tau$.

Chapter 6

Indirect SUSY Search at CDF

New phenomena beyond the SM should appear as a deviation from the SM if such new models exist. Since a deviation may occur through a generation of heavy particles, one of our methodologies for new physics search is to find those traces, for example, a search for scalar top quark described in the next chapter. Another approach is a precise measurement for a parameter, such as branching ratios and etc. When an unknown particle intermediates in a decay of produced particles, branching ratios for rare decays could be larger than predicted in the SM. This is another approach of the searches for beyond the SM, including SUSY. In this chapter we report on a search for $B_s^0 \to \mu^+\mu^-$ and $B_d^0 \to \mu^+\mu^-$ decays in CDF II.

The rare flavor-changing neutral current decay $B_s^0 \to \mu^+\mu^-$[1] is one of the most sensitive probes to physics beyond the SM [75-79]. The decay has not been observed and the branching ratio ($\mathcal{B}R$) is currently limited to $\mathcal{B}R(B_s^0 \to \mu^+\mu^-) < 2.0\times10^{-6}$ at 90% Confidence Level (C.L.) [80], while the SM prediction is $(3.5\pm0.9)\times10^{-9}$ [81]. The limit on the related branching ratio, $\mathcal{B}R(B_s^0 \to \mu^+\mu^-) < 1.6\times10^{-7}$ [82], is approximately 1000 times larger than its SM expectation. The $\mathcal{B}R(B_s^0 \to \mu^+\mu^-)$ can be significantly enhanced in various supersymmetric extensions of the SM. R-parity violating SUSY models can accommodate $\mathcal{B}R(B_s^0 \to \mu^+\mu^-)$ up to 10^{-6} [77]. Minimal supergravity models at large tan β [76-78] also predict $\mathcal{B}R(B_s^0 \to \mu^+\mu^-) < \mathcal{O}(10^{-7})$ in regions of parameter space consistent with the observed muon $g-2$ [83] as well as with

---

[1] Throughout this chapter inclusion of charge-conjugate modes is implicit.

the observed relic density of CDM [84]. SO(10) models [79], which naturally accommodate neutrino masses, predict a branching ratio as large as 10^{-6} in regions of parameter space consistent with these same experimental constraints. Correspondingly, the $\mathcal{BR}(B_d^0 \to \mu^+\mu^-)$ can be enhanced by the same models. Even modest improvements to the experimental limits can significantly restrict the available parameter space of these models. The dataset used in this study corresponds to an integrated luminosity of $\mathcal{L} = 171 \pm 10$ pb^{-1} [85].

The data used in this analysis are selected by dimuon triggers. Muons are reconstructed as track stubs in the CMU chambers. Two well-separated stubs are required and each is matched to a track reconstructed online using COT axial information [86]. The matched tracks must have $p_T > 1.5$ GeV/c. A complete event reconstruction performed online confirms the p_T and track-stub matching requirements.

If the overlapping CMP chambers contain a confirming muon stub, the track is required to have $p_T > 3$ GeV/c. The two tracks must originate from the same vertex, be oppositely charged, and have an opening angle inconsistent with a cosmic ray event. The invariant mass of the muon pair must satisfy $M_{\mu^+\mu^-} < 6$ GeV/c^2. Events in which neither muon is reconstructed with a CMP stub must additionally satisfy $p_T^{\mu^+} + p_T^{\mu^-} > 5$ GeV/c and $M_{\mu^+\mu^-} > 2.7$ GeV/c^2. This set of triggers is used for all the data included here and events passing these requirements are recorded for further analysis.

Our offline analysis begins by identifying the muon candidates and matching them to the trigger tracks using COT hit information. To avoid regions of rapidly changing trigger efficiency, we omit muons with $p_T < 2$ GeV/c. To reduce backgrounds from fake muons, stricter track-stub matching requirements are made and the vector sum of the muon momenta must satisfy $|\vec{p}_T^{\,\mu^+\mu^-}| > 6$ GeV/c. To ensure good vertex resolution, stringent requirements are made on the number of SVX II hits associated with each track. Surviving events have the two muon tracks constrained to a common 3D vertex satisfying vertex quality requirements. The two-dimensional decay length, $|\vec{L}_T|$, is calculated as the transverse distance from the beam line to the dimuon vertex and is signed relative to $\vec{p}_T^{\,\mu^+\mu^-}$. For each B candidate we estimate the proper decay length using $\lambda = cM_{\mu^+\mu^-}|\vec{L}_T|/|\vec{p}_T^{\,\mu^+\mu^-}|$. In the data, 2981 events survive all the above trigger and offline reconstruction requirements. This forms a background-dominated sample with contributions from two principal sources: combinatoric background events with a fake muon and events from generic B-hadron decays (e.g., sequential semileptonic decays $b \to c\mu^- X \to \mu^+\mu^- X$ or double semileptonic decay in gluon splitting events $g \to b\bar{b} \to \mu^+\mu^- X$).

We model the signal decays using PYTHIA program [87] tuned to inclusive B-hadron data [88]. The PYTHIA events are passed through a full detector simulation and satisfy the same requirements as the data. To normalize to experimentally determined cross sections, we require $p_T(B^0_{s(d)}) > 6$ GeV/c and rapidity $|y| < 1$.

To discriminate $B^0_{s(d)} \to \mu^+\mu^-$ decays from background events we use the four variables: the invariant mass of the muon pair ($M_{\mu^+\mu^-}$), the B-candidate proper decay length (λ), the opening angle ($\Delta\Phi$) between the B-hadron flight direction (estimated as the vector $\vec{p}_T^{\,\mu^+\mu^-}$) and the vector $\vec{L}_T$, and the B-candidate track isolation I, where I is defined as

$$I = \frac{|\vec{p}_T^{\,\mu^+\mu^-}|}{\sum_{i,\Delta R<1.0} p_T^i + |\vec{p}_T^{\,\mu^+\mu^-}|}.$$

Figure 6.1 shows the distributions of these variables for background-dominated data and MC signal events.

A "blind" analysis technique is used to determine the optimal selection criteria for these four variables. The data in the search window $5.169 < M_{\mu^+\mu^-} < 5.469$ GeV/c^2 are hidden, and the optimization is performed using only data in the sideband regions, $4.669 < M_{\mu^+\mu^-} < 5.169$ GeV/c^2 and $5.469 < M_{\mu^+\mu^-} < 5.969$ GeV/c^2. The search region corresponds to approximately ± 4 times the two-track invariant mass resolution centered on the B^0_s and B^0_d masses, 5.369 GeV/c^2 and 5.279 GeV/c^2, respectively. We use the set of $(M_{\mu^+\mu^-}, \lambda, \Delta\Phi, I)$ criteria which minimizes the *a priori* expected 90% C.L. upper limit on the branching ratio. For a given number of observed events n and an expected background of n_{bg}, the branching ratio is determined using

$$\mathcal{BR}(B^0_s \to \mu^+\mu^-) \leq \frac{N(n, n_{bg})}{2\sigma_{B^0_s}\mathcal{L}\alpha\varepsilon_{total}},$$

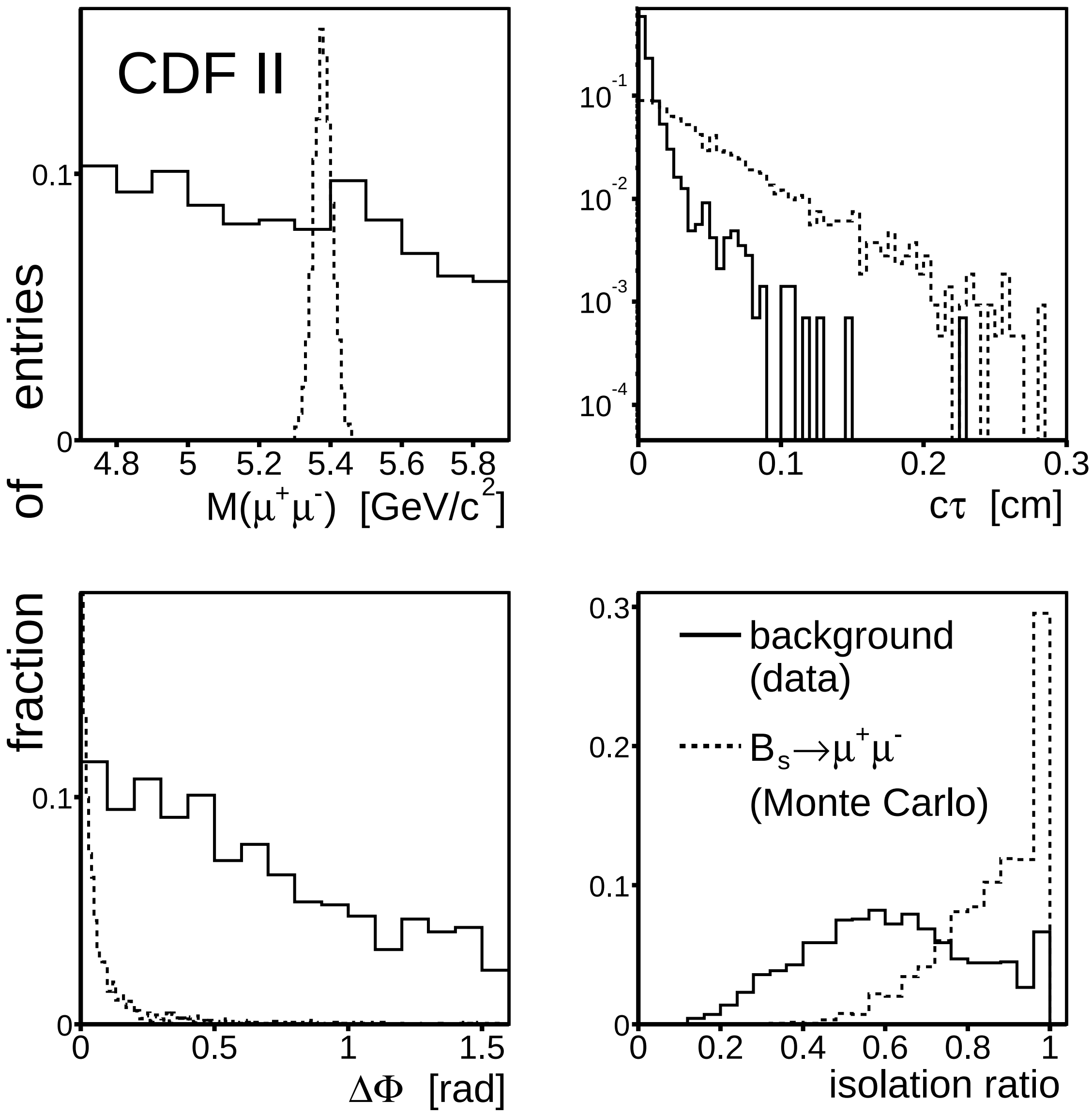

Fig. 6.1. Arbitrarily normalized distributions of the discriminating variables for events in our background-dominated data sample (solid line) compared to Monte Carlo $B_s^0 \to \mu^+\mu-$ events (dashed line).

where $N(n, n_{bg})$ is the number of candidate $B_s^0 \to \mu^+\mu^-$ decays at 90% C.L., estimated using the Bayesian approach of Ref.[89] and incorporating the uncertainties into the limit. The *a priori* expected limit is given by the sum over all possible observations, n, weighted by the corresponding Poisson probability when expecting n_{bg}. The B_s^0 production cross section is estimated as $\sigma_{B_s^0} = \frac{f_s}{f_u} = \frac{0.100}{0.391}$, where $f_{s(u)}$ is the probability that a b quark fragments to produce $B_{s(u)}$ hadron, and σ_{B^+} is taken from Ref.[90]. For the $B_d^0 \to \mu^+\mu^-$ limit we substitute $\sigma_{B_d^0}$ for $\sigma_{B_s^0}$, f_d for f_s, and assume $f_d = f_u$. The factor of 2 in the denominator accounts for the charge-conjugate B-hadron final states. The expected background n_{bg} and the total acceptance times efficiency $\alpha\varepsilon_{total}$ are estimated separately for each combination of requirements.

For both signal and background, the variables λ and $\Delta\Phi$ are the only correlated variables with a linear correlation of -0.3. Thus we estimate the number of background events as $n_{bg} = n_{sb}(\lambda, \Delta\Phi) f_I f_M$, where $n_{sb}(\lambda, \Delta\Phi)$ is the number of sideband events passing a particular set of λ and $\Delta\Phi$ cuts, f_I is the fraction of background events that survive a given I requirement, and f_M is the ratio of the number of events in the search window to the number of events in the sideband regions. Since $M_{\mu^+\mu^-}$ and I are uncorrelated with the rest of the variables, we evaluate f_M and f_I on samples with no λ or $\Delta\Phi$ requirement, thus reducing their associated uncertainty.

We estimate f_I from the background-dominated sample for a variety of thresholds. We investigate sources of systematic bias by calculating f_I in bins of $M_{\mu^+\mu^-}$ and λ and conservatively assign a relative systematic uncertainty of ± 5%. Since the $M_{\mu^+\mu^-}$ distribution of the background-dominated sample is well described by a first-order polynomial, f_M is given by the ratio of widths of the search to sideband regions.

MC studies demonstrate that our estimate of n_{bg} accurately accounts for generic $b\bar{b}$ contributions, while two-body decays of B mesons ($B_{s(d)}^0 \to h^+h^-$, where $h^\pm = \pi^\pm$ or $K^\pm$) are estimated to contribute to the search region at levels at least 100 times smaller than our expected sensitivity.

Using these background-dominated control samples, $\mu^\pm\mu^\pm$ events and $\mu^+\mu^-$ events with

$\lambda < 0$, we compare our background predictions to the number of events in the search window for a wide range of $(\lambda, \Delta\Phi, I)$ requirements. No statistically significant discrepancies are observed. For example, using the optimized set of selection criteria described below and summing over these control samples, we get a total prediction of 3 ± 1 events and observe five. Another cross-check is performed using a fake muon enhanced $\mu^+\mu^-$ sample. By requiring at least one of the muon legs to fail the muon identification requirements, we reduce the signal efficiency by a factor of 50 while increasing the background acceptance by a factor of 3. In this sample, using the optimized requirements, we predict 6 ± 1 and observe seven events.

We estimate the total acceptance times efficiency as $\alpha\varepsilon_{total} = \alpha\varepsilon_{trig}\varepsilon_{reco}\varepsilon_{final}$, where α is the geometric and kinematic acceptance of the trigger, ε_{trig} is the trigger efficiency for events in the acceptance, ε_{reco} is the offline reconstruction efficiency for events passing the trigger, and ε_{final} is the efficiency for passing the final cuts on the discriminating variables for events satisfying the trigger and reconstruction requirements. For the optimization, only ε_{final} changes as we vary the requirements on $M_{\mu^+\mu^-}, \lambda, \Delta\Phi$, and I.

The acceptance is estimated as the fraction of $B^0_{s(d)} \to \mu^+\mu^-$ MC events which fall within the geometric acceptance and satisfy the kinematic requirements of at least one of the analysis triggers. We find $\alpha = (6.6 \pm 0.5)\%$. The uncertainty includes roughly equal contributions from systematic variations of the modeling of the B-hadron p_T spectrum and longitudinal beam profile, and from the statistics of the sample. It also includes negligible contributions from variations of the beam line offsets and of the detector material description used in the simulation.

The trigger efficiency, including the effects of the offline-to-trigger track matching, is estimated from samples of $J/\psi \to \mu^+\mu^-$ decays selected with a trigger requiring only one identified muon. The data are used to parametrize the trigger efficiency as a function of p_T and η for the unbiased muon. The efficiency for $B^0_{s(d)} \to \mu^+\mu^-$ decays is determined by the convolution of this parametrization with the $(p_T^{\mu^+}, \eta^{\mu^+}, p_T^{\mu^-}, \eta^{\mu^-})$ spectra of signal MC events within the acceptance. Including the online reconstruction requirements, the trigger efficiency is $\varepsilon_{trig} = (85 \pm 3)$ %. The uncertainty is dominated by the systematic uncertainty accounting for kinematic differences between $J/\psi \rightarrow \mu^+\mu^-$ and $B^0_{s(d)} \rightarrow \mu^+\mu^-$ decays and also includes contributions from variations in the functional form used in the parametrization, the effects of two-track correlations, and sample statistics.

The offline reconstruction efficiency is given by the product $\varepsilon_{reco} = \varepsilon_{COT}\varepsilon_{\mu}\varepsilon_{SVX}$, where ε_{COT} is the absolute reconstruction efficiency of COT, ε_{μ} is the muon reconstruction efficiency given a COT track, and ε_{SVX} is the fraction of reconstructed muons which satisfy the SVX II requirements. Each term is a two-track efficiency. A hybrid data-MC method is used to determine ε_{COT}. Occupancy effects are accounted for by embedding COT hits from MC tracks in data events. The MC simulation is tuned at the hit level to reproduce residuals, hit width, and hit usage in the data.

For embedded muons with $p_T > 2$ GeV/c, we measure $\varepsilon_{COT} = 99$ %. Using the unbiased $J/\psi \rightarrow \mu^+\mu^-$ samples, we estimate the muon reconstruction efficiency, including the track-stub matching requirements, to be 96%. A sample of $J/\psi \rightarrow \mu^+\mu^-$ events satisfying our COT and muon reconstruction requirements is used to determine $\varepsilon_{SVX} = 75$ %. The total reconstruction efficiency is given by the above product, $\varepsilon_{reco} = (71 \pm 3)$ %. The uncertainty is dominated by the systematic uncertainty accounting for kinematic differences between $J/\psi \rightarrow \mu^+\mu^-$ and $B^0_{s(d)} \rightarrow \mu^+\mu^-$ decays and also includes contributions from the variation of the COT simulation parameters and sample statistics.

The efficiency ε_{final} is determined from the $B^0_{s(d)} \rightarrow \mu^+\mu^-$ MC sample and varies from 28 % - 78 % over the range $(M_{\mu^+\mu^-}, \lambda, \Delta\Phi, I)$ requirements considered in the optimization. The MC modeling is checked by comparing the mass resolution and $\lambda, \Delta\Phi$ and I efficiency as a function of selection threshold for $B^+ \rightarrow J/\psi K^+ (J/\psi \rightarrow \mu^+\mu^-)$ events. The $B^+ \rightarrow J/\psi K^+$ MC sample is produced in the same manner as the $B^0_s \rightarrow \mu^+\mu^-$ sample. The $B^+ \rightarrow J/\psi K^+$ data sample is collected using dimuon triggers very similar to those used in the analysis, but with a larger acceptance for $B^+ \rightarrow J/\psi K^+$ decays. We make the same requirements on the dimuon tracks and vertex as employed in the analysis. The MC efficiency is consistent with the sideband-subtracted data efficiency for a range of cut thresholds within 5% (relative), which is assigined as a systematic uncertainty on ε_{final}. In both the data and the MC sample, the mean of the three-track invariant mass distribution is within 3 MeV/c^2 of the world average B^+ mass. The two-track invariant mass resolution is well described by the MC sample.

The optimal set of selection criteria uses a ± 80 MeV/c^2 search window around the B_s^0 mass, $\lambda > 200\mu$m, $\Delta\Phi < 0.10$ rad, and $I > 0.65$. The mass resolution, estimated from the MC for the events surviving all requirements, is 27 MeV/c^2 so that the B_d^0 and B_s^0 masses are resolved. We define a separate search window centered on the world average B_d^0 mass and use the same set of selection criteria for the $B_d^0 \to \mu^+\mu^-$ search. The total acceptance times efficiency is $\alpha\varepsilon_{total} = (2.0 \pm 0.2)$ % for both decays.

Using these criteria one event survives all requirements and has an invariant mass of $M_{\mu^+\mu^-} = 5.295$ GeV/c^2, thus falling into both the B_s^0 and B_d^0 search windows as shown in **Fig. 6.2**. This is consistent with the 1.1 ± 0.3 background events expected in each of the B_s^0 and B_d^0 mass windows. We derive 90% (95%) C.L. limits of $\mathcal{BR}(B_s^0 \to \mu^+\mu^-) < 5.8 \times 10^{-7} (7.5 \times 10^{-7})$ and $\mathcal{BR}(B_d^0 \to \mu^+\mu^-) < 1.5 \times 10^{-7} (1.9 \times 10^{-7})$. The new $B_s^0 \to \mu^+\mu^-$ limit improves the previous limit [80] by a factor of 3 and significantly reduces the allowed parameter space of R-parity violating and SO(10) SUSY models [77, 79]. The $B_d^0 \to \mu^+\mu^-$ limit is slightly better than the recent limit from the Belle Collaboration [82].

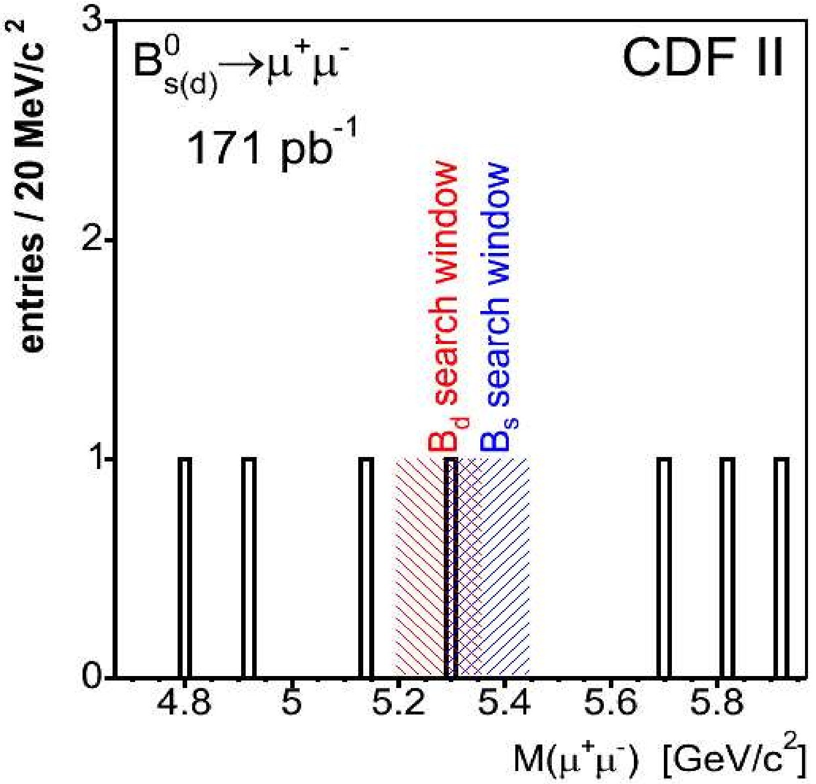

Fig. 6.2. The $\mu^+\mu^-$ invariant mass distribution of the events in the sideband and search regions satisfying all requirements.

Chapter 7

Search for R-parity Violating Stop

It has been shown in Chapter 2 that in SUSY there exists a large parameter region where R_p violating decay of $\tilde{t}_1$ can become dominant over the one-loop level and the three body decay. In this scenario, the stop can be pair-produced and decay into $b\tau$ with the final state being $bb\tau\tau$, see **Fig. 7.1**. In this analysis, we investigate modes with one of the two taus decaying leptonically, while the other one decays via one of the hadronic modes. The experimental signature is an electron/muon, a hadronic tau candidate and two jets.

For reference, a similar Run I analysis with a combined search in electron and muon channels has resulted in a mass limit of $M(\tilde{t}_1) > 122$ GeV/c^2 [91].

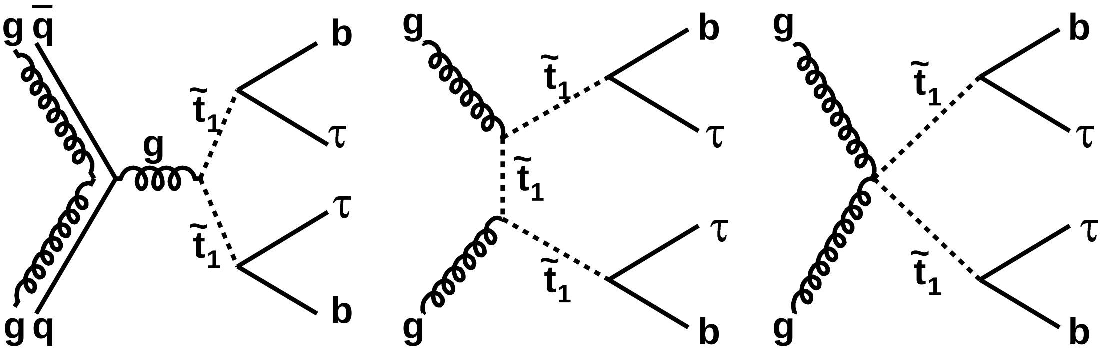

Fig. 7.1. Feynman diagrams for the stop pair production at the Tevatron. We assume that each of the stop quarks decay via R-parity violating coupling to b-quark and τ-lepton.

7.1 Data and Monte Carlo Samples

For the search of stop pair production, we use events collected by the lepton+track triggers, namely TAU_ELE, TAU_CMUP and TAU_CMX, described in Chapter 4 in detail.

For signal $p\bar{p} \rightarrow \tilde{t}_1\bar{\tilde{t}}_1$ we use run dependent PYTHIA MC samples produced using CDF offline software in version 5.3.3. For each of the point in $\tilde{t}_1$ mass we generated a sample of about 50,000 events.

For background studies, we used the following samples:

- $Z/\gamma^* \rightarrow \tau_l\tau_h$ PYTHIA
- $Z/\gamma^* \rightarrow \ell\ell$ PYTHIA
- Inclusive $t\bar{t}$ PYTHIA
- WW, WZ PYTHIA
- ZZ, ALPGEN

7.2 Event Selection

We select events with at least one lepton candidate (either CEM electron, CMUP muon, or CMX muon) with $P_T > 10$ GeV and at least one hadronically-decaying τ-lepton (τ_h) candidate with $P_T^\tau > 15$ GeV/c in the fiducial region of the detector. We then apply lepton (electron or muon) and tau identification selection cuts followed by several event-level cuts designed to improve the sensitivity of the measurement.

7.2.1 Geometrical and Kinematical Acceptance

The geometrical and kinematical event acceptance is defined as a fraction of stop events satisfying the following requirements: an event has at least one pair of lepton ($\ell = e$ or μ) and τ_h candidates that satisfy kinematical and fiducial requirements as specified in **Table 7.1** and $\Delta R(\ell, \tau_h) > 0.7$. Note that these fiducial requirements ensure not only robust event reconstruction, but also high and well understood efficiency of triggering.

For acceptance calculation we use PYTHIA MC and require that selected lepton and tau candidates are matched to generator-level (HEPG) leptons to exclude mistags, e.g. when one of the jets is identified as a tau candidate. While after applying all the identification and selection cuts, these mistags are seen very rarely, at this stage mistagging happens often and therefore meaningful acceptance number requires matching of reconstructed objects to the generator level information. The acceptance depends on the mass of the stop. **Table 7.2** shows the step-by-step efficiencies of the acceptance requirements for signal events with a stop mass of 130 GeV/c^2.

Corrections and Scale Factors

We correct acceptance for the muon channels by additional scaling factors to compensate for the difference in stub-finding efficiencies between data and MC: $f^{CMUP} = 0.939 \pm 0.005$ and $f^{CMX} = 0.990 \pm 0.003$ [92]. In **Table 7.3** we show a summary of acceptance calculations for each of the generated stop mass points. We do not explicitly correct for the efficiency of $|z_0| < 60$ cm cut as comparisons of MC and data have shown a very good agreement; the uncertainty is sufficiently small to be ignored compared to other effects.

Table 7.2 shows the event acceptance for the case of $M(\tilde{t}_1) = 130$ GeV/c^2. We assign an overall systematic uncertainty of 1.5% [93].

7.2.2 Electron Identification Cuts and Efficiency

Table 7.4 shows the efficiency for electron at each stage of the identification cuts. We assign a scale factor of 0.97 with a systematic uncertainty of 1%, as suggested by recent data and MC comparisons [94]. Note that isolations are not included in the ID and are considered separately.

Table 7.1. Geometrical and kinematical requirements for electron, muon, and tau.

Electron:	Muon:	Tau
CdfEmObject	CdfMuon	CdfTau
CEM	CMUP or CMX	
$E_T > 10$ GeV	$p_T > 10$ GeV	$P_T^{seed-trk} > 6$ GeV/c
$P_T > 8$ GeV		$P_T^{vis} > 15$ GeV/c
$\lvert\eta\rvert < 1.0$		$\lvert\eta_{det}^{\tau}\rvert < 1.0$
$\lvert z_0^{e-trk}\rvert < 60$ cm	$\lvert z_0^{\mu-trk}\rvert < 60$ cm	
$\lvert z_{\mathrm{COT}}\rvert < 150$ cm	$\lvert z_{R=137}^{\mu-trk}\rvert < 150$ cm	$\lvert z_{R=137}^{\tau-trk}\rvert < 150$ cm
9 cm $< \lvert z_{\mathrm{CES}}\rvert <$ 230 cm	Fiducial in CMUP or CMX	$9 < \lvert z_{R_{CES}}^{\tau-trk}\rvert < 230$ cm
$\lvert x_{\mathrm{CES}}\rvert < 21.5$ cm		

Table 7.2. Kinematical and geometrical acceptance for the case of $M_{\tilde{t}_1} = 130$ GeV/c^2. Note that reconstructed object (e, μ or τ are required to match to a corresponding HEPG particle). Fiduciality requirement includes XFT fiduciality and CES or CMUP/CMX fiduciality.

$e+\tau$		$\mu^{CMUP}+\tau$		$\mu^{CMX}+\tau$	
Electron:	Efficiency (%)	Muon:	Efficiency (%)	Muon:	Efficiency (%)
CdfElectron	70.6 ± 0.2	CdfMuon:	66.4 ± 0.2		
η	83.6 ± 0.2	CMUP	37.4 ± 0.3	CMX	18.1 ± 0.2
E_T	72.2 ± 0.2				
p_T	93.2 ± 0.2	p_T	78.0 ± 0.3	p_T	74.8 ± 0.5
z_0	96.0 ± 0.1	z_0	96.3 ± 0.2	z_0	96.7 ± 0.2
Fiducial	86.8 ± 0.2	Fiducial	98.3 ± 0.1	Fiducial	92.6 ± 0.4
Total	33.1 ± 0.2		21.8 ± 0.2		7.50 ± 0.12
Tau:					
CdfTau	62.1 ± 0.4		64.0 ± 0.4		63.2 ± 0.8
η	87.6 ± 0.3		88.2 ± 0.4		87.1 ± 0.7
E_T	95.9 ± 0.2		95.7 ± 0.3		95.4 ± 0.4
Seed p_T	97.2 ± 0.2		97.3 ± 0.2		96.9 ± 0.4
Fiducial	90.8 ± 0.3		90.2 ± 0.4		91.0 ± 0.6
Total	46.0 ± 0.4		47.5 ± 0.5		46.3 ± 0.8
$\Delta R(e,\tau)$	96.4 ± 0.2		96.2 ± 0.3		97.0 ± 0.4
α	14.7 ± 0.1		9.96 ± 0.13		3.37 ± 0.08
ScaleFactor	1.000 ± 0.015		0.939 ± 0.005		0.990 ± 0.003
Final α	$14.7 \pm 0.1 \pm 0.2$		$9.35 \pm 0.12 \pm 0.18$		$3.35 \pm 0.08 \pm 0.05$

Table 7.3. Acceptance as a function of stop quark mass. Acceptance values quoted at this point are not corrected for known differences in stub finding efficiency between Data and MC.

	$\tilde{t}_1\bar{\tilde{t}}_1 \to b\bar{b}\tau\tau$ [$M(\tilde{t}_1)$, GeV/c^2]						
	100	110	120	130	140	150	160
α_{cor}^{CEM}	10.7 ± 0.1	12.1 ± 0.1	13.6 ± 0.1	14.7 ± 0.1	15.9 ± 0.2	16.9 ± 0.2	17.7 ± 0.2
α_{cor}^{CMUP}	7.32±0.11	8.14±0.12	9.12±0.13	9.96±0.13	10.7 ± 0.1	11.1 ± 0.1	12.0 ± 0.1
α_{cor}^{CMX}	2.64±0.07	2.82±0.07	3.03±0.08	3.37±0.08	3.40±0.08	3.58±0.08	3.76±0.08

Table 7.4. Efficiency of electron identification cuts using stop MC sample with $M(\tilde{t}_1) = 130$ GeV/c^2. We apply scale factor of 0.97 ± 0.01.

	Efficiency [%]
Track Quality	99.4 ± 0.1
$E^{had}/E^{em} < 0.055 + 0.00045 \times E$	96.9 ± 0.2
$E/p < 2.0$ (for $E_T < 50$ GeV)	95.4 ± 0.2
$-3.0 < Q_{trk} \cdot \Delta x < 1.5$ cm	98.8 ± 0.1
$\|\Delta z\| < 3$ cm	99.6 ± 0.1
$\chi^2_{strip} < 10$	96.7 ± 0.2
$L_{shr} < 0.2$	97.8 ± 0.2
$\|d_0\| < 0.2$ cm	99.6 ± 0.1
Cumulative	85.2 ± 0.4
ScaleFactor	0.97 ± 0.01
Final Efficiency	$85.2 \pm 0.4 \pm 0.9$

7.2.3 Muon Identification Cuts and Efficiency

To improve purity of the signal, a set of muon identification cuts is applied.

Those variables used are explained below;

E^{had}, E^{em} :

The CHA energy or the CEM energy in the calorimeter tower pointed by the muon track. Because muon is a minimum ionizing particle, less energy is fallen in the calorimeter.

d_0 :

Same as that parameter in electron cut.

ΔX_{CMU}, ΔX_{CMU} :

The distance in the r-z plane between the muon stub and the track extrapolation to the stub.

I^{trk} :

Same as that parameter in electron cut.

The full list of cuts and corresponding MC efficiency can be found in **Table 7.5**.

We estimate the efficiency of the muon identification cuts using MC for events passing the acceptance cuts and scale the efficiency using scale factors [92].

Table 7.5. Efficiency of muon ID cuts for CMUP and CMX muons for $Z \to \tau_\mu \tau_h$ and $\tilde{t}_1\bar{\tilde{t}}_1 \to b\bar{b}\tau_\mu\tau_h$ for the case $M(\tilde{t}_1) = 130$ GeV/c^2. We use MC efficiency as a default. We quote alternative efficiencies obtained either directly from data or via MC-to-data comparisons as explained in the text. For all other cuts we use MC and apply scale factors, and assign additional systematics of 4% for CMUP and 1% for CMX.

	CMUP	CMX
Track Quality	99.7 ± 0.1	99.4 ± 0.2
$E^{em} < 2$, $E^{had} < 6$, and $E^{had} + E^{em} > 0.1$ GeV	93.9 ± 0.3	91.2 ± 0.7
$\|d_0\| < 0.2$ cm	99.9 ± 0.1	100.0
$\Delta X_{CMU} < 4$ and $\Delta X_{CMP} < 7$ or $\Delta X_{CMX} < 6$	98.5 ± 0.2	98.3 ± 0.3
Cumulative	92.1 ± 0.4	89.1 ± 0.8
ScaleFactor	0.930 ± 0.04	0.995 ± 0.01
Final Efficiency	$85.7 \pm 0.4 \pm 4.0$	$88.7 \pm 0.8 \pm 1.0$

7.2.4 Tau Identification Cuts and Efficiency

We apply the same hadronic tau ID cuts as in the $Z \to \tau\tau$ cross-section measurement [93], except for the tau tracking isolation. This is because stop events have significantly more activity due to hard jets in the event, which becomes a dominant issue in the efficiency of the isolation cut. In this measurement we estimate the efficiency using MC and correct it using the same scale factors except for the isolation cut. The dominant background in this analysis is $Z \to \tau\tau$ and not QCD. This motivates us to loosen the isolation requirement: no tracks with $p_T > 1$ GeV/c in the isolation cone. However, in this analysis we chose to separate the isolation cuts from identification, and the issues related to isolation are discussed later in this section. Full list of cuts and their efficiencies can be found in **Table 7.6**.

7.2.5 Lepton Isolation Efficiencies

We require that both lepton (e, μ) and tau candidates are isolated. The isolation requirement that we use contains two parts: (i) no jets in an annulus of $0.3 < \Delta R < 0.8$ around the lepton (See **Table 7.7** for jet definition) and (ii) sum of p_T of all tracks around electron or muon candidate in a cone $\Delta R < 0.4$ to be less than 2 GeV/c.

Table 7.6. Efficiency of tau ID cuts for $Z \to \tau_l \tau_h$ and $\tilde{t}_1 \bar{\tilde{t}}_1 \to b\bar{b}\tau_l\tau_h$ for the case $M(\tilde{t}_1) = 130$ GeV/c^2.

Requirement	Electron Channel	Muon Channel	
		CMUP	CMX
Seed Track Quality	98.4 ± 0.2	98.2 ± 0.2	98.3 ± 0.4
$\lvert z_0^{\tau-seed} - z_0^{e/\mu-trk} \rvert \leq 5$ cm	99.4 ± 0.1	99.1 ± 0.2	98.9 ± 0.3
$d_0^{\tau-seed} < 0.2$ cm	97.9 ± 0.2	99.7 ± 0.2	98.1 ± 0.4
$\xi > 0.1$	93.4 ± 0.3	93.1 ± 0.4	92.4 ± 0.8
$M^{track} \leq 1.8$ GeV & $M^{track+\pi^0} \leq 2.5$ GeV	94.1 ± 0.3	95.2 ± 0.4	95.5 ± 0.6
$N_{trk}^{\tau\ cone} = 1$ or 3	85.3 ± 0.5	86.4 ± 0.6	85.0 ± 1.1
Cumulative	71.7 ± 0.6	72.3 ± 0.8	71.5 ± 1.3
ScaleFactor	1.00 ± 0.03	1.00 ± 0.03	1.00 ± 0.03
Final Efficiency	$71.7 \pm 0.6 \pm 2.2$	$72.3 \pm 0.8 \pm 2.2$	$71.5 \pm 1.3 \pm 2.1$

Table 7.7. Jet definition used in this analysis. Jets were reconstructed using standard module at CDF software with the cone size of $\Delta R = 0.4$. Jet energy was corrected using so called Level 5 jet corrections [95].

$\lvert\eta^{det}\rvert$	< 2.4
E_T^{raw}	> 10 GeV
E_T^{cor}	> 15 GeV
$\Delta R(e/\mu/\tau_h, jet)$	> 0.8

Motivation for using the lepton-jet isolation is that the tracking isolation strongly depends on a presence of jets nearby: efficiency becomes very low if a jet happens to be near lepton. **Figure 7.2** shows how average track isolation efficiency depends on ΔR to the closest jet compared to the efficiency for $Z \to \tau\tau$ events, in which jets are rarely present. Note that with a moderate cut of $\Delta R > 0.8$ efficiency in stop events becomes quite similar to the one in $Z \to \tau\tau$ events. Remaining residual difference is small and is partially due to the jet thresholds (a jet with $E_T^{cor} < 15$ GeV can happen to be near the lepton, but will not be considered as a "jet"). The lower bound in lepton-jet isolation is dictated by the fact that electron or tau will always be identified as a jet and therefore we always expect a jet somewhere within $\Delta R < 0.3$ around electron or tau. We keep the same definition for muons for consistency.

With lepton-jet isolation applied, we estimate the track efficiency using PYTHIA MC.

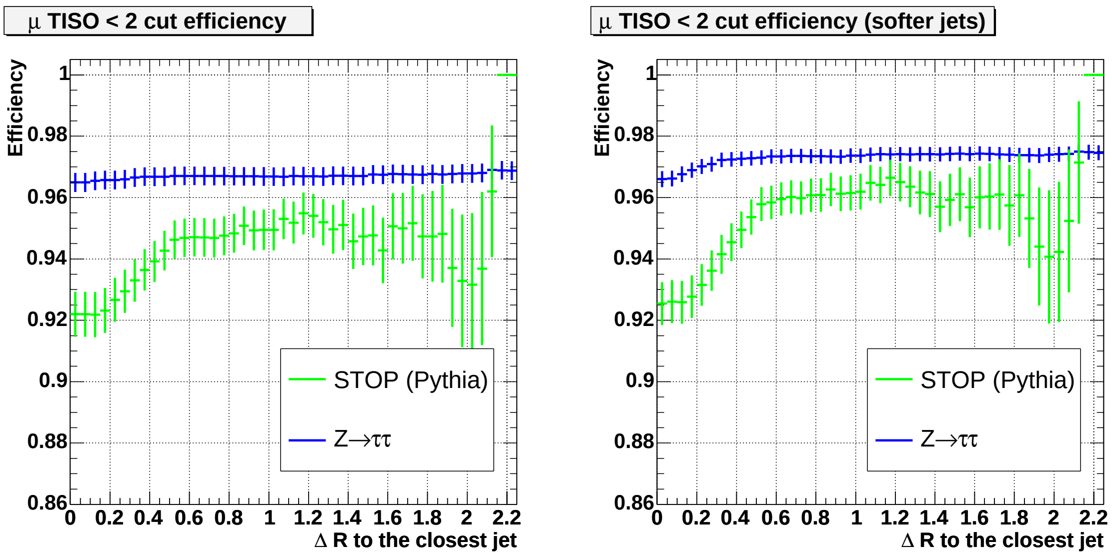

Fig. 7.2. (a) Cumulative efficiency of the lepton track isolation as a function of ΔR, where ΔR is the cut value of minimal separation between jet and a lepton. We compare $Z \to \mu\mu$ and stop events after all other ID cuts applied. This plot shows that track isolation strongly depends on jet closeness; (b) To amplify this effect, we plot the same distribution, but with a softer jet definition threshold ($E_T^{raw} > 6$, $E_T^{cor} > 10$ GeV). This plot shows even better agreement between track isolation efficiencies in Z and stop samples for events with applied jet isolation $\Delta R > 0.8$.

We do not apply any scale factors as our previous studies have indicated a good agreement between data and MC. We separately studied the luminosity dependence and found it to be weak. Note that lepton-jet isolation is much less dependent on the instantaneous luminosity due to a relatively stiff requirement that the jet has to have energy above 15 GeV.

Table 7.8 shows the efficiency of isolation cuts for the set with mass of $M(\tilde{t}_1) = 130$ GeV$/c^2$. We assign a 3% overall systematic uncertainty that well covers difference between isolation in $Z \to \ell\ell$ and stop events and also small differences between $Z \to \ell\ell$ data and MC.

7.2.6 Trigger Efficiency

Trigger efficiencies for the lepton plus track triggers were measured for each of the two legs separately using data taken over the same running period as the one used in this measurement.

Efficiency of the muon leg in the muon plus track trigger was measured using $Z \to \mu\mu$ and Υ events as a function of muon track p_T and associated track P_T [96-98]. Average plateau

Table 7.8. Efficiency of isolation cuts for $\tilde{t}_1\bar{\tilde{t}}_1 \to b\bar{b}\tau_l\tau_h$ for the case $M(\tilde{t}_1) = 130$ GeV/c^2. We assign the systematic uncertainty of 3% for these cuts.

Requirement	Electron Channel	Muon Channel	
		CMUP	CMX
Lepton:			
Jet Separation	90.4 ± 0.4	88.8 ± 0.4	90.7 ± 0.7
$I^{trk}_{\Delta R<0.4} < 2.0$ GeV/c	87.4 ± 0.4	92.9 ± 0.4	93.2 ± 0.7
Tau:			
Jet Separation	93.9 ± 0.4	94.3 ± 0.4	94.1 ± 0.8
$N^{\tau,\,\Delta\Theta}_{trk} = 0$ & $N^{\tau,\,\Delta R}_{trk} = 0$	77.8 ± 0.7	79.3 ± 0.8	79.4 ± 1.4
$I^{\tau,\,\Delta\Theta}_{\pi^0} \leq 0.6$ GeV/c	94.3 ± 0.4	94.4 ± 0.9	94.0 ± 1.5
ScaleFactor	1.00 ± 0.03	1.00 ± 0.03	1.00 ± 0.03

efficiency for the muon leg is found to be approximately 95%.

Efficiency for the electron leg is calculated using a sample of conversion electrons reconstructed in jet and muon data [71, 72].

For the track leg, the measurement of the trigger efficiency [99, 100] is made in assumption that this leg is a hadronic tau and the efficiency is parametrized as a function of several tau variables. In the course of measuring efficiencies, we verified that the trigger efficiencies for the two legs are independent, e.g. we compared efficiency for events with a single tau candidate and for events with tau candidate and an additional loose lepton. Average efficiency for the track leg above 10 GeV/c is approximately 97%, and it shows slow continuous growth toward higher p_T. We attribute this tendency to special features in the XFT track finding algorithm [99].

We calculate average trigger efficiency by convoluting MC with the parametrized trigger efficiency functions, which results for the case $M(\tilde{t}_1) = 130$ GeV/c^2 can be found in **Table 7.9**.

7.2.7 Event Level Cuts and Efficiency

We then apply several topology cuts to remove remaining backgrounds.

Table 7.9. Average trigger efficiency for $Z \to \tau_l \tau_h$ and $\tilde{t}_1 \bar{\tilde{t}}_1 \to b\bar{b}\tau_l\tau_h$ for the case $M(\tilde{t}_1) = 130$ GeV/c^2.

Trigger	$Z \to \tau\tau$	$\tilde{t}_1\bar{\tilde{t}}_1 \to b\bar{b}\tau\tau$
CEM $\varepsilon^e_{L1} \times \varepsilon^e_{L2} \times \varepsilon^e_{L3}$	$96.1 \pm 0.2 \pm 1.0$	$97.1 \pm 0.2 \pm 1.0$
CMUP$\varepsilon^\mu_{L1} \times \varepsilon^\mu_{L2} \times \varepsilon^\mu_{L3}$	$95.8 \pm 0.2 \pm 1.0$	$95.5 \pm 0.3 \pm 1.0$
CMX $\varepsilon^\mu_{L1} \times \varepsilon^\mu_{L2} \times \varepsilon^\mu_{L3}$	$95.3 \pm 0.3 \pm 1.0$	$95.4 \pm 0.6 \pm 1.0$
TAU $\varepsilon^\tau_{L1} \times \varepsilon^\tau_{L2} \times \varepsilon^\tau_{L3}$	$95.2 \pm 0.3 \pm 1.0$	$96.3 \pm 0.5 \pm 1.0$

Table 7.10. Requirements for a pair of tracks to be tagged as a conversion.

$\lvert\Delta(\cot\theta)\rvert \geq 0.04$
$\Delta S_{xy} \geq 0.2$

Conversion Electron Removal

This is applicable to the electron channel only. We remove events, in which primary electron candidate is likely produced by a photon conversion. Definition of a conversion candidate is given in **Table 7.10**, which is the same as the cut in Chapter 5.

Cosmic Ray Removal

Cosmic removal is applicable to the muon channel. Sometimes, cosmic ray will pass through the detector and shower in the calorimeter producing a topology similar to a single muon and a one prong tau candidate. It may even overlap with some activity in the calorimeter, e.g. a jet event. However, we find that such occurrences happen at a completely negligible rate due to the tight selection cuts, e.g. Δz matching, Y_T cut (defined later), jet thresholds incompatible with a soft minimum bias event etc. The only sizable presence of this background is expected in the $n_{jet} = 0$ bin, thus we choose to remove events that simultaneously satisfy two requirements:

$$|\phi_\mu - \phi_\tau^{seed\,track} - \pi| < 0.1, \quad n_{jet} = 0. \tag{7.1}$$

This cut has whatsoever no effect on the signal due to a very unlike topology, but is very effective in rejecting cosmic ray events and helps removing some of the $Z \to \tau\tau$ and $Z \to \mu\mu$ events in the $n_{jet} = 0$ bin.

Table 7.11. $Z \to \mu\mu$ and $Z \to ee$ veto definition.

$Z \to \mu\mu$	$Z \to ee$	
	Calorimeter-Based	Track-Based
Second Track (trk):	Second CdfEmObject (em):	Second Track (trk):
Match to any stub	$E_T > 8$ GeV	$p_T^{trk} > 10$ GeV/c
$p_T \geq$10 GeV/c	$E^{had}/E^{em} < 0.12$	$Iso^{trk}_{\Delta R=0.4} < 4$ GeV/c
		Tower EM Fraction > 0.7
$\lvert z_0^{trk} - z_0^{\mu}\rvert < 5$ cm	$\lvert z_0^{trk} - z_0^{e}\rvert < 5$ cm	
Opposite charge	Opposite charge (if $\lvert\eta\rvert < 1.2$)	Opposite charge
$76 \leq M(\mu, trk) \leq 106$ GeV/c^2	$76 < M(e, em) < 106$ GeV/c^2	$66 < M(e, trk) < 111$ GeV/c^2

Drell-Yan Removal

We remove events with likely $Z \to \mu\mu$ or $Z \to ee$ candidates defined as shown in **Table 7.11**. Note that in the electron channels we use both calorimeter- and track-based veto, the mass window in the second case is wider to accommodate Bremsstrahlung effect. In the track case, to minimize effect on the signal, we additionally require that the EM fraction of total energy in the calorimeter tower the track extrapolates to is larger than 0.7.

In addition to what described above, we noted a number of likely $Z \to ee$ events that were not predicted by MC, particularly in a region of high transverse mass of electron and missing transverse energy, which should indicate cases when the electron leg, which was identified as a tau, is severely mismeasured. The excess was not very large (about 2 sigma effect), but still indicated that there could be some issues with MC predictions for the electron-to-tau fake rate in events of this peculiar topology. We chose to strengthen the $Z \to ee$ suppression by removing events that satisfy all of the following criteria:

$$\frac{(f^{EM}(\tau) - 0.4)^2}{(0.4)^2} + \frac{(\Delta\phi(e,\tau) - 1.5)^2}{(1.5)^2} \geq 1, \quad \Delta\phi > 1.5, \quad M_T(e,\tau) > 35 \text{ GeV}/c^2 \tag{7.2}$$

These selections are motivated by MC, see **Fig. 7.3** showing a 2D distribution of $f^{EM}(\tau)$ versus $\Delta\phi(e,\tau)$ for $Z \to ee +$ 1jet MC events passing all above cuts and also $Y_T > 85$ GeV/c and $M_T(e,\tau) > 35$ GeV/c^2 cuts (these cuts are described in the following subsections).

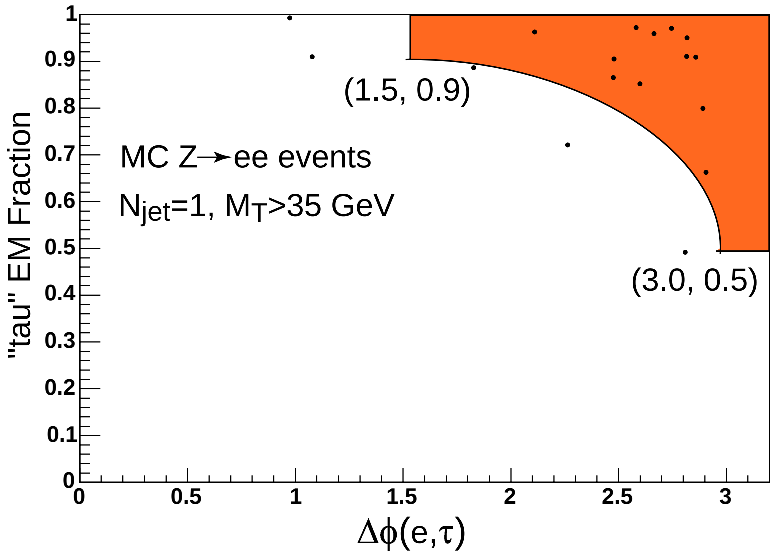

Fig. 7.3. 2D distribution of $f^{EM}(\tau)$ versus $\Delta\phi(e,\tau)$ for $Z \to ee + 1$jet MC events passing all above cuts and also $Y_T > 85$ GeV$/c$ and $M_T(e,\tau) > 35$ GeV$/c^2$ cuts (these cuts are described in the following subsections).

Y_T Cut

To suppress Z+jets and QCD backgrounds, we apply the scalar sum of lepton, tau and missing energy.

$$Y_T(\ell, \tau_h, \not{E}_T) \equiv P_T(\ell) + P_T(\tau_h) + \not{E}_T \tag{7.3}$$

Cut value for the Y_T variable is optimized for the best limit using Bayesian method [101] with real acceptance figures and estimated backgrounds (with some simplifications compared to the full analysis). We assumed that the observed number of events will be in agreement with the background estimation and distributed according to Poissonian statistics. We weighted limit for each possible outcome with the Poissonian probability to predict an average expected limit. We chose optimized value of the cut to be $Y_T \geq 85$ GeV.

N_{jet} and M_T

After all cuts described in the above, a still intolerably high number of background events is expected. We use two additional variables that are found to be very powerful in separating

Table 7.12. Definition of six regions in the M_T versus N_{jet} plane with the dominant contribution indicated for each region. Regions A, B, C and D will be used in setting final limit, regions A' and B' will be used as control regions.

	$M_T < 35$	$M_T > 35$
$N_{jet} \geq 2$	A ($\simeq$ 2/3 of signal, $Z \to \tau\tau$)	B ($\simeq$ 1/3 of signal, W+jets)
$N_{jet} = 1$	A' ($Z \to \tau\tau$)	B' (W+jets)
$N_{jet} = 0$	C ($Z \to \tau\tau$)	D (W+jets)

Table 7.13. Efficiency of event level cuts for 130 GeV stop. The last two cuts are applicable for region A only.

Cut	$e + \tau$	CMUP $\mu + \tau$	CMX $\mu + \tau$
$Q_l \times Q_\tau = -1$	99.5 ± 0.1	99.5 ± 0.2	99.5 ± 0.3
Conversion Removal	98.2 ± 0.3	–	–
Cosmic Removal	–	100.0	100.0
$Z \to ll$ Removal	90.2 ± 0.5	99.8 ± 0.1	99.5 ± 0.3
$Y_T(l, \tau, \not{E}_T) > 85$ GeV	84.8 ± 0.7	85.9 ± 0.8	82.7 ± 1.6
$N_{jet} \geq 2$	84.6 ± 0.8	84.7 ± 0.9	82.8 ± 1.7
$M_T(l, \not{E}_T) < 35$ GeV	71.3 ± 1.1	72.0 ± 1.2	71.1 ± 2.3
Cumulative	45.1 ± 1.0	52.0 ± 1.2	48.1 ± 2.1

signal and background, these variables are the number of jets (defined as in **Table 7.7**), N_{jet}, and the transverse mass of electron and $\not{E}_T$ defined as

$$M_T(l, \not{E}_T) = \sqrt{2 \times {p_T}^l \not{E}_T \times (1 - \cos\Delta\Theta)} \tag{7.4}$$

Majority of signal events have two or more jets in the final state (backgrounds typically have one or no jets) and tend to have moderate values of M_T, as opposed to W+jets events that most of the time have large M_T. However, we found that using these variables as cuts is not as effective as a statistical analysis of events passing and failing these cuts. As it will be shown later, this procedure also allows estimating the contribution of the difficult to evaluate W+jets background.

We categorize events according to which of the six regions defined in the M_T versus N_{jet} plane (see **Table 7.12**) they fall. With known expected fractions of signal and background events in each region, one can perform a fit of the data and background expectations for the stop cross-section.

Table 7.14. Full selection efficiency for region A as well as scale factors required to obtain efficiency for the complementary regions B, A' and B'. Full selection efficiency for regions C and D is always less than 0.01% and can be safely ignored compared to expected background contribution in these regions. Scale factors are included (including corrections for the stub finding efficiency).

	$\tilde{t}_1\bar{\tilde{t}}_1 \to b\bar{b}\tau\tau$ [$M(\tilde{t}_1)$, GeV/c^2]						
	100	110	120	130	140	150	160
ε_A^{CEM}[%]	0.94±0.04	1.37±0.05	1.67±0.05	2.07±0.06	2.27±0.06	2.40±0.07	2.66±0.07
f_B/f_A	42.2 ± 2.8	35.7 ± 2.2	41.9 ± 2.0	40.2 ± 1.8	41.0 ± 1.7	46.8 ± 1.8	47.0 ± 1.7
$f_{A'}/f_A$	37.0 ± 2.7	24.1 ± 1.8	20.1 ± 1.4	16.9 ± 1.2	13.2 ± 1.0	12.6 ± 1.0	11.7 ± 0.9
$f_{B'}/f_A$	12.1 ± 1.5	11.2 ± 1.2	8.4 ± 0.9	7.4 ± 0.8	6.3 ± 0.7	6.8 ± 0.7	5.3 ± 0.6
f_C/f_A	3.2 ± 0.8	2.2 ± 0.6	1.0 ± 0.3	0.6 ± 0.2	0.6 ± 0.2	0.6 ± 0.2	0.3 ± 0.1
f_D/f_A	1.3 ± 0.5	0.4 ± 0.2	0.3 ± 0.2	0.6 ± 0.2	0.3 ± 0.2	0.2 ± 0.1	0.1 ± 0.1
ε_A^{CMUP}[%]	0.77±0.04	1.04±0.04	1.31±0.05	1.60±0.05	1.80±0.05	1.87±0.06	2.10±0.06
f_B/f_A	37.5 ± 2.8	34.6 ± 2.3	34.6 ± 2.0	38.9 ± 1.9	38.7 ± 1.8	38.6 ± 1.8	46.1 ± 1.8
$f_{A'}/f_A$	33.3 ± 2.7	27.4 ± 2.1	21.6 ± 1.6	17.4 ± 1.3	14.1 ± 1.1	14.5 ± 1.1	13.2 ± 1.0
$f_{B'}/f_A$	9.3 ± 1.4	9.6 ± 1.2	8.7 ± 1.0	6.5 ± 0.8	5.7 ± 0.7	5.5 ± 0.7	5.7 ± 0.7
f_C/f_A	3.9 ± 0.9	2.4 ± 0.6	1.0 ± 0.4	1.0 ± 0.3	0.7 ± 0.2	0.5 ± 0.2	0.4 ± 0.2
f_D/f_A	1.5 ± 0.6	1.0 ± 0.4	0.8 ± 0.3	0.2 ± 0.15	0.2 ± 0.1	0.2 ± 0.1	0.4 ± 0.2
ε_A^{CMX}[%]	0.26±0.02	0.34±0.03	0.41±0.03	0.56±0.03	0.61±0.04	0.66±0.04	0.73±0.04
f_B/f_A	35.4 ± 5.2	43.5 ± 4.9	41.2 ± 4.4	38.8 ± 3.6	41.3 ± 3.5	45.2 ± 3.5	41.2 ± 3.2
$f_{A'}/f_A$	39.4 ± 5.5	18.2 ± 3.2	26.5 ± 3.5	19.8 ± 2.6	10.7 ± 1.9	10.5 ± 1.8	10.2 ± 1.6
$f_{B'}/f_A$	11.0 ± 2.9	12.4 ± 2.7	10.3 ± 2.2	8.6 ± 1.7	10.7 ± 1.9	6.5 ± 1.4	3.6 ± 1.0
f_C/f_A	6.3 ± 2.2	3.5 ± 1.4	0.5 ± 0.5	0.4 ± 0.4	0.	0.9 ± 0.5	0.3 ± 0.3
f_D/f_A	0.8 ± 0.8	0.6 ± 0.6	0.5 ± 0.5	0.4 ± 0.4	0.	0.	0.

We use MC to estimate efficiency of the event level cuts in each of the regions. Results for region A for 130 GeV stop are shown in **Table 7.13**. **Table 7.14** gives full selection efficiencies for region A as well as scale factors required to obtain efficiency for the complementary regions B, A' and B' for a range of stop masses. Full selection efficiency for regions C and D is always less than 0.01% and can be safely ignored compared to expected background contribution in these regions. **Figure 7.4** shows full selection efficiency for region A versus stop mass for CEM electron, CMUP muon, CMX muon and combined CMUP+CMX muon channels.

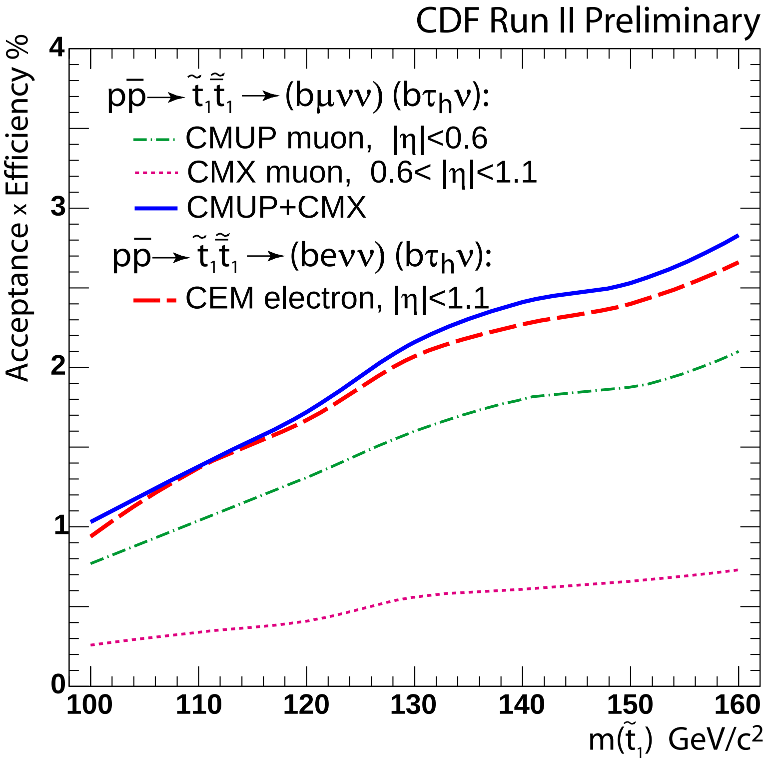

Fig. 7.4. Full selection efficiency for region A versus stop mass for CEM electron, CMUP muon, CMX muon and combined CMUP+CMX muon channels.

7.3 Uncertainties

In this section we discuss remaining systematic and theoretical uncertainties not discussed earlier.

7.3.1 Parton Distribution Functions

We have used the re-weighting method [102, 103]. This procedure assigns each event a weight in the (Q^2, x_1, x_2) space. The reference set (the one with all weights being equal to 1) was the median CTEQ6M PDF set, and the re-weighing procedure was applied using PDF sets with each of the 20 eigenvectors shifted up or down. All positive and negative variations in the full event selection due to shifts in each of the 20 eigenvectors were summed up separately in quadratures. If changes in the selection efficiency obtained by shifting the same eigenvector up

Table 7.15. Estimated uncertainties in full selection efficiency due to variations in PDF for signal.

	$\tilde{t}_1\bar{\tilde{t}}_1 \to b\bar{b}\tau\tau$ $[M(\tilde{t}_1)$, GeV/$c^2]$						
	100	110	120	130	140	150	160
	$e + \tau$ *Channel*						
Negative [%]	5.9	4.4	5.1	4.7	4.3	3.7	4.5
Positive [%]	4.3	3.2	3.3	3.9	2.7	2.1	2.9
Average [%]	5.1	3.8	4.2	4.3	3.5	2.9	3.7
	$\mu + \tau$ *Channel*						
Negative [%]	6.3	6.1	5.6	4.8	4.2	4.9	3.4
Positive [%]	4.6	4.2	3.7	3.0	2.4	3.0	2.2
Average [%]	5.5	5.2	4.7	3.9	3.3	4.0	3.3
α_s variation [%]	0.36	0.25	0.18	0.18	0.13	0.10	0.09
Average [%]	5.5	5.2	4.7	3.9	3.3	4.0	3.3

or down were positive (or negative) in both cases, the largest deviation was counted toward the positive (negative) sum and zero toward negative (positive) sum. The results of these studies are shown in **Table 7.15**. For the final uncertainty, we use a symmetrical error calculated as an average value for each mass point

7.3.2 Initial and Final State Radiation

The uncertainty due to the initial and final state radiation is estimated by separately turning off the ISR and FSR switches in PYTHIA. **Table 7.16** shows the full event selection efficiency (includes acceptance, ID and event-topology cuts) for the default and the two deviated cases.

These results are in agreement with the previous Run I studies indicating that these uncertainties are small. Note that the differences between the deviated cases and the default are within the statistical uncertainty. For assigning a systematic uncertainty in this case, we use the largest relative difference between the central values across all stop mass points for each channel, i.e. 1.4(2.7)% for ISR and 1.2(1.0)% for FSR for the $e(\mu) + \tau$ channel. We effectively assume that the large statistical uncertainty will cover any unaccounted effects of ISR/FSR.

Table 7.16. Results of the studies of the systematic effects due to initial and final state radiation. Full event selection is quoted for the default PYTHIA settings as well as for the cases when ISR (or FSR) switch was turned off. Uncertainty quoted is a relative difference between the central values for the default and shifted cases.

		Default	ISR off		FSR off	
			α	ε_α [%]	α	ε_α [%]
110 GeV	e	1.41 ± 0.05	1.39 ± 0.05	1.4	1.40 ± 0.05	0.4
	μ	1.61 ± 0.06	1.59 ± 0.05	1.0	1.59 ± 0.05	1.0
130 GeV	e	2.09 ± 0.06	2.10 ± 0.06	0.7	2.11 ± 0.06	1.2
	μ	2.36 ± 0.07	2.42 ± 0.07	2.7	2.38 ± 0.07	0.9
150 GeV	e	2.42 ± 0.07	2.42 ± 0.07	0.2	2.45 ± 0.07	1.1
	μ	2.88 ± 0.07	2.87 ± 0.07	0.4	2.90 ± 0.07	0.9

7.3.3 Missing E_T

Another possible systematic effect that has to be considered is the accuracy in simulating the missing transverse energy, $\not\!\!E_T$, in Monte Carlo. We use event topology cuts that are correlated with $\not\!\!E_T$.

For reference, we compare the distributions of $\not\!\!E_T$ in $Z \to ee$ data and MC by selecting events passing acceptance requirements[1] and a requirement that the invariant mass of the two electron candidates falls within a ±5 GeV window around the Z mass. Events are also required to have opposite charge and have to pass conversion removal.

To estimate a systematics uncertainty, we assume that the possible (although not observed) deviation between $\not\!\!E_T$ in data and MC can be parameterized as an overall scale shift, $\not\!\!E_T \to \not\!\!E_T \times (1+f)$. This is illustrated in **Fig. 7.5(a)** that shows comparison of the $\not\!\!E_T$ distribution in data and "scaled" MC for values f between -0.1 and +0.1 for events with $N_{jet} = 0$, 1 and ≥ 2 in the definition adopted in this analysis. Plots in the middle column correspond to the default MC case. Obviously, the agreement is quite good. To estimate the uncertainty, we fit the $\not\!\!E_T$ distribution in data for $Z \to ee$ events to the MC prediction with shifted $\not\!\!E_T$ as a function of f as illustrated in **Fig. 7.5(b)**. It is easy to see that the shift values are bound by $f = \pm 0.1$ for all N_{jet} cases within at least 68% C.L.

---

[1] Note that $Z \to ee$ electrons nearly always pass as reconstructed tau objects

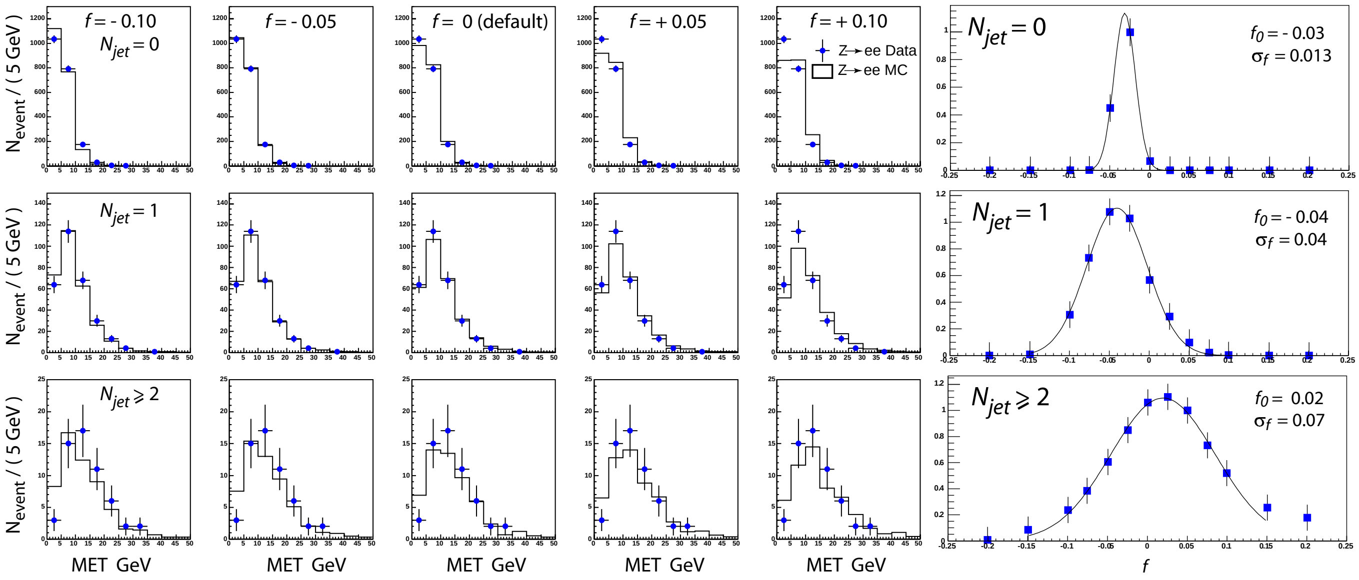

(a) (b)

Fig. 7.5. (a) Shapes of the missing transverse energy, $\not\!\!E_T$, distributions in $Z \to ee$ events in Data compared to MC with applied shifts in transverse energy of the form $\not\!\!E_T = \not\!\!E_T(1+f)$. The middle column corresponds to the default MC case ($f = 0$). Events with the number of jets $N_{jet} = 0$, 1 and ≥ 2 are compared separately and show good agreement. Integrals of MC distributions are normalized to the number of events observed in data; (b) Probability density function as a function of shift parameter f obtained by fitting the distributions on the left. We conservatively assume that $|f| < 0.1$, which covers all N_{jet} cases within at least 68% C.L..

Thus obtained f can be used to smear the $\not\!\!E_T$ distribution in signal MC events and use the difference with the default case as a systematic uncertainty associated with the accuracy of $\not\!\!E_T$ simulation. Note that in the signal events $\not\!\!E_T$ is a vector sum of the "real" $\not\!\!E_T$ contributions associated with neutrinos (and also muons) in the final state and the "instrumental" one associated with various mismeasurements resulting in artificially measured $\not\!\!E_T$. As one does not expect "real" $\not\!\!E_T$ in $Z \to ee$ events, the measurement of f is applicable only to the "instrumental" part. Therefore, for each signal event in MC, we "correct" the measured[2] $\not\!\!E_T$ as:

$$\vec{\not\!\!E}_T^{\,meas\ cor} = \sum \vec{p}_T^{\,\nu} + (\vec{\not\!\!E}_T^{\,meas} - \sum \vec{p}_T^{\,\nu}) \times (1+f) \tag{7.5}$$

Note that in the trivial case of $f = 0$, this correction defaults to applying no correction at all. We apply this procedure with $f = \pm 0.1$ to each of the signal samples and the results of these

---

[2] It still has to be corrected for the muon in case of the $\mu + \tau$ channel, as $\not\!\!E_T$ due to muon is "real" as opposed to "instrumental" $\not\!\!E_T$ due to jet mismeasurements, additional minimum bias interactions, beam effects etc.

Table 7.17. Estimated uncertainties in full selection efficiency obtained by varying the $\not\!\!E_T$ distribution as described in the text.

	$\tilde{t}_1\bar{\tilde{t}}_1 \to b\bar{b}\tau\tau$ [$M(\tilde{t}_1)$, GeV/c^2]						
	100	110	120	130	140	150	160
$e+\tau$	4.2	2.6	4.2	3.0	3.8	3.6	3.3
$\mu+\tau$	2.2	3.1	2.4	3.4	2.2	3.1	2.2

Table 7.18. Estimated uncertainties in full selection efficiency due to variations in jet energy scale (absolute and relative combined) using the standard method at CDF II.

	$\tilde{t}_1\bar{\tilde{t}}_1 \to b\bar{b}\tau\tau$ [$M(\tilde{t}_1)$, GeV/c^2]						
	100	110	120	130	140	150	160
	$e+\tau$ *Channel*						
+1 σ [%]	2.8	2.5	0.4	2.5	1.4	1.2	1.1
+1 σ [%]	1.4	2.3	5.3	2.7	0.2	0.4	2.1
Average [%]	2.1	2.4	2.8	2.6	0.8	0.8	1.6
	$\mu+\tau$ *Channel*						
+1 σ [%]	1.8	2.7	2.6	1.8	1.0	0.9	1.3
-1 σ [%]	4.0	2.9	3.8	2.2	1.9	1.1	1.4
Average [%]	2.9	2.8	3.2	2.0	1.5	1.0	1.4

studies are presented in **Table 7.17**. We think that this simple approach is an overestimation of the effect, as this effect has to be related to resolutions and not to the shift in overall scale. We intend to improve this estimation in the next version of this analysis.

7.3.4 Jet Energy Scale

To estimate the effect of imprecise knowledge of the jet energy scale, we used a standard method provided in the jet correction method [95]. This method allows shifting the jet scale up or down by 1 sigma. The sensitivity in the full event selection depends on how often signal events have jets that are around the threshold. By increasing stop mass, one expects jets to have higher and higher typical energies, which should decrease the importance of this uncertainty. Results of our estimations in **Table 7.18** agree with this observation, although presence of two jets somewhat smears the picture. For the final uncertainty, we use a symmetrical error with

Table 7.19. Full list of the systematic effects considered in this study. The first number in each column corresponds to the $e+\tau$ channel, second one to the $\mu+\tau$ channel.

	$\tilde{t}_1\tilde{t}_1 \to b\bar{b}\tau\tau$ $[M(\tilde{t}_1)$, GeV$/c^2]$						
Systematics Type	100	110	120	130	140	150	160
PDF	4.6(5.5)	3.8(5.2)	4.2(4.7)	3.9(3.9)	3.5(3.3)	2.9(4.0)	3.7(3.0)
ISR	1.4(2.7)	1.4(2.7)	1.4(2.7)	1.4(2.7)	1.4(2.7)	1.4(2.7)	1.4(2.7)
FSR	1.0(1.0)	1.0(1.0)	1.0(1.0)	1.0(1.0)	1.0(1.0)	1.0(1.0)	1.0(1.0)
Jet Scale	3.4(2.9)	3.4(2.8)	3.6(3.2)	2.7(2.0)	1.4(1.5)	1.0(1.0)	1.0(1.0)
$\not\!\!E_T$	4.2(2.2)	2.6(3.1)	4.2(2.4)	3.0(3.4)	3.8(2.2)	3.6(3.1)	3.3(2.2)
α $e(\mu)$	1.5(1.7)	1.5(1.7)	1.5(1.7)	1.5(1.7)	1.5(1.7)	1.5(1.7)	1.5(1.7)
$e(\mu)$ ID	1.0(3.0)	1.0(3.0)	1.0(3.0)	1.0(3.0)	1.0(3.0)	1.0(3.0)	1.0(3.0)
τ ID	3.0	3.0	3.0	3.0	3.0	3.0	3.0
ISO	2.0	2.0	2.0	2.0	2.0	2.0	2.0
Total $e+\tau$	8.3	7.2	8.2	7.1	7.0	6.4	6.7
Total $\mu+\tau$	8.8	8.8	8.4	8.0	7.2	7.7	6.9

the value obtained as an average of the up and down shifts. This corresponds to an assumption that the shape of the distribution for the lowest E_T jet in the small vicinity of the threshold can be approximated by a constant.

7.3.5 Final Systematics Tally

Full list of all systematic uncertainties considered in this analysis is shown in **Table 7.19**. The list includes uncertainties discussed in this section as well as those considered earlier to provide a complete reference of all uncertainties affecting this study.

7.3.6 Theoretical Uncertainties

We analyzed the dependence of the theoretical cross-section on a choice of the PDF set by using CTEQ6 infrastructure. We also studied the cross-section dependence on a choice of the renormalization and factorization scales by using a half and a double of the default values. We found that PDF uncertainties are surprisingly large[3] and are comparable to the effect due to variations in the scale. There is more detailed discussion on this at the end, when a mass limit

---

[3] PDF uncertainty is an order of 10% mainly due to eigen-vectrors 5 and 15, which are related to the high x gluon fraction

is calculated.

7.4 Background Estimation

The backgrounds to our signal, which may also produce $jj\tau\tau$ final states, are $Z+$ jet events, diboson events, top events, $W+$ jet and QCD. We describe these backgrounds and methods we use to estimate their contribution.

7.4.1 $Z \to \tau\tau$

Though $Z \to \tau\tau$ events pass the most of the selections, their contamination is reduced by using $N_{jet} \geq 2$ cut. We estimate $Z \to \tau\tau$ contribution using PYTHIA MC and applying the same cuts as in the data analysis.

Estimated $Z \to \tau\tau$ rate is corrected for known scale factors (ID and reconstruction efficiencies) and trigger efficiency. Corresponding uncertainties are propagated into final estimation of $Z \to \tau\tau$ yield.

Correction for N_{jet} Distribution in PYTHIA

It is known that PYTHIA MC does not reproduce the number of jets distribution observed in data. **Figure 7.6** shows the distribution for the number of jets in $Z \to ee$ data and MC. Data were selected in the same way as in the main analysis except that $\xi-$cut in tau candidate selection was reversed, $Z \to ee$ removal was disabled and the events were required to fall into the mass window of $66 < M_{ee} < 116$ GeV/c^2. We correct the problem of N_{jet} distribution in MC using re-weighting of the $Z \to \tau\tau$ MC events as described in the remainder of this subsection.

Seemingly a simple way to correct MC will be to use weights using information in **Fig. 7.6**. However, these weights apply to the "unbiased" selection of the Z-boson, while the degree of "incorrectness" of PYTHIA MC prediction for the number of jets in Z events may depend on

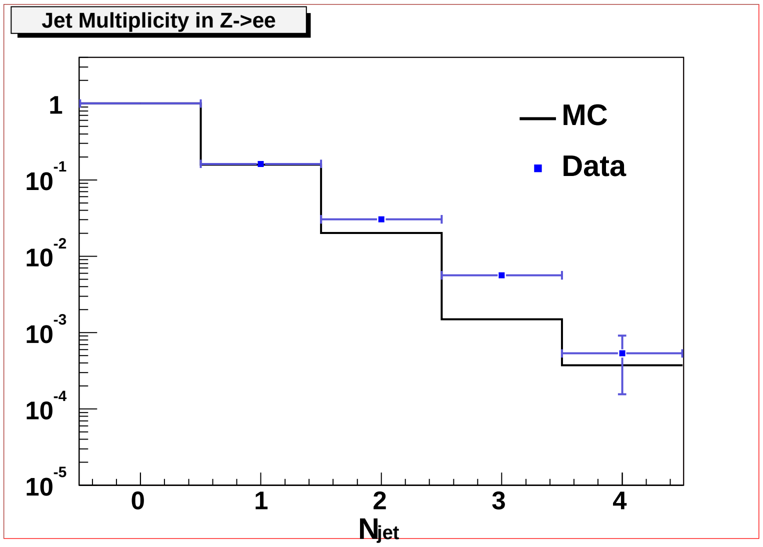

Fig. 7.6. The number of jets distribution in $Z \to ee$ in data and MC. Each distributions are normalized to unity at $N_{jet} = 0$.

the event topology, i.e. the required weights can be a function of η and p_T of the Z-boson, η^Z and p_T^Z. If these weights are not uniform, the event topology cuts, which are correlated with the dynamics of the Z boson, may preferentially choose certain regions in the η^Z-p_T^Z space where the weights can be different from those in the "unbiased" sample.

Weighting factors are obtained from comparison between unbiased samples of $Z \to ee$ events in MC and data[4] as a function of η^Z and p_T^Z. First, for each bin in the η^Z-p_T^Z plane, we define the fraction of events having a certain number of jets, n_{jet}:

$$\begin{aligned} f_0(\eta, p_T) &= \frac{N_{ev}(\eta, p_T, n_{jet} = 0)}{N_{ev}(\eta, p_T, n_{jet} \geq 0)}, \quad f_1(\eta, p_T) = \frac{N_{ev}(\eta, p_T, n_{jet} = 1)}{N_{ev}(\eta, p_T, n_{jet} \geq 0)}, \\ f_2(\eta, p_T) &= \frac{N_{ev}(\eta, p_T, n_{jet} \geq 2)}{N_{ev}(\eta, p_T, n_{jet} \geq 0)}. \end{aligned} \tag{7.6}$$

We calculate these ratios for both data and MC $Z \to ee$ events, $f_i^{Data}(\eta, p_T)$ and $f_i^{MC}(\eta, p_T)$, respectively. We then define weights $w_i(\eta, p_T)$ as

$$w_i(\eta, p_T) = \frac{f_i^{Data}(\eta, p_T)}{f_i^{MC}(\eta, p_T)}. \tag{7.7}$$

These weights can then be used to correct the distribution for the number of jets in MC

---

[4] $Z \to ee$ events were selected in the same way as for the $\not\!\!E_T$ systematics studies, e.g. no event level cuts other than the requirement of opposite sign were applied in selection.

Table 7.20. Scale factors for $Z \to \tau\tau$ MC prediction for the number of events with $n_{jet} = 0$, 1 and ≥ 2. Scale factors are calculated for events passing all selection cuts and for events passing all cuts and failing the M_T cut. These scale factors are equally applicable to the MC efficiencies of corresponding cuts on the number of jets.

	$R(i)$	
i	$M_T < 35$ GeV/c^2	$M_T > 35$ GeV/c^2
0	0.993 ± 0.005	0.992± 0.008
1	0.98 ± 0.05	0.92 ± 0.09
≥2	1.4 ± 0.3	2.2 ± 1.2

$Z \to \tau\tau$ events. We first apply all other event cuts including event topology selections to the $Z \to \tau\tau$ MC events and then correct on a bin-by-bin basis the distribution for the number of jets. We finally obtain the averaged corrected efficiency for the cut on the number of jets as

$$\tilde{\varepsilon}(n_{jet} = i) = \frac{N_{ev}(n_{jet} = i)}{N_{ev}(n_{jet} \geq 0)} = \frac{\sum w_i(\eta, p_T) N_{ev}^{Z\to\tau\tau\ MC}(\eta^Z, p_T^Z, n_{jet} = i)}{\sum N_{ev}^{Z\to\tau\tau\ MC}(\eta^Z, p_T^Z, n_{jet} = i)}, \tag{7.8}$$

where the sum in denominator runs over bins in the η^Z-p_T^Z plane, and in the denominator also over all n_{jet}.

It is more convenient to define an average scale factor $R(i)$ that can be used to correct the $Z \to \tau\tau$ MC prediction for the number of events passing n_{jet} cut as

$$R(i) = \frac{\sum w_i(\eta^Z, p_T^Z) N_{ev}^{Z\to\tau\tau\ MC}(\eta^Z, p_T^Z, n_{jet} = i)}{\sum N_{ev}^{Z\to\tau\tau\ MC}(\eta^Z, p_T^Z, n_{jet} = i)}. \tag{7.9}$$

We also calculate the scale factor for the predicted number of $Z \to \tau\tau$ events in the complementary region of $M_T > 35$GeV/c^2, which will be needed in the final fitting procedure, and both results are shown in **Table 7.20**. Note that the statistical uncertainty due to the number of $Z \to \tau\tau$ MC events passing all cuts is included in the scale factor, i.e. the uncertainty quoted should not be added to the statistical error in the estimation of this background.

Another point we would like to mention is that while we properly correct the expected average number of the $Z \to \tau\tau$ events passing $n_{jet} \geq 2$ cut, the jet dynamics was never considered, e.g. it is possible that jet E_T distributions in data and MC may differ and the overall scale factor that we use will not correct that difference.

7.4.2 QCD

Light-quark QCD backgrounds usually get into the sample via one jet faking an electron (e.g. conversions), while the other jet (or a part of it) is faking a τ candidate. Typically, the multiplicity of fake τ's from jets peaks in a two-prong bin for the range of jet E_T and p_T^τ characteristic for this analysis [104]. Heavy flavor QCD backgrounds have two important features that distinguish the way they penetrate the dataset. First, there are "real" electrons from the semileptonic decays of heavy flavor quarks, and, second, "tau" fakes from heavy flavor jets have slightly different shape of the multiplicity distribution likely due to the decay modes of b mesons[5]. This background is estimated using the lepton isolation extrapolation. As an important feature common for QCD backgrounds the lepton isolation, $I^{trk}_{\Delta R<0.4}$, is distributed in a flat to the first order for fake electrons inside jets. This allows estimating the number of events in the signal region $I^{trk}_{\Delta R<0.4} < 2.0$ GeV/c by using events in the "sideband" region $2.0 < I^{trk}_{\Delta R<0.4} < 10.0$ GeV/c. For example, after the cuts are applied in the electron channel, we find no such events in region A (See **Table 7.12**), which propagates into an estimated $0.00^{+0.25}_{-0.00}$ expected rate of QCD events in signal region.

7.4.3 $Z/\gamma^* \to \mu\mu$ and $Z/\gamma^* \to ee$

$Z/\gamma^* \to \mu\mu$ background events enter the sample via two modes: (i) one of the muons passes hadronic tau requirements by leaving substantial deposition in the calorimeter, or (ii) the recoil jet in $Z/\gamma^* \to \mu\mu$ is misidentified for a hadronic tau while the event pass $Z \to \mu\mu$ candidate removal either because one of the muons is not reconstructed (e.g. fall outside the detector coverage) or the invariant mass of the two muon candidates falls outside the Z window mass cut. We use PYTHIA MC to estimate the background contamination due to $Z/\gamma^* \to \mu\mu$ and find it negligible in signal region. $Z \to ee$ background contributes more because of a higher electron to tau fake rate and due to Bremsstrahlung.

---

[5] For example, some of the "heavy" mesons are ready candidates for fake τ's ($D^{\pm}$ has mass of 1.9 GeV/c^2 compared to $m_\tau = 1.8$ GeV/c^2 and decays into three pions)

7.4.4 $t\bar{t}$ and Diboson

These two backgrounds are dominant physics backgrounds in a sense that they have real lepton and a hadronic tau. These backgrounds can be reliably estimated using corresponding MC and known NLO cross-sections. The cross-sections that we used for $t\bar{t}$, WW, WZ and ZZ processes were 6.7, 12.4, 3.78 and 1.4 pb correspondingly.

7.4.5 W+jets

W+jets background finds its way into our sample via jet faking a tau candidate. This background can be strongly suppressed by the event topology cuts that effectively require remaining W+jet events to have large transverse mass, M_T, which is equivalent to require a heavy boost of the W, thus diminishing its contribution. Note that W+jets have two components: $W(\to \ell)$+jets and $W(\to \tau \to \ell)$+jets, and these two components are somewhat different. Although $W \to \tau$ is suppressed by the branching ratio, the presence of the neutrinos from W and τ results in typically relatively low $\not\!\!E_T$ and M_T values because the neutrinos partially compensate to each other.

Although the remaining W background is relatively small, these events are topologically very similar to signal and their contribution is difficult to estimate without relying on MC tau fake rates, which are hardly reliable. To estimate the W+jets contribution, we used the four regions defined in **Table 7.12** and perform statistical estimation of the W+jets rate. The fit procedure is discussed in the following section, but an important assumption we make about W+jet events is that the rate of W events scales so that $f^W_{AC} \simeq f^W_{BD}$, where $f^W_{AC} = N^W_A/N^W_C$ and $f^W_{BD} = N^W_B/N^W_D$ (N^W_X represents the number of W+jets events in region X).

Table 7.21. The ratio of the number of W+jets events with the number of "extra" jets $n_{jet}^{extra} = 1$ and ≥ 2 to the number of events with $n_{jet}^{extra} = 0$. These results were obtained using PYTHIA MC for $W \to e$ and $W \to \tau \to e$ sub-channels and in the regions $M_T < 35$ GeV/c^2 and $M_T > 35$ GeV/c^2.

	$W \to e$			$W \to \tau \to e$		
i	$M_T < 35$	$M_T > 35$	f_{AC}^W/f_{BD}^W	$M_T < 35$	$M_T > 35$	f_{AC}^W/f_{BD}^W
$n_{jet}^{extra} = 1$	0.205 ± 0.016	0.185± 0.006	1.11±0.09	0.203±0.015	0.198±0.018	1.03±0.15
$n_{jet}^{extra} \geq 2$	0.031 ± 0.007	0.030 ± 0.003	1.0±0.2	0.044±0.008	0.026±0.007	1.7±0.6

W+**jets Events:** N_{jet} **vs** M_T

To verify the expected scaling, we use a W+jet PYTHIA MC sample. We compare events passing all selection criteria and categorize them according to the number of extra jets[6] in the event. In **Fig. 7.7**, we show the ratio of the number of events with $n_{jet}^{extra} \geq 2$ to the number of events with $n_{jet}^{extra} = 0$ as a function of M_T for $W \to e$ and $W \to \tau \to e$ events. The statistics is low, but the ratios are in statistical agreement. We repeat the same calculation for the ratio of the number of events with $n_{jet}^{extra} = 1$, where the statistics is much higher and find a good agreement, see **Fig. 7.8**.

Table 7.21 shows the calculated fractions $f_{AC}^W = N_A^W/N_C^W$ and $f_{BD}^W = N_B^W/N_D^W$ along with those predicted by MC in each region. We conclude that one can define a value $r = f_{BD}^W/f_{AC}^W$ and safely assume that $0.5 < r < 1.5$: this range covers both the (statistically insignificant) differences between $W \to \tau \to \ell$ and $W \to \ell$ samples and also between the measured MC values of f_{AC}^W and f_{BD}^W.

7.4.6 Final Background Tally

Table 7.22 presents a summary of the expected number of background events for each of the six regions from all sources except W+jets events that will be considered separately. The calculation assumes that the integrated luminosity for the CMUP and CEM data is 197 pb^{-1} and 178 pb^{-1} for the CMX data. These numbers include corresponding reconstruction and

---

[6] Remember that one of the jets has to fake a tau candidate, so that an event with one what we call "extra jet" is really a $W + 2$ jets event.

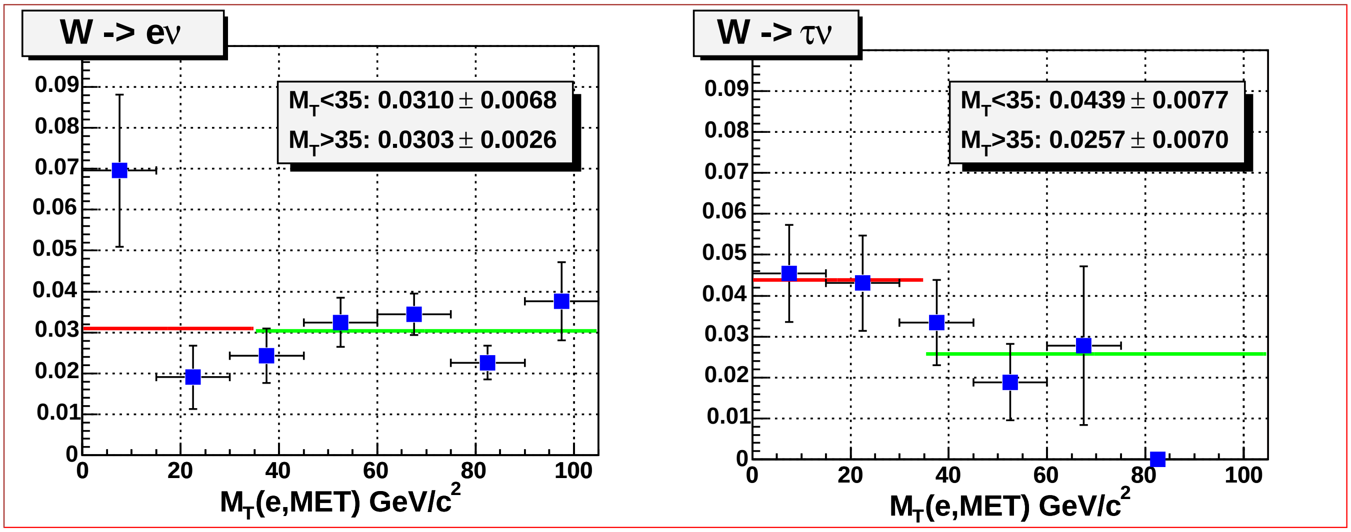

Fig. 7.7. The ratio of $N^{ev}(N_{jet} \geq 2)/N^{ev}(N_{jet} = 0)$ as a function of M_T for $W \rightarrow e\nu$ + jets and $W \rightarrow \tau\nu$ + jets events. The red and green lines mean the averages in low (< 35) and high (< 35) M_T regions, respectively.

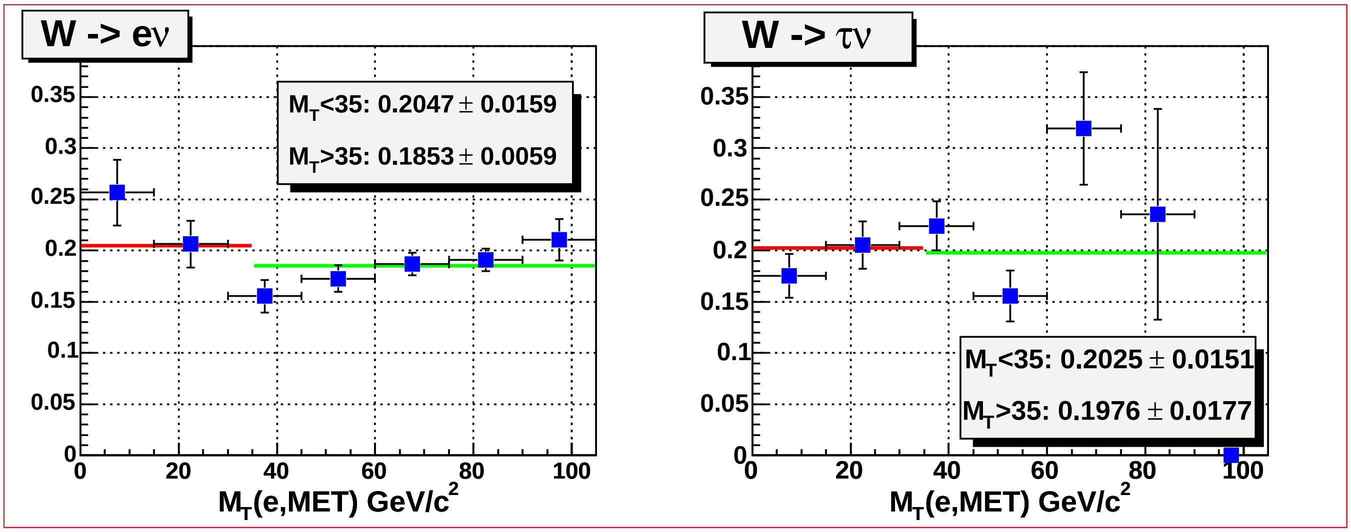

Fig. 7.8. The ratio of $N^{ev}(N_{jet} = 1)/N^{ev}(N_{jet} = 0)$ as a function of M_T for $W \rightarrow e\nu$ + jets and $W \rightarrow \tau\nu$ + jets events. The red and green lines mean the averages in low (< 35) and high (< 35) M_T regions, respectively.

Table 7.22. Summary of backgrounds for the six regions. W+jet background estimation will be performed at the fitting stage and is not included in the total.

Process	Expected Rate for $\mathcal{L} = 196.5$ (178 for CMX) pb^{-1}					
	A	B	A’	B’	C	D
$e+\tau$ Channel						
$Z \to \tau\tau$	2.09 ± 0.52	1.18 ± 0.69	4.59 ± 0.40	1.50 ± 0.23	12.49 ± 0.54	2.87 ± 0.26
$Z \to ee$	0.14 ± 0.10	0.28 ± 0.14	1.60 ± 0.33	0.63 ± 0.21	11.63 ± 0.90	0.63 ± 0.21
QCD	$0.00^{+0.23}_{-0.00}$	$0.25^{+0.37}_{-0.18}$	$0.25^{+0.37}_{-0.18}$	$0.75^{+0.53}_{-0.36}$	$1.75^{+0.75}_{-0.59}$	$0.50^{+0.46}_{-0.28}$
$t\bar{t}$	0.23 ± 0.03	0.99 ± 0.06	0.028 ± 0.010	0.15 ± 0.02	0.	0.004 ± 0.004
WZ	0.026 ± 0.012	0.057 ± 0.017	0.026 ± 0.012	0.062 ± 0.018	0.005 ± 0.005	0.052 ± 0.016
ZZ	0.035 ± 0.006	0.010 ± 0.003	0.008 ± 0.003	0.010 ± 0.003	0.008 ± 0.003	0.020 ± 0.005
WW	0.08 ± 0.04	0.173 ± 0.007	0.078 ± 0.005	0.189 ± 0.007	0.016 ± 0.002	0.126 ± 0.006
W+jet	To be determined in the fit					
Total :	$2.60^{+0.58}_{-0.53}$	$2.94^{+0.80}_{-0.73}$	$6.58^{+0.64}_{-0.55}$	$3.29^{+0.62}_{-0.48}$	$25.90^{+1.29}_{-1.20}$	$4.19^{+0.57}_{-0.43}$
$\mu+\tau$ CMUP Channel						
$Z \to \tau\tau$	1.10 ± 0.19	0.56 ± 0.18	3.07 ± 0.25	0.82 ± 0.13	3.62 ± 0.28	1.33 ± 0.17
$Z \to \mu\mu$	0.	0.30 ± 0.17	0.	0.20 ± 0.14	0.20 ± 0.14	2.32 ± 0.48
QCD	$0.25^{+0.37}_{-0.18}$	$0^{+0.23}_{-0.00}$	$0.75^{+0.53}_{-0.36}$	$0.25^{+0.37}_{-0.18}$	$0^{+0.23}_{-0.00}$	$0.25^{+0.37}_{-0.18}$
$t\bar{t}$	0.14 ± 0.03	0.95 ± 0.08	0.020 ± 0.011	0.078 ± 0.023	0	0
WZ	0.021 ± 0.002	0.008 ± 0.001	0.009 ± 0.001	0.027 ± 0.002	0.005 ± 0.001	0.026 ± 0.003
ZZ	0.021 ± 0.004	0.014 ± 0.003	0.008 ± 0.003	0.023 ± 0.004	0.004 ± 0.002	0.011 ± 0.003
WW	0.003 ± 0.001	0.021 ± 0.002	0.009 ± 0.001	0.095 ± 0.005	0.025 ± 0.002	0.42 ± 0.01
W+jet	To be determined in the fit					
Total:	$1.54^{+0.42}_{-0.26}$	$1.86^{+0.35}_{-0.27}$	$3.87^{+0.59}_{-0.44}$	$1.50^{+0.42}_{-0.26}$	$3.85^{+0.39}_{-0.31}$	$4.36^{+0.63}_{-0.54}$
$\mu+\tau$ CMX Channel						
$Z \to \tau\tau$	0.61 ± 0.15	0.27 ± 0.14	1.47 ± 0.19	0.64 ± 0.12	1.44 ± 0.19	0.55 ± 0.11
$Z \to \mu\mu$	0	0.11 ± 0.11	0	0.11 ± 0.11	0	1.15 ± 0.36
QCD	$0^{+0.23}_{-0.00}$	$0^{+0.23}_{-0.00}$	$0.50^{+0.46}_{-0.28}$	$0^{+0.23}_{-0.00}$	$0.25^{+0.37}_{-0.18}$	$0^{+0.23}_{-0.00}$
$t\bar{t}$	0.052 ± 0.020	0.34 ± 0.05	0.007 ± 0.007	0.022 ± 0.013	0	0.007 ± 0.007
WZ	0.009 ± 0.002	0.004 ± 0.001	0.004 ± 0.001	0.012 ± 0.002	0.001 ± 0.001	0.014 ± 0.002
ZZ	0.006 ± 0.002	0.008 ± 0.003	0.006 ± 0.002	0.007 ± 0.003	0.001 ± 0.001	0.007 ± 0.003
WW	0.001 ± 0.001	0.008 ± 0.001	0.003 ± 0.001	0.041 ± 0.003	0.012 ± 0.002	0.192 ± 0.007
W+jet	To be determined in the fit					
Total:	$0.68^{+0.27}_{-0.15}$	$0.74^{+0.30}_{-0.18}$	$1.99^{+0.50}_{-0.34}$	$0.84^{+0.28}_{-0.17}$	$1.70^{+0.41}_{-0.26}$	$1.92^{+0.45}_{-0.38}$
Total $\mu\tau$:	$2.21^{+0.50}_{-0.30}$	$2.60^{+0.46}_{-0.32}$	$5.58^{+0.77}_{-0.55}$	$2.34^{+0.50}_{-0.31}$	$5.56^{+0.57}_{-0.40}$	$6.28^{+0.77}_{-0.66}$

Table 7.23. Number of events found in each of the six primary (isolated) and complementary (used for QCD background estimation) regions.

Region	$e+\tau$ Channel		$\mu+\tau$ Channel	
	Primary	QCD	Primary	QCD
A	**2**	0	**3**	1
B	3	1	4	0
A'	7	1	5	5
B'	16	3	12	1
C	22	7	5	1
D	37	2	48	1

ID scale factors as well as the trigger simulation, while uncertainty on the luminosity is not included.

7.5 Data

In **Table 7.23** we show the number of events observed in data. The data in region A is shown in bold font to indicate that the box (region A) was not opened until all cuts were finalized and backgrounds were estimated.

7.6 Fit Procedure and Limit Setting

As discussed earlier, out of the four regions, signal is expected to dominate in region A, but its non-negligible part of 30% will find its way into region B. W+jets are primarily occupying region D with some parts of it in regions C and B. All four regions have contributions from other previously discussed backgrounds. We repeat our background estimation calculations to predict the rates of those backgrounds and the results are shown in **Table 7.22**.

We build the likelihood function as follows: we start with full rates of signal and background processes, ν_i in each of the four regions $i = A,\ B,\ C,\ D$ and use Poisson probability to calculate probability of the true rates being within $d\nu_i$ of ν_i given the number of observed events N_i:

$$d\mathcal{P} = \prod_{i=A,B,C,D} P(\nu_i, N_i)d\nu_i, \tag{7.10}$$

where $P(\nu_i, N_i)$ is a simple Poisson distribution function with the expected rate ν_i and the number of observed events N_i.

We introduce fractions ε_i for the signal defined as $\varepsilon_i = \nu_i^s/\nu_A^s$ and account for the fact that each rate is a sum of rates of W, signal and "other" backgrounds (subscripts w, s and b, respectively):

$$\begin{aligned} \nu_A &= \nu_A^b + \nu_A^w + \nu_A^s, \\ \nu_B &= \nu_B^b + \nu_A^w/\nu_C^w \times \nu_D^w \times r + \varepsilon_B \nu_A^s, \\ \nu_C &= \nu_C^b + \nu_C^w + \varepsilon_C \nu_A^s, \\ \nu_D &= \nu_D^b + \nu_D^w + \varepsilon_D \nu_A^s, \end{aligned} \tag{7.11}$$

where $r = f_{BD}^W/f_{AC}^W$, which is 1 if the scaling for W's were exact and is introduced to account for possible deviations from the exact equality.

We then perform a transformation of variables $(\nu_A, \nu_B, \nu_C, \nu_D) \to (\nu_A^w, \nu_C^w, \nu_D^w, \nu_A^s)$. The Jacobian of this transformation is

$$J = (\varepsilon_C r \frac{\nu_A^w \nu_D^w}{(\nu_C^w)^2} - \varepsilon_D r \frac{\nu_A^w}{\nu_C^w} + \varepsilon_B - r \frac{\nu_D^w}{\nu_C^w}) = r \frac{\nu_A^w}{\nu_C^w} (\varepsilon_C \frac{\nu_D^w}{\nu_C^w} - \varepsilon_D) + (\varepsilon_B - r \frac{\nu_D^w}{\nu_C^w}). \tag{7.12}$$

We include existing prior knowledge about the "other" backgrounds and r assuming that those are nuisance parameters and will be integrated out later:

$$\frac{d\mathcal{P}}{d\nu_A^s} = d\nu_A^w d\nu_C^w d\nu_D^w \int_{0.5}^{1.5} dr \prod_{i=A,B,C,D} \int_0^\infty d\nu_i^b exp[-\frac{(\nu_i^b - \nu_{i0}^b)^2}{2\sigma_i^{b2}}] \prod_{i=A,B,C,D} P(\nu_i, N_i) \times J(r) dr. \tag{7.13}$$

Finally, we replace the signal rate in region A with a physically meaningful cross-section using $\nu_A^s = \sigma(\tilde{t}_1 \bar{\tilde{t}}_1) \times L \times \mathcal{B}(\tau\tau \to \tau_l \tau_h) \times \alpha$, where α is the full selection efficiency of signal events for region A and L is the integrated luminosity. We include prior knowledge about the acceptance and its uncertainty and re-write probability function in its final form:

$$\frac{d\mathcal{P}}{d\sigma} = \int d\alpha \times exp[-\frac{\alpha - \alpha_0}{2\sigma_\alpha^2}] \times L \times \mathcal{B} \times \alpha \times \frac{d\mathcal{P}}{d\nu_A^s} \tag{7.14}$$

and define Likelihood as:

$$\mathcal{L}(\sigma) = \frac{d\mathcal{P}}{d\sigma}. \tag{7.15}$$

We integrate over all integration variables in physical region (all processes must have non-negative rates) to obtain the one-dimensional likelihood function as a function of the cross-section. **Figure 7.9** shows the likelihood function obtained using this method for electron and muon channels separately for $M(\tilde{t}_1) = 130$ GeV/c^2. We use 95% C.L. highest posterior density intervals to determine the maximum allowed cross-section value that we report as the final limit. Combined limit is obtained by using the product of two likelihood functions:

$$\mathcal{L}(\sigma) = \mathcal{L}^{e+\tau}(\sigma) \times \mathcal{L}^{\mu+\tau}(\sigma). \tag{7.16}$$

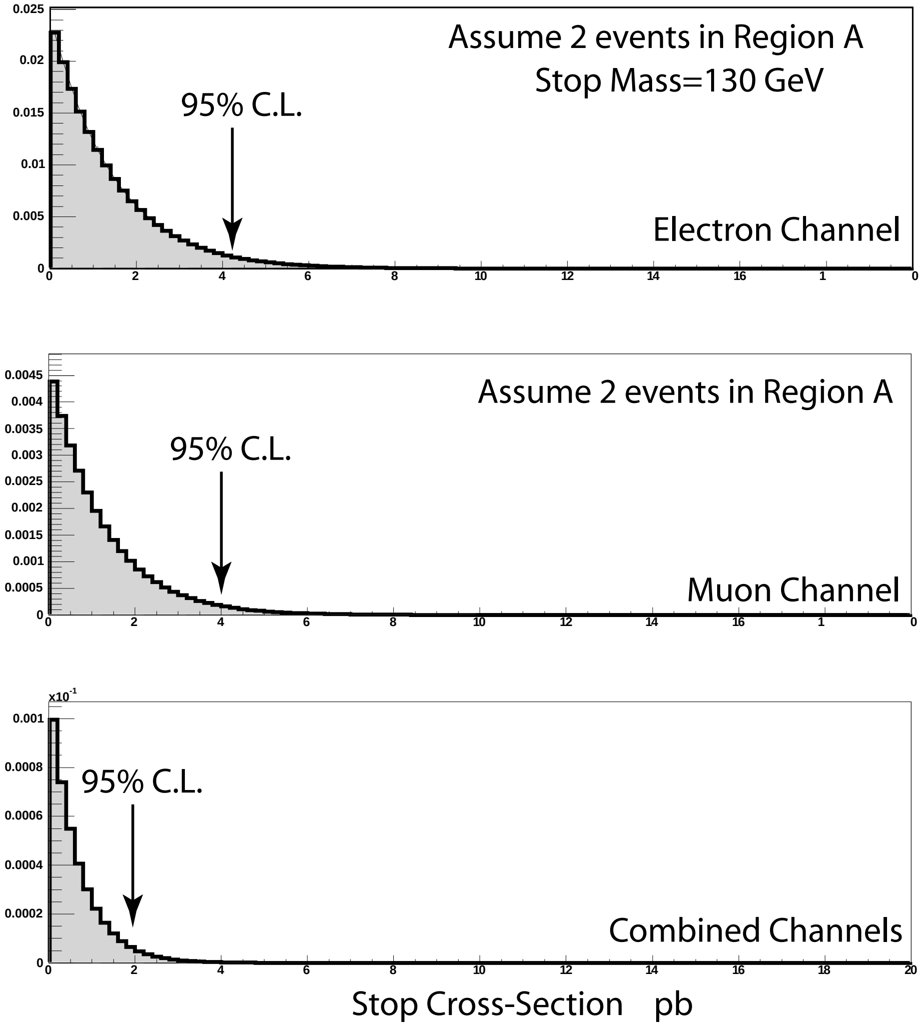

Fig. 7.9. Probability density function (ProbDF) of the $\tilde{t}_1\bar{\tilde{t}}_1$ production cross-section obtained from electron channel data (top), muon channel data (middle), and for both channels combined (bottom). Plots are obtained in assumption that 1 event will be found in each of the channels and using $M(\tilde{t}_1) = 130$ GeV/c^2.

7.6.1 Handling of Systematic Uncertainties in the Fit

We have to take into account not only the fact that possible systematic effects affect the overall rate of events passing our selections, but also how the events are distributed among the four regions. One example is the jet scale uncertainty: when the scale is moved up from its central value, passing events will on average have more jets and therefore one can expect a migration of the events from the bins with lower number of jets to bins with higher number of jets. To handle these effects, we first define a 3×2 matrix A_{ij}, where i runs over three n_{jet} bins and j runs over two bins in M_T, with each value being the expected acceptance in a corresponding bin. For deviated cases, we re-calculate this matrix and call it A'. We then introduce a parameter α associated with a particular kind of uncertainty and use linearized approximation for $A(\alpha)$ as:

$$A_{ij}(\alpha) = A_{ij} + \alpha \times (A'_{ij} - A_{ij}). \tag{7.17}$$

We then choose an appropriate prior ProbDF for each case, treat corresponding α's as nuisance parameters and integrate them out. We call this a *matrix* method, as opposed to *number* method, when we assume that the systematics does not cause noticeable migration between bins.

In addition, some of the uncertainties, e.g. luminosity or tau ID, are correlated between electron and muon channels. Each of these uncertainties is treated separately assuming 100% correlation between the electron and muon channels. In **Table 7.24**, we give a short summary of the assumptions used in fitting. To simplify calculations, we separately combine all fully uncorrelated *number*-type uncertainties into one including the uncertainty due to limited MC statistics.

Note that many of the uncertainties discussed also affect MC-based background estimations. We parameterize the changes in the backgrounds in the same way as we do for the signal acceptance, e.g. expected number of background events coming from MC is scaled with luminosity by assuming 100% correlation between channels and between signal and MC-based

Table 7.24. Handling of systematic uncertainties in the fit.

Type	Method	Prior ProbDF(α)	Degree of Correlation
Jet Scale	matrix	gauss	100%
$\not\!\!E_T$	matrix	1 if $0 < \alpha < 1$, else 0	100%
PDF	number	gauss	100%
τ ID	number	gauss	100%
ISR	number	gauss	100%
FSR	number	gauss	100%
Luminosity	number	gauss	100%
α	number	gauss	0%
$e(\mu)$ ID	number	gauss	0%
stat. error	number	gauss	0%

backgrounds. We account for effects of background migration between regions due to jet energy scale and $\not\!\!E_T$ variations in the same way as for the signal MC and preserve a 100% correlation between channels and between signal and background acceptance estimations.

7.6.2 Final Likelihood for Combined Channels

We finally use the likelihood as in Eqs.(7.16) and (7.14) with σ_α defined as a sum in quadratures of uncorrelated systematic uncertainties and statistical uncertainty due to limited MC statistics (last group in **Table 7.24**).

To account for systematic effects correlated between channels and for possible systematic shifts, we adjust α_0 in the likelihood:

$$\alpha_0^e = \alpha_0^e \times (1 + \sum x_i \times \sigma_i^e) \ ,$$
$$\alpha_0^\mu = \alpha_0^\mu \times (1 + \sum x_i \times \sigma_i^\mu) \ , \tag{7.18}$$

where i runs over all systematic types, σ_i is the size of the systematic uncertainty of type i, and x_i are corresponding eigenvectors. We accordingly correct fractions ε_B, ε_C and ε_D. We then re-write Eq.(7.16) as

$$\mathcal{L}(\sigma) = \int f(\vec{x}) d\vec{x} \mathcal{L}^{e+\tau}(\sigma, \vec{x}) \times \mathcal{L}^{\mu+\tau}(\sigma, \vec{x}) \ , \tag{7.19}$$

where $f(\vec{x})$ is assumed to be a ProbDF for $\vec{x}$ and is a product of individual ProbDFs (most of which are simple gauss functions, except for the $\not\!\!E_T$ case, where a θ-function is assumed). This simple procedure provides desired values of correlations between the two channels.

7.7 Procedure Validation

We perform several cross-checks to verify the integrity of the fitting method and to validate the procedure in the control regions.

7.7.1 Fit Validation

To show that the fitting routine produces expected results, we perform the following check: for each of the four regions, we sum up the rates for "known" backgrounds with the expected number of W events in each region as predicted by MC. We then calculate the expected number of stop events in each of the regions assuming that stop production exists with some cross-section and add it to the sum. We round up the expected rate to represent the observed number of data events and apply our standard fit procedure. The result of this pseudo-experiment for the case of a 130 GeV stop with a cross-section of 10 pb with the fit applied to the muon channel only is illustrated in **Fig. 7.10**. It shows the output ProbDF as a function of the stop cross-section and it is clearly in good agreement with the 10 pb expectation.

7.7.2 Cross-Check: $Z \to \tau\tau$ Control Region

We define a $Z \to \tau\tau$ control region by tightening transverse mass cut to $M_T(\ell, \not\!\!E_T) < 25$ GeV/c^2 and replacing the cut on Y_T with a cut on a vector sum of transverse momenta of the lepton and $\not\!\!E_T$, $p_T > 25$ GeV/c, defined as

$$p_T(e, \not\!\!E_T) \equiv |\vec{p}_T^{\,\ell} + \vec{\not\!\!E}_T|. \tag{7.20}$$

We compare MC predictions to the data and find good agreement between the two. QCD background was estimated in a standard way, W+jet background was ignored due to its small

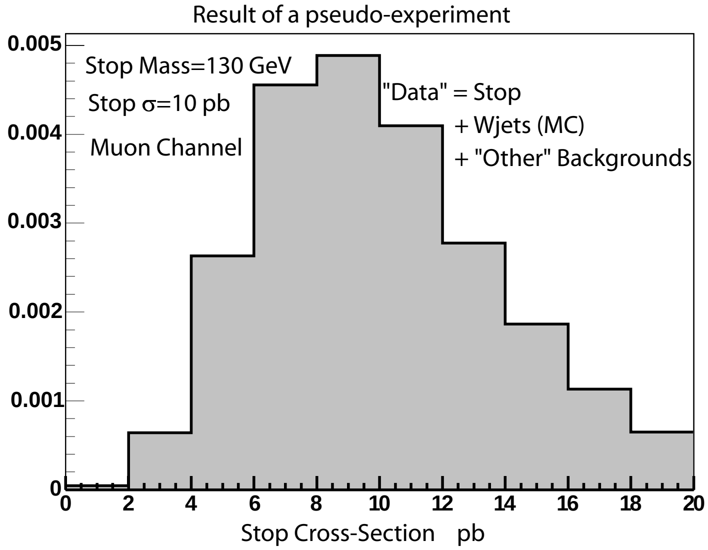

Fig. 7.10. ProbDF for the stop cross-section obtained using the standard fit method for data obtained in a pseudo-experiment, in which the stop has a mass of 130 GeV/c^2 with a production cross-section of 10 pb, rate of the W+jet background events is obtained using MC and other backgrounds are the same as in the real analysis. Fit is applied to muon data only. ProbDF obtained is consistent with the reference cross-section.

contribution. **Figure 7.11** shows the distribution of the number of tracks in the final tau candidates in the muon channel.

7.7.3 Control Regions $N_{jet} = 0$ and $N_{jet} = 1$

If one takes into account the current lower limit on the stop mass (122 GeV/c^2), the expectation for the stop events in the region of $N_{jet} = 1$ is absolutely negligible and therefore it can also serve as a control region. It is obvious that the W+jets background is negligible in regions A' and C, and the agreement between data and expected backgrounds is good, see **Fig. 7.12** for electron and muon channels separately, and **Fig. 7.13** for the combined plot. However, we still can use our standard fitting procedure to estimate "signal" rate (in events, not in pb) in region A' using as input the number of events in B' and in the $N_{jet} = 0$ bins. We expect no signal events and the fit returns a PorbDF in agreement with expectation of no signal events in that region[7].

---

[7] As expected in this case, due to a relatively large expected number of background events in "signal" region A', the ProbDF is quite wide and only provides a very imprecise confirmation that no large fluctuations happened in the region in question.

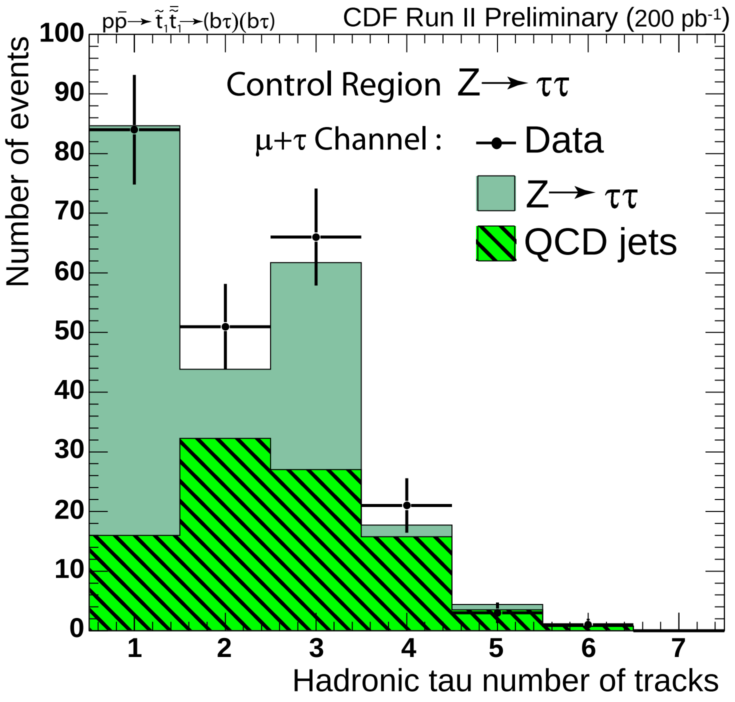

Fig. 7.11. Distribution of the number of prongs in the final tau candidates for $Z \to \tau_\mu \tau_h$.

7.8 Cross Section Limit with 200 pb^{-1} Data

7.8.1 Limit

We calculate 95% C.L. upper limits on the cross-section of the stop pair production as a function of stop mass, see **Table 7.25**. The band in **Fig. 7.14** shows the expected limit in case of no discovery for combined analysis of electron and muon channels and corresponds to the 68% probability range of possible limits obtained by assuming that the observed number of events follows the background expectation. Actual limit on the cross-section was set based on five observed events (3 events in the muon channel and 2 events in the electron channel) overlaid with the theoretical stop cross-section using CTEQ6M PDF set shown as a solid line, while dashed lines indicate the theoretical uncertainty in the cross-section calculation due to renormalization and factorization scales and PDF. Also shown are previously existing limits on stop mass (or, which is equivalent, on the third generation scalar leptoquark, $\tilde{S}_0$ or S_1, mass.

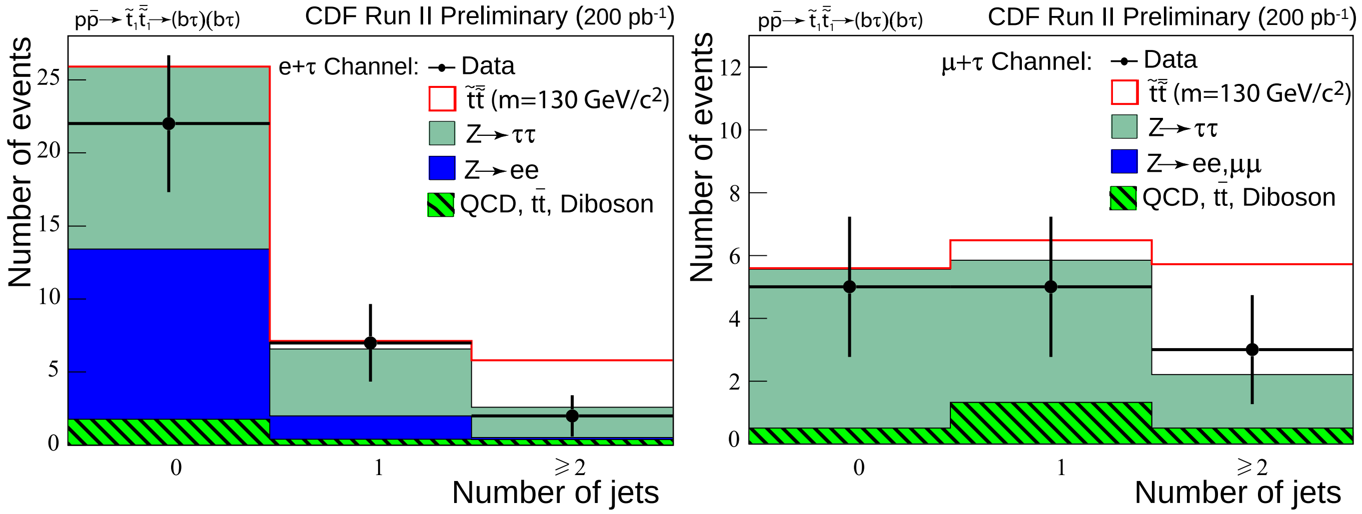

(a) (b)

Fig. 7.12. Distribution of the number of jets in the final candidate events for $M_T > 35$ GeV$/c^2$ region for (a) electron channel and (b) muon channel.

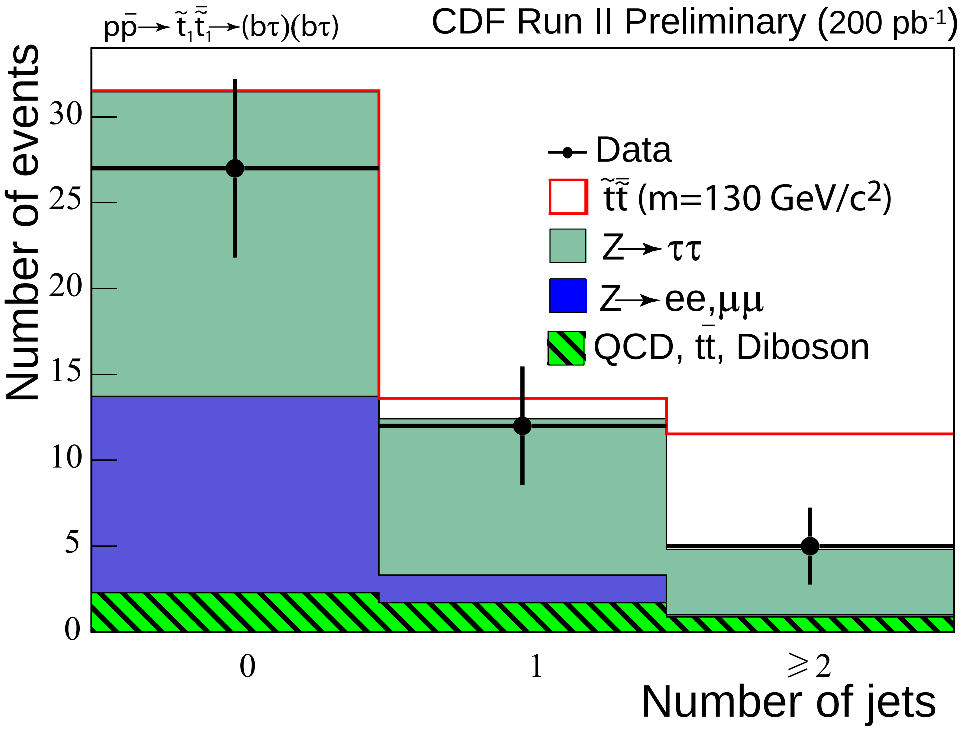

Fig. 7.13. Distribution of the number of jets in the final candidate events for $M_T > 35$ GeV$/c^2$ region for electron channel and muon channel combined.

Table 7.25. 95% C.L. upper limit on the $\tilde{t}_1\bar{\tilde{t}}_1$ production cross-section (in pb) as a function of stop mass.

		$\tilde{t}_1\tilde{t}_1 \to b\bar{b}\tau\tau$ $[M(\tilde{t}_1)$, GeV$/c^2]$						
$N_{evt}^{e+\tau}$	$N_{evt}^{\mu+\tau}$	100	110	120	130	140	150	160
2	3	6.75	4.75	3.75	3.05	2.75	2.65	2.35

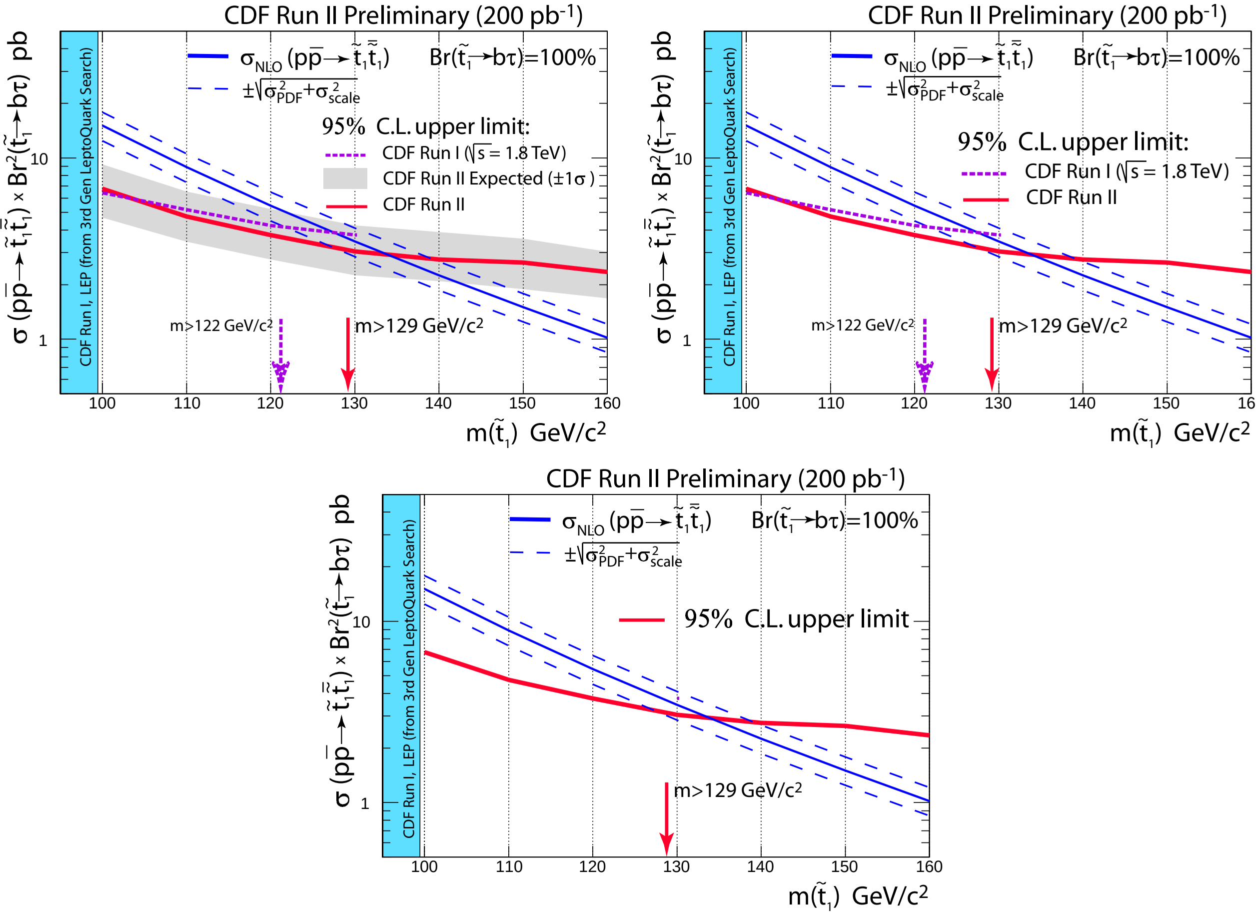

Fig. 7.14. Theoretical predictions for the $\tilde{t}_1\bar{\tilde{t}}_1$ production cross-section (blue solid lines) and its uncertainty due to factorization and normalization scales combined with the PDF error (blue dashed lines). Projected 95% C.L. upper limit for the $\tilde{t}_1\bar{\tilde{t}}_1$ production cross-section obtained from combined electron and muon channel data is shown as a band (corresponds to a 68% probability range of possible limit if data were to follow background expectation). Red solid lines show the 95% C.L. limits obtained in this analysis. Earlier constraint obtained from CDF and LEP leptoquark searches ($M(\tilde{t}_1) > 99$ GeV$/c^2$) is shown as a box, a limit obtained in a similar Run I stop search analysis ($M(\tilde{t}_1) > 122$ GeV$/c^2$) is shown as a dashed line (violet).

Table 7.26. 95% C.L. upper limits on the $\tilde{t}_1\bar{\tilde{t}}_1$ production cross-section (in pb) as a function of stop mass in the case of theoretical uncertainties on the cross-section convoluted into the fit. Note that this should not be interpreted as the upper limit on the cross section and only used to estimate a conservative limit on the stop mass.

		$\tilde{t}_1\bar{\tilde{t}}_1 \to b\bar{b}\tau\tau$ [$M(\tilde{t}_1)$, GeV/c^2]				
$N_{evt}^{e+\tau}$	$N_{evt}^{\mu+\tau}$	100	110	120	130	140
2	3	6.42	5.17	4.35	3.55	3.05

7.8.2 Stop Mass Limit

Setting a conservative mass limit requires accounting for theoretical uncertainties in the calculation of the stop production cross-section. These uncertainties include dependence of the cross-section on the renormalization and factorization scale as well as dependence on PDFs. We found that uncertainties owing to the scale (obtained by varying the scale from its default value to a double and a half of that) and the choice of a PDF are similar and are about 10-12% each. It was somewhat unexpected that PDF uncertainties are that large, e.g. it was estimated to be much smaller in comparison with Run I analyses, and we traced them to eigenvectors 5 and 15 in the CTEQ6.1 counting scheme. Eigenvector 15 is primarily associated with the high-x gluon component, which is rather poorly constrained. We combine the two theoretical uncertainties into a single number by summing them in quadratures to obtain an additional 18% systematic uncertainty on the theoretical cross-section. This error is convoluted into the fitting procedure and results of calculation of the upper limit that include theoretical error are shown in **Table 7.26**. These were used to calculate the mass limit by finding an intersection of the limit curve with the default cross-section line. We arrived at a mass limit of $M(\tilde{t}_1) > 129$ GeV/c^2.

7.8.3 Third Generation Scalar Leptoquark Mass Limit

The stop pair production process is very similar to the pair production of the third generation scalar leptoquark (LQ_3). The cross sections become identical in the limit of high gluino

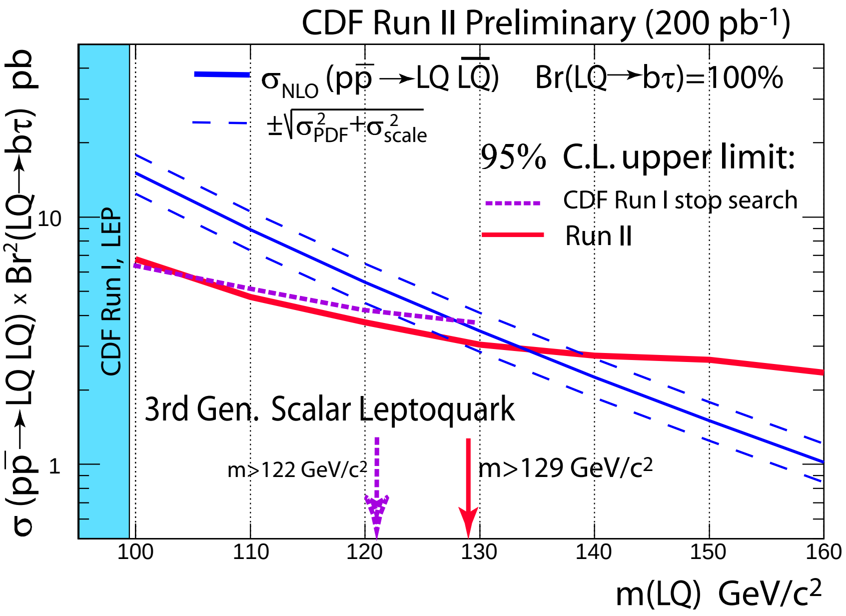

Fig. 7.15. Theoretical prediction for the third generation scalar leptoquark pair production cross-section (blue solid line) and its uncertainty due to factorization and normalization scales combined with the PDF error (dashed lines). Projected 95% C.L. upper limit for the leptoquark production cross-section obtained from combined electron and muon channel data is shown as a band (corresponds to a 68% probability range of possible limit if data were to follow background expectation). Red solid line shows the 95% C.L. limit obtained in this analysis. Earlier constraint obtained from CDF and LEP leptoquark searches ($m(LQ_3) > 99$ GeV/c^2) is shown as a box. In all cases we assume the branching ratio $LQ_3 \to \tau b = 100\%$.

mass, which is usually so assumed. **Figure 7.15** shows theoretical prediction for the LQ_3 production cross-section, which is identical to the prediction for the stop pair (**Fig. 7.14**).

7.8.4 Kinematical Distributions For Signal Region

Here we present a set of the signal region distributions for combined electron and muon channels. **Figure 7.16** presents the distributions for Y_T and M_T. **Figure 7.17** shows invariant mass of lepton and tau and $\not{E}_T$ distributions. Lepton P_T (E_T was used for electrons) and tau visible transverse momentum P_T^{vis} are shown in **Fig. 7.18**. E_T^{corr} for the leading (having the biggest E_T^{corr}) and second jets are given in **Fig. 7.19**.

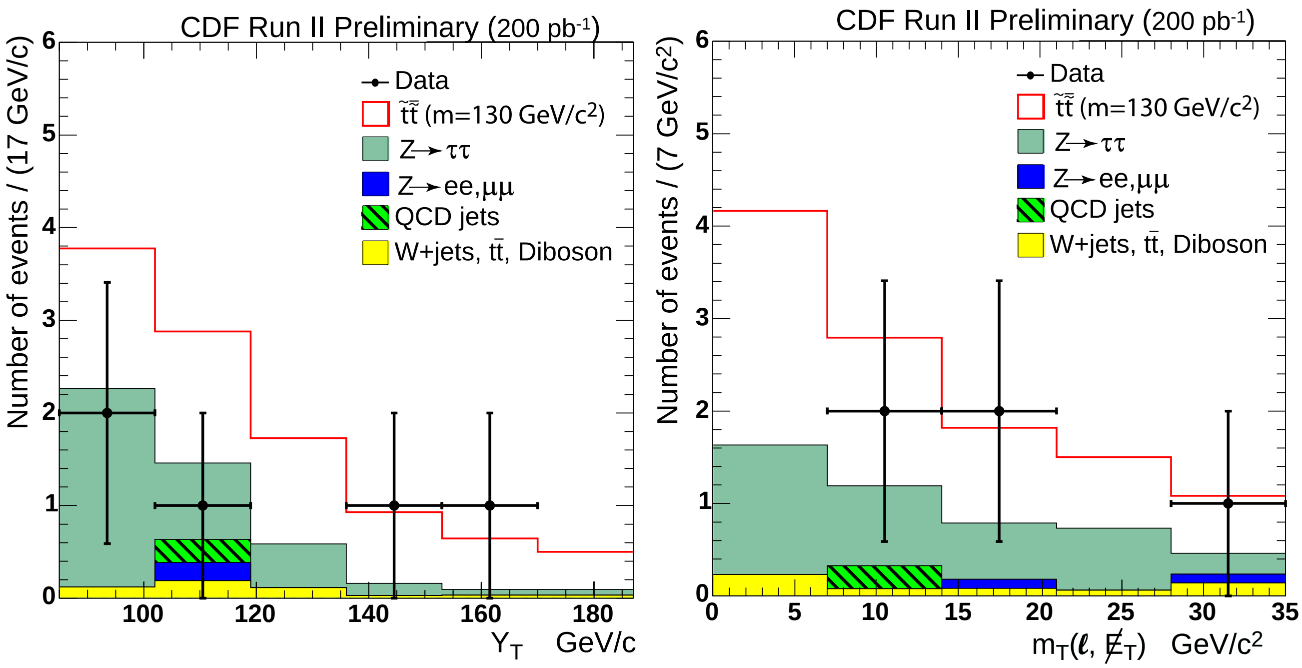

Fig. 7.16. Distributions for Y_T and M_T for combined electron and muon channels in region A.

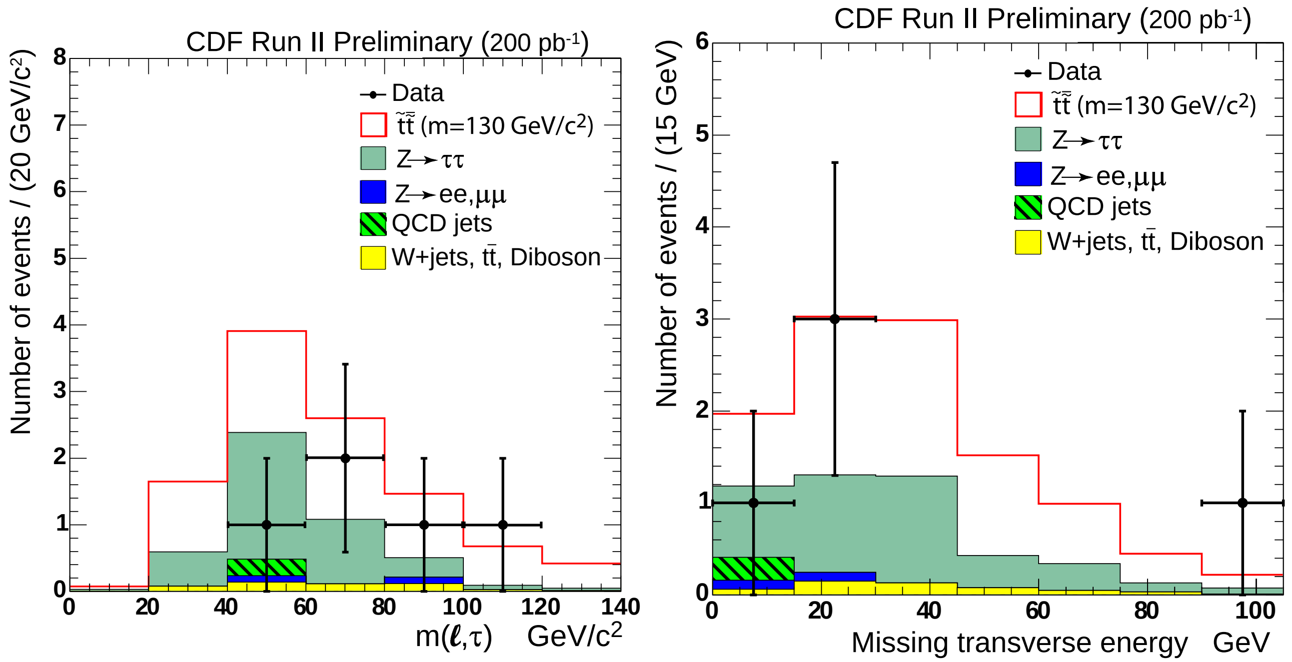

Fig. 7.17. Distributions for the invariant mass of the two tau candidates $M(\tau_l, \tau_h)$ and missing transverse energy for combined electron and muon channels in region A.

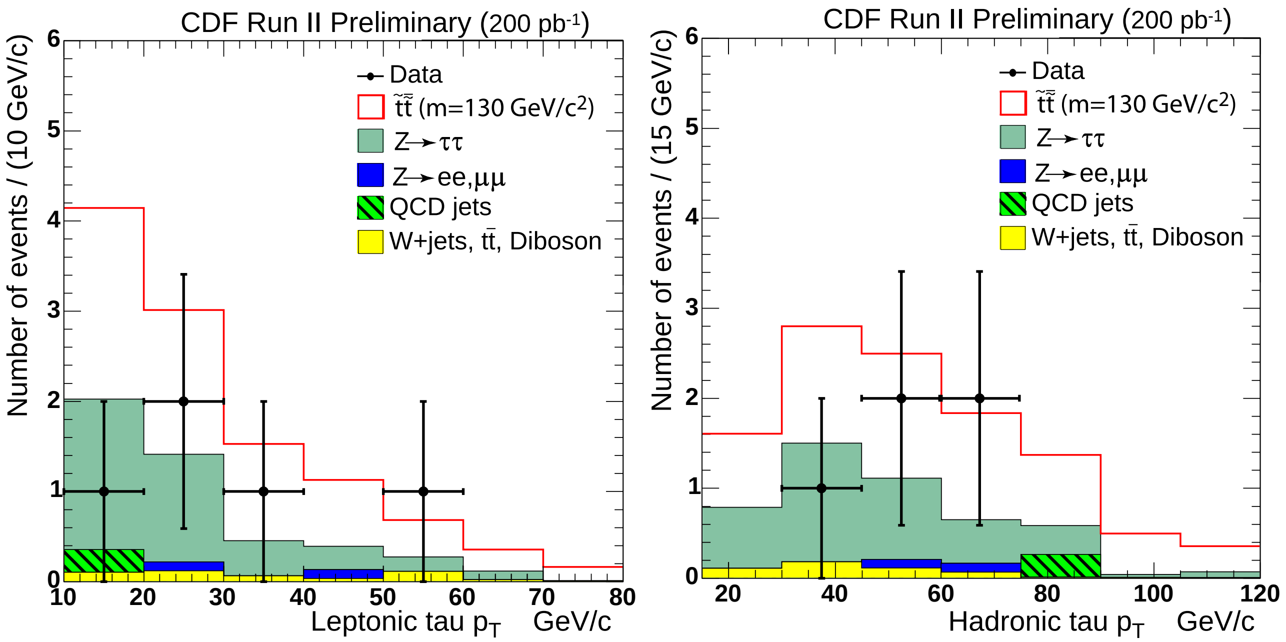

Fig. 7.18. Distributions for lepton P_T and tau P_T^{vis} for combined electron and muon channels in region A.

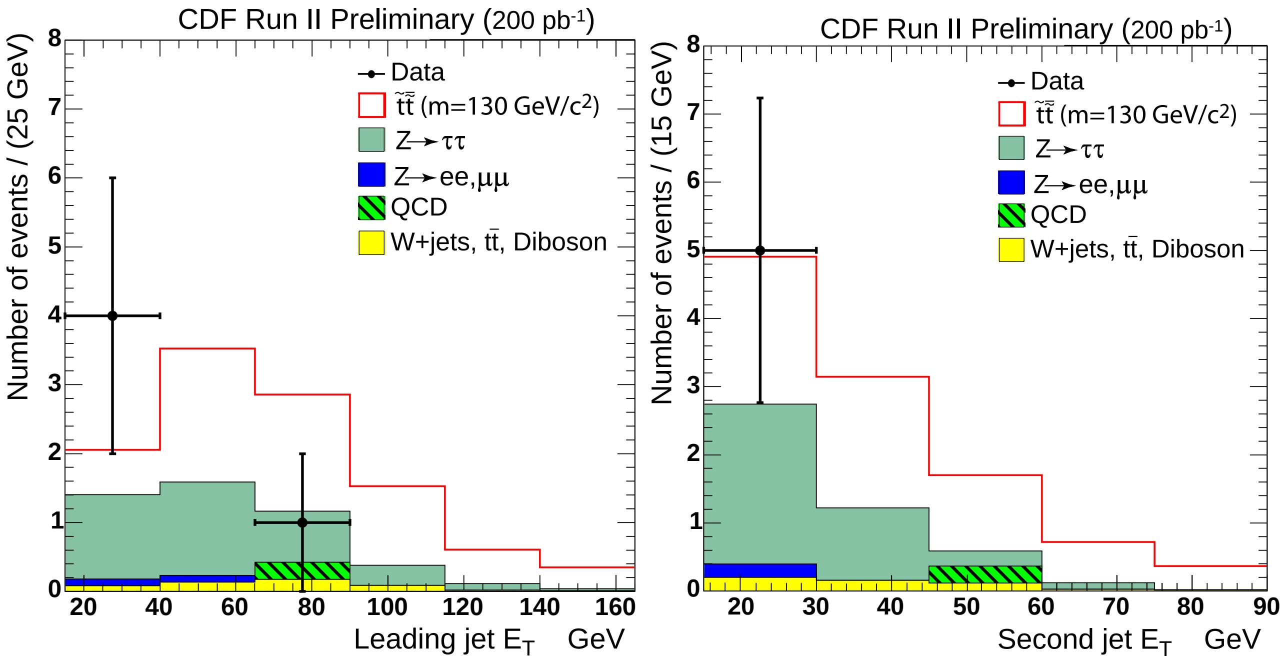

Fig. 7.19. Distributions for leading jet E_T^{corr} and second jet E_T^{corr} for combined electron and muon channels in region A.

7.9 Conclusions

We have performed a search for SUSY stop quark pair production. The number of events found is in agreement with the expectations based on the background studies. With no excess found over SM, we set a final stop mass limit using 200 pb^{-1} of Run II data: (i) for the default cross-section prediction, the lower mass limit is 134 GeV/c^2; (ii) convolution of theoretical uncertainties owing to renormalization and factorization scales and existing flexibility in PDF leads to a limit of $M(\tilde{t}_1) > 129$ GeV/c^2.

Chapter 8

Summary

We have searched for the scalar top quark pair production in the scenario with R-parity violation. The supersymmetric theory defines the quantum number called R-parity which distinguishes particles in standard model from supersymmetric particles. A scalar top quark (stop) can decay via $\not{R}_p$-violating supersymmetric coupling into tau lepton and b-quark in this scenario. The final states for the analysis include two tau leptons, one lepton from $\tau \to \ell\nu_\ell\nu_\tau$ and the other decaying hadronically, and two or more jets. To collect such events which contain multiple taus in the final states, a new tau trigger (the lepton plus track trigger) is installed in Run II experiment. The lepton plus track trigger allows a lower threshold for lepton momentum (8 GeV/c), keeping physical events for analysis at reasonable rate (~45 nb) in the condition of high luminosity produced by Tevatron Run II. This trigger system prove good performance and have been working well at present. There are many physical topics which can be explored by data taken the lepton plus track trigger.

The data used in stop search correspond to total integrated luminosity of 200 pb^{-1} and was taken from March 2002 to September 2003 collected with the Collider Detector at Fermilab. We find no excess from the Standard Model prediction. As the result, we set the mass limit of 134 GeV/c^2 at 95% confidence level assuming that a stop decays 100% to b and τ. CTEQ6M which is the library of Parton Distribution Function and $Q^2 = \sqrt{M_{\tilde{t}_1}^2 + p_T^2}$ as the QCD parameters of renormalization/fragmentation are used. This limit improves the previous limit of 122 GeV/c^2

by the CDF Run I analysis. The mass limit can also be applied for the third generation scalar leptoquark (S_0 and $\tilde{S}_1$, charge $-4/3$).

Bibliography

[1] M. E. Peskin, "Beyond the standard model," (1997).

[2] Q. Shafi and Z. Tavartkiladze, "Flavor problem, proton decay and neutrino oscillations in susy models with anomalous $\mathcal{U}(1)$," hep-ph/9911264 (1999).

[3] H. Baer and M. Brhlik, "Cosmological relic density from minimal supergravity with implecations for collider physics," *Phys. Rev.* **D53**:597, (1996).

[4] W. Porod, "Phenomenology of stops, sbottoms, staus and tau-sneutrino," hep-ph/9804208 (1998).

[5] S. P. Martin, "A Supersymmetry Primer," hep-ph/9709356 (1997).

[6] For examples, see C. S. Aulah and R.N. Mohapatra, *Phys. Lett.* **B119**:316 (1982); F. Zwirner, *ibid.* **B132**:103 (1983); R. Barbieri and A. Masiero, *Nucl. Phys.* **B267**:679 (1986); S. Dimopoulos and L. J. Hall, *Phys. Lett.* **B196** 135 (1987); *ibid.* **B207**:210 (1987); L. Hall, *Mod. Phys. Lett.* **A5**:467 (1990).

[7] L. J. Hall and M. Suzuki, "Explicit R-parity breaking in supersymmetric models," *Nucl. Phys.* **B231**:419 (1984).

[8] S. Dawson, "R-parity breaking in supersymmetric theories," *Nucl. Phys.* **B261**:297, (1985).

[9] H1 Collaboration, C. Adloff *et al.*, hep-ex/9702012 (1997); ZEUS Collaboration, Breitweg *et al.*, " hep-ex/9702015 (1997).

[10] E. Perez, Y. Sirois, and H. Dreiner, hep-ph/9703444 (1997); D. Choudhury and S. Raychaudhuri, hep-ph/9702392 (1997); G. Altarelli *et al.*, hep-ph/9703276 (1997); H. Dreiner and P. Morawitz, hep-ph/9703279 (1997); J. Kalinowski *et al.*, hep-ph/9703288 (1997); D. Choudhury and S. Raychaudhuri, hep-ph/9703369 (1997).

[11] J. C. Romão and J. W. F. Valle. "Neutrino masses in supersymmetry with spontaneously broken R-parity," *Nucl. Phys.* **B381**:87 (1992).

[12] S. Olsen. *Plenary talk at the 8th DPF meeting, Albuquerque, NM, Aug. 1994.*

[13] C. Kao, H. Baer, and X. Tata, "Impact of R-Parity Violation on Supersymmetry Searches at the Tevatron," hep-ph/9410283 (1994).

[14] G. F. Giudice, V. Barger, and T. Han, "Some new aspects of supersymmetry R-parity violating interactions," *Phys. Rev.* **D40**:2987 (1989).

[15] Particle Data Group, *Phys. Rev.* **D54**:1 (1996).

[16] R. M. Godbole, P. Roy, and X. Tata, *Nucl. Phys.* **B401**:67 (1993); A. I. Belesev *et al.*, *Phys. Lett.* **B350**:263 (1995); C. Weinheimer *et al.*, *ibid.* **B300**:210 (1993).

[17] R. Mohapatra, *Phys. Rev.* **D34**:3457 (1986); J. D. Vergados, *Phys. Lett.* **B184**:55 (1987); M. Hirsch, H. V. Klapdor-Kleingrothaus, and S. G. Kovalenko, *ibid.* **B352**:1 (1995); *Phys. Rev. Lett.* **75**:17 (1995); *Phys. Rev.* **D53**:1329 (1996).

[18] S. Davidson, D. Bailey, and B. A. Campbell, *Z. Phys.* **C61**:613 (1994); C. S. Wood *et al.*, *Science* **275**:1759 (1997); W. J. Marciano and J.L. Rosner, *Phys. Rev. Lett.* **65**:2963 (1990), erratum **68**:898 (1992).

[19] H. Dreiner, "An Introduction to Explicit R-Parity Violation," hep-ph/9707435 (1997).

[20] R. Gupta, T. Bhattacharya, and S. R. Sharpe, "Matrix elements of four-fermion operators with quenched Wilson fermions," *Phys. Rev.* **D55**:4036 (1996).

[21] G. Bhattacharyya, J. Ellis, and K. Sridhar, *Mod. Phys. Lett.* **A10**:1583 (1995); G. Bhattacharyya, D. Choudhury, and K. Sridhar, *Phys. Lett.* **B355**:193 (1995); J. Ellis, S. Lola, and K. Sridhar, hep-ph/9705416, (1997).

[22] G. Bhattacharyya, *Nucl. Phys. Proc. Suppl.* **52A**:83 (1997).

[23] G. Bhattacharyya and D. Choudhury, *Mod. Phys. Lett. A* **10**:1699 (1995).

[24] F. Zwirner, "Observable $\Delta B = 2$ transitions without nucleon decay in a minimal supersymmetric extension of the standard model," *Phys. Lett.* **B132**:103 (1983).

[25] J. L. Goity and M. Sher, "Bounds on $\Delta B = 1$ couplings in the supersymmetric standard model," *Phys. Lett.* **B346**:69 (1995).

[26] B. de Carlos and P. L. White, "R-parity violation effects through soft supersymmetry-breaking terms and the renormalization group," *Phys. Rev.* **D54**:3427 (1996).

[27] A. Y. Smirnov and F. Vissani, "Upper bound on all products of R-parity violating couplings λ' and λ'' from proton decay ," *Phys. Lett.* **B380**:317 (1996).

[28] L. M. Krauss and F. Wilczek, *Phys. Rev. Lett.* **62**:1221 (1989); T. Banks, *Nucl. Phys.* **B323**:90 (1989).

[29] L. E. Ibanez and G. G. Ross, *Phys. Lett.* **B260**:291 (1991); *Nucl. Phys.* **B368**:3 (1992); T. Banks and M. Dine, *Phys. Rev.* **D45**:1424 (1992).

[30] G. F. Giudice and R. Rattazzi, "R-Parity Violation and Unification," hep-ph/9704339 (1997).

[31] M. C. Bento, L. Hall, and G. G. Ross, *Nucl. Phys.* **B292**:400 (1987); N. Ganoulis, G. Lazarides, and Q. Shafi, *ibid.* **B323**:374 (1989).

[32] H. Dreiner and G. G. Ross, "Sphaleron erasure of primordial baryogenesis," *Nucl. Phys.* **B410**:183 (1993).

[33] W. Beenakker *et al.*, "PROSPINO: A program for the production of sumersymmetric particles in next-to-leading order QCD," hep-ph/9611232 (1996).

[34] J. Pumplin *et al.*, "New generation of parton distributions with uncertainties from global QCD analysis," hep-ph/0201195 (2002).

[35] D. Stump *et al.*, "Inclusive jet production, parton distributions, and the search for new physics," hep-ph/0303013 (2003).

[36] M. Guchait, A. Datta, and K. K. Jeong, "Stop squark search at tevatron in the light slepton scenario," hep-ph/9903214 (1999).

[37] K. Hikasa and M. Kobayashi, "Light scalar top quark at e^+e^- colliders," *Phys. Rev.* **D36**:724 (1987).

[38] W. Podod, "More on higher order decays of the lighter top squark," *Phys. Rev.* **D59**:095009 (1999).

[39] Y. Mambrini and A. Djouadi, "Three-body decays of top and bottom squarks," hep-ph/00011364 (2000).

[40] J. W. F. Valle, M. A. Diaz, and D. A. Restrepo, "Three-body decays of the lightest stop in minimal supergravity with and without R-parity," hep-ph/9908286 (1999).

[41] J. W. F. Valle, W. Porod, and D. A. Restrepo, "Light stop: MSSM versus R-parity violation," hep-ph/0001033 (2000).

[42] V. Barger *et al.*, "Report of the SUGRA working group for Run II of the tevatron," hep-ph/0003154 (2000).

[43] R. Culbertson *et al.*, "Low-scale and gauge-mediated supersymmetry breaking at the Fermilab Tevatron Run II," hep-ph/0008070 (2000).

[44] S. Ambrosanio *et al.*, "Report of the beyond the MSSM subgroup for the Tevatron Run II SUSY/Higgs workshop," hep-ph/0006162 (2000).

[45] M. Carena *et al.*, "Report of the Higgs working group of the Tevatron Run 2 SUSY/Higgs workshop," hep-ph/0010338 (2001).

[46] M. Chertok *et al.*, "Lepton + track trigger for Run II: A new approach for triggering on dileptons -electron case-," *CDF Note* 4807.

[47] J. Done *et al.*, "Lepton + track trigger for Run II: A new approach for triggering on dilepton -muon case-," *CDF Note* 5157.

[48] M. Albrow *et al.*, "Run-II trigger table and datasets plan," *CDF Note* 4718.

[49] CDF Collaboration, F. Abe *et al.*, "Search for chargino-neutralino associated production at the Fermilab Tevatron collider," *Phys. Lett.* **80**:5275 (1998); Also see *CDF Note* 4371.

[50] M. P. Giordani *et al.*, "Dilepton triggers for exotic searches at CDF II," *CDF Note* 6074.

[51] CDF Collaboration, F. Abe *et al.*, "Observation of Top Quark Production in $p - \bar{p}$ Collisions with the Collider Detector at Fermilab," *Phys. Lett.* **74**:2626 (1995).

[52] D0 Collaboration, S. Abachi *et al.*, "Observation of the Top Quark," *Phys. Lett.* **74**:2632 (1995).

[53] For reviews of the MSSM and supergravity, see H. P. Nilles, *Phys. Rep.* **110**:1 (1984); P. Nath, R. Arnowitt, and A. Chamseddine, "Applied $N = 1$ Supergravity," ICTP Series in Theoretical Physics Vol. I, World Scientific, Singapore (1984); H. Haber and G. Kane, *Phys. Rep.* **117**; X. Tata, "The Standard Model and Beyond," edited by J. E. Kim, World Scientific, Singapore, 304 (1991).

[54] CDF Collaboration, T. Affolder *et al.*, "Search for the supersymmetric partner of the top quark in $p\bar{p}$ collisions at $\sqrt{s} = 1.8$ TeV," *Phys. Rev.* **D63**:091101 (2001).

[55] J. C. Romão, M. A. Dí az, and J. W. F. Valle, "Minimal supergravity with R-parity breaking," *Nucl. Phys.* **B524**:23 (1998).

[56] M. A. Dí az, hep-ph/9711435, hep-ph/9712213 (1997); J. C. Romão, hep-ph/9712362 (1997); J. W. F. Valle, talk at PASCOS 98, hep-ph/9808292 (1998).

[57] F. de Campos, M. A. García-Jareño, A. S. Joshipura, J. Rosiek, and J. W. F. Valle, *Nucl. Phys.* **B451**:3 (1995); A. Akeroyd, M. A. Díaz, J. Ferrandis, M. A. García-Jareño, and J. W. F. Valle, *Nucl. Phys.* **B529**:3 (1998).

[58] A. S. Joshipura, and M. Nowakowski, *Phys. Rev.* **D51**:2421 (1995); T. Banks, Y. Grossman, E. Nardi, and Y. Nir, *Phys. Rev.* **D52**:5319 (1995); F. Vissani and A. Yu. Smirnov, *Nucl. Phys.* **B460**:37 (1996); R. Hempfling, *Nucl. Phys.* **B478**:3 (1996); F. M. Borzumati, Y. Grossman, E. Nardi, and Y. Nir, *Phys. Lett.* **B384**:123 (1996); H. P. Nilles and N. Polonsky, *Nucl. Phys.* **B484**:33 (1997); B. de Carlos and P. L. White, *Phys. Rev. D* **55**:4222 (1997); E. Nardi, *Phys. Rev.***D55**:5772 (1997); S. Roy and B. Mukhopadhyaya, *Phys. Rev.* **D55**:7020 (1997); A. Faesiter, S. Kovalenko, and F. Simkovic, *Phys. Rev.* **D58**:055004 (1998); M. Carena, S. Pokorski, and C. E. M. Wagner, *Phys. Lett.* **B430**:281 (1998); M. E. Gómez and K. Tamvakis, *Phys. Rev.* **D58**:057701 (1998).

[59] A. Masiero and J. W. F. Valle, *Phys. Lett.* **B251**:273 (1990); J. C. Romão, A. Ioannissyan, and J. W. F. Valle, *Phys. Rev.* **D55**:427 (1997).

[60] C. Pagliarone *et al.*, "Motivations for searching a lepton flavor violating higgs decay $h \to \mu\tau$," *CDF Note* 5778.

[61] C. Pagliarone, U. Cotti, L. Diaz-Cruz, and E. Vataga, "Search for the lepton flavor violating higgs decay $h \to \tau\mu$ at hadron colliders," *Proc. of the APS/DPF/DPB Summer Study on the Future of Particle Physics (Snowmass 2001)* ed. N. Graf, eConf **C010630**:102 (2001).

[62] N. Arkani-Hamed, S. Dimopoulos, and G. Dvali, "The hierarchy problem and new dimensions at a millimeter," *Phys. Lett.* **B429**:263 (1998).

[63] S. Dimopoulos, N. Arkani-Hamed and G. Dvali, "New dimensions at a millimeter to a fermi and superstrings at a TeV," *Phys. Lett.* **B436**:257 (1998).

[64] A. Anastassov, "Non-isolated pi0/gamma reconstruction," *CDF Note* 6688.

[65] M. Coca and E. Halkiadakis, "Central electron identification efficiencies for winter 2003 conferences," *CDF Note* 6262.

[66] F. Ratnikov, "Tau reconstruction for CDF Eun II," *CDF Note* 6252.

[67] P. Murat, "$W \to \tau\nu$ signal in Run II data and preliminary measurement of $\sigma \times BR(W \to \tau\nu)/\sigma \times BR(W \to e\nu)$," *CDF Note* 6010.

[68] Y. Miyazaki *et al.*, "Improved extraction of $Z^0 \to \tau\tau$ events from low p_T lepton datasets in Run Ib," *CDF Note* 5251.

[69] A. Anastassov *et al.*, "Tau reconstruction efficiency and qcd fake rate for Run 2," *CDF Note* 6308.

[70] K. McFarland, S. Demers, J. Insler, and T. Vaiciulis, "Backgrounds to $Z \to \tau_e\tau_{had}$," *CDF Note* 6400.

[71] S. Baroiant *et al.*, "Measurement of electron trigger efficiencies for Level 1 and Level 2 8-Gev triggers," *CDF Note* 6257.

[72] S. Baroiant *et al.*, "Measurement of the 8 Gev inclusive electron Level 3 trigger efficiency using conversions," *CDF Note* 6324.

[73] G. Manca and Y. K. Kim, "Z^0 to electrons cross section measurement with Run II data," *CDF Note* 6281.

[74] K. Bloom *et al.*, "Updated measurements of $\sigma(p\bar{p} \to W \to \mu\nu), \sigma(p\bar{p} \to Z \to \mu\mu)$, and R using CDF Run II data," *CDF Note* 6302.

[75] S. R. Choudhury and N. Gaur, "Dileptonic decay of B_s meson in SUSY models with large $\tan\beta$," *Phy. Lett.* **B451**:86 (1999).

[76] H. Dreiner, A. Dedes, and U. Nierste, "Correlation of $B_s \to \mu^+\mu^-$ and $(g-2)_\mu$ in Minimal Supergravity," *Phys. Lett.* **87**:251804 (2001).

[77] R. Arnowitt, *et al.*, "Detection of $B_s \to \mu^+\mu^-$ at the Tevatron Run II and constraints on the SUSY parameter space," *Phys. Lett.* **B538**:121 (2002).

[78] H. Baer *et al.*, *J. High Energy Phy. 07* (2002).

[79] R. Dermisek *et al.*, *Phys. Lett.*, **B**538:121, 2002.

[80] CDF Collaboration, F. Abe *et al.*, "Search for the decays $B_d^0 \to \mu^+\mu^-$ and $B_s^0 \to \mu^+\mu^-$ in $p\bar{p}$ collisions at $\sqrt{s} = 1.8$ TeV," *Phys. Rev.* **D57**:R3811 (1998).

[81] G. Bunchalla and A.J.Buras, *Nucl. Phys.* **B398**:285 (1993); **B400**:225 (1993); **548**:309 (1999); M. Misiak and J. Urban, *Phy. Lett.* **B451**:161 (1999).

[82] Belle Collaboration, M. C. Chang *et al.*, "Search for $B^0 \to \ell^+\ell^-$ at the Belle detector," *Phys. Rev.* **D68**:111101(R) (2003).

[83] Muon $g-2$ Collaboration, G. W. Bennett *et al.*, "Measurement of the Negative Muon Anomalous Magnetic Moment to 0.7 ppm," *Phys. Rev. Lett.* **92**:161802 (2004).

[84] D. N. Spergel *et al.*, *Astrophys. J. Suppl. Ser.* **148**:175 (2003).

[85] D. Acosta *et al.*, *Nucl. Instrum. Methods Phy. Res., Sect. A* **494**:57 (2002); S. Klimenko, J. Konigsberg, and T. M. Liss, *Fermilab Report* FERMILAB-FN-0741 (2003).

[86] E. J. Thomson *et al.*, *IEEE Trans. Nucl. Sci.* **49**:1063 (2002).

[87] T. Sjostrand *et al.*, *Comput. Phys. Commun.* **135**:238 (2001).

[88] K. Lannon, *Ph.D.thesis, University of Illinois at Urbana Champaign* (2003).

[89] Particle Data Group, K. Hagiwara *et al.*, *Phys. Rev.* **D66**:010001 (2002).

[90] CDF Collaboration, D. Acosta *et al.*, *Phys. Rev.* **D65**:052005 (2002). This corresponds to a measurement at $\sqrt{s} = 1.8$ TeV. No correlation is made to account for the increased $\sqrt{s}$ since it is small compared to the uncertanity on the measured σ_{B^+}.

[91] M .J. Kim *et al.*, "Combined limits from searches for R-parity violating scalar top quark decays in the $e\tau jj \& \mu\tau jj$," *CDF Note* 5601.

[92] V. Martin *et al.* "High p_T, recommended cuts and efficiencies for release 5.3.1," *CDF Note* 7031.

[93] S. Baroiant *et al.*, "Measurement of $Z \to \tau\tau$ cross-section -electron channel-," *CDF Note* 6552.

[94] C. Hill *et al.*, "Electron identification in offline release 5.3," *CDF Note* 7309.

[95] C. Hill *et al.*, "Generic Jet Energy Correction for Run II data used for the Winter Conference," *CDF Note* 280.

[96] S. Baroiant *et al.*, "Measurement of the Level 1 trigger efficiency for the muon plus track trigger," *CDF Note* 6358.

[97] S. Baroiant *et al.*, "Level 1 and Level 3 trigger efficiency for the cmx muon plus track trigger," *CDF Note* 6760.

[98] S. Baroiant *et al.*, "Measurement of the Level 3 trigger efficiency for the muon plus track trigger (the CMUP case)," *CDF Note* 6621.

[99] S. Baroiant *et al.*, "XFT efficiency for the isolated track leg of the electron + track trigger," *CDF Note* 6510.

[100] S. Baroiant *et al.*, "Lepton + track triggers: Measurement of the Level 3 trigger efficiency for taus," *CDF Note* 6553.

[101] J. Conway, "Calculation of cross section upper limits combining channels incorporating correlated and uncorrelated systematic uncertainies," *CDF Note* 6428.

[102] E. Halkiadakis *et al.*, "PDF uncertanities for W and Z cross section measurement," *CDF Note* 6890.

[103] O. Gonzalez and C. Rott, "Uncertainties due to the PDFs for the gluino-sbottom search," *CDF Note* 7051.

[104] S. Baroiant *et al.*, "γ + jet and W ; jet backgrounds to $Z/h \to \tau\tau$," *CDF Note* 6734.

Publication List

Published Papers

1. CDF Collaboration, D. Acosta *et al.*, "Search for $B_s^0 \to \mu^+\mu^-$ and $B_d^0 \to \mu^+\mu^-$ Decays in $p\bar{p}$ Collisions at $\sqrt{s} = 1.96$ TeV," *Phys. Rev. Lett.* **93**, 2004, pp.032001.
2. S. Baroiant, M. Chertok, M. Goncharov, T. Kamon, V. Khotilovich, R. Lander, T. Ogawa, C. Pagliarone, F. Ratnikov, A. Safonov, A. Savoy-Navarro, J. R. Smith, E. Vataga, CDF Collaboration, "The CDF II Tau Physics Program - Triggers, tau ID and Preliminary Results," 4^{th} International Workshop on Very High Multiplicity Physics, Alushta Crimea, Ukraine, May31-June4 2003.
3. A. Anastassov *et al.*, "Selection of Tau Leptons with the CDF Run 2 Trigger System," 9^{th} Pisa Meeting on Advanced Detectors - La Biodola, Isola d'Elba, Italy, May25-31 2003.

Oral Reports

1. T. Ogawa, "Search for R-parity Violating Stop in CDF Run II," The Physical Society of Japan, Fukuoka, March 2004.
2. T. Ogawa, "Lepton plus Track (τ) Trigger in CDF Run II," The Physical Society of Japan, Miyazaki, September 2003.
3. T. Ogawa, "$Z \to \tau\tau$ and R-parity Violating SUSY Search with taus at CDF-II," American Physical Society, Philadelphia, April 2003.